

STRUCTURAL INSIGHTS INTO THE ACTIVE SITE OF ALPHA-CARBONIC
ANHYDRASES

By

SUZANNE ZOË FISHER

A DISSERTATION PRESENTED TO THE GRADUATE SCHOOL
OF THE UNIVERSITY OF FLORIDA IN PARTIAL FULFILLMENT
OF THE REQUIREMENTS FOR THE DEGREE OF
DOCTOR OF PHILOSOPHY

UNIVERSITY OF FLORIDA

2006

Copyright 2006

By

Suzanne Zoë Fisher

This document is dedicated to my parents, Alet and Peter Fisher.

ACKNOWLEDGMENTS

I would like to thank my advisor and mentor, Dr. Robert McKenna. Throughout my stay in his lab, he was an inspiration and a constant source of enthusiasm and encouragement. He was always available for questions and very patient, to say the least. Without him, none of this work would have been possible and I thank him deeply and sincerely for his outstanding guidance over the years. Another key person to thank is Dr. David Silverman. I have worked closely with him and his lab and appreciate the excellent advice and insightful discussions that we have had. I would also like to thank my other committee members, Dr. James Flanagan and Dr. Maurice Swanson. Together, my committee has shown nothing but support and respect for me and my work and their supervision has kept me on track and focused on my goals.

I would like to thank some of the other labmembers and friends. Mavis Agbandje-McKenna, Lakshmanan Govindasamy, Deepa Bhatt, and Huyn-Joo Nam have all given me a lot of assistance, general advice, and technical expertise. The graduate students John Domsic, Brittney Whitaker, and Nicolette Case have made a lot of tough times manageable and provided many a good laugh. I would also like to thank the undergraduates Edward Miller, Mike DiMattia, and Caroli Genis for great conversations and being good company. The McKenna lab really is a special and unique place and I will miss it a great deal.

I would also like to thank Kathy Conture, Susan Gardner, and Wayne McCormack who are part of the administrative staff for the IDP and have helped me with all things

practical over the years. Also, Pat Jones and Terry Rickey from the Biochemistry and Molecular Biology Department have been helpful with everyday things, from registering for class to purchasing chemicals for the lab.

Lastly, I would like to thank my family. Despite living far away in South Africa, they have always supported and encouraged me to stay in the United States and continue my studies. A special thank you also goes to my American family, the Hunts. They have been generous and kind by welcoming me into their home and making me a part of their family.

TABLE OF CONTENTS

	<u>page</u>
ACKNOWLEDGMENTS	iv
LIST OF TABLES	ix
LIST OF FIGURES	x
ABBREVIATIONS	xii
ABSTRACT	xiv
CHAPTER	
1 INTRODUCTION	1
The Discovery of Carbonic Anhydrase	1
A Fine Example of Convergent Evolution	2
Human Carbonic Anhydrases (HCAs)	5
Structure of HCA II	9
Activity and Catalytic Mechanism of CAs	10
Substrate Binding in the CA Active Site	11
Measuring CA Activity	13
HCA and Human Disease	14
CA Inhibitors	16
2 STRUCTURAL AND KINETIC ANALYSIS OF PROTON SHUTTLING IN HUMAN CARBONIC ANHYDRASE II	28
Introduction	28
Materials and Methods	32
Enzymes	32
Crystallography	33
Activity Analysis by ¹⁸ O Exchange	35
Results and Discussion	36
Crystallography	36
Effect of pH on the Wild Type HCA II Active Site	37
Effect of pH on the Mutant HCA II Active Site	39
Catalysis	41
Conclusion	42

3	STRUCTURAL AND KINETIC EFFECTS OF HYDROPHOBIC MUTATIONS IN THE ACTIVE SITE OF HUMAN CARBONIC ANHYDRASE II	51
	Introduction.....	51
	Materials and Methods	52
	Enzymes	52
	Crystallography	53
	Kinetics and Activity Analysis.....	54
	Results and Discussion	55
	Structural Effects of Hydrophobic Mutations	55
	Kinetic Effects of Hydrophobic Mutations	58
	Solvent Structure and Implications for Proton Transfer.....	60
	Conclusion.....	63
4	WORKING TOWARDS A NEUTRON STRUCTURE OF PERDEUTERATED HUMAN CARBONIC ANHYDRASE II	75
	Introduction.....	75
	Materials and Methods	82
	Production and Crystallization of Perdeuterated HCA II.....	82
	Crystallography	83
	Activity Analysis by ¹⁸ O Exchange Methods.....	84
	Results and Discussion	84
	Structural Effects of Perdeuteration	85
	Kinetic Effects of Perdeuteration	87
	Conclusion.....	88
5	NOVEL INHIBITORS AND THEIR BINDING MODES TO HCA II	99
	Introduction.....	99
	Materials and Methods	101
	Expression, Purification, and Crystallization.....	101
	Synchrotron X-ray Data Collection.....	101
	Structure Determination and Model Refinement	102
	Results and Discussion	103
	Conclusion.....	105
6	EXPRESSION, PURIFICATION, KINETIC, AND STRUCTURAL CHARACTERIZATION OF AN ALPHA-CLASS CA FROM AEDES AEGYPTI (AACA1).....	114
	Introduction.....	114
	Materials and Methods	116
	Expression and Purification.....	116
	Activity Analysis by ¹⁸ O Exchange.....	117
	Determination of Inhibition Constants	118
	Model Building.....	118

Results and Discussion	119
Conclusion	122
7 CONCLUSIONS AND FUTURE DIRECTIONS	130
Summary and Conclusions	130
Future Directions	134
LIST OF REFERENCES	136
BIOGRAPHICAL SKETCH	149

LIST OF TABLES

<u>Table</u>	<u>page</u>
1-1 Catalytic constants and subcellular locations of active α -CA isozymes	19
2-1 Data set and model statistics for wild type HCA II from pH 5.1 to 10.0.....	44
2-2 Data set and model statistics for H64A/N62H and H64A/N67H HCA II at pH 6.0 and 7.8.	45
2-3 pH-Independent rate constants for proton transfer and pK_a for proton donor and acceptors in wild type and mutant HCA II.....	46
3-1 Data set and final model statistics for N62L HCA II and N67L HCA II.....	65
3-2 Data set and final model statistics for Y7F HCA II.	66
3-3 Maximal values of rate constants for hydration of CO_2 , proton transfer, and pK_a of the zinc-bound water.....	67
4-1 Scattering amplitudes and cross sections of atoms by X-rays and neutrons.	90
4-2 Data collection and model refinement statistics.....	91
4-3 Distances between solvent molecules and active site residues for hydrogenated and perdeuterated HCA II.	92
5-1 Data collection, refinement and final model statistics.	107
6-1 Maximal values of k_{cat}/K_m for the hydration of CO_2 and k_B for the proton transfer dependent release of $H_2^{18}O$ from isoforms of carbonic anhydrase.....	124

LIST OF FIGURES

<u>Figure</u>	<u>page</u>
1-1 Ribbon diagram of CA from three classes	20
1-2 Multiple sequence alignment of fourteen HCA domains	21
1-3 Conservation of HCAs.	22
1-4 Active sites of HCA I, II, and III.....	23
1-5 Molecular and electrostatic surface potentials of HCAs.	24
1-6 Ribbon diagram of HCA II with secondary structure elements	25
1-7 Active site of wild type HCA II	26
1-8 HCA II in complex with inhibitors.	27
2-1 Crystal structures of wild type HCA II active site	47
2-2 Crystal structures of mutant HCA II active site	48
2-3 The pH profiles for k_{cat}/K_M catalyzed by wild type and mutant HCA II.	49
2-4 The pH profiles for $RH_2O/[E]$ catalyzed by wild type and mutant HCA II.....	50
3-1 Active site of wild type human carbonic anhydrase II.....	68
3-2 Active site of N62L and N67L at pH 8.2 and pH 6.0	69
3-3 Active site of Y7F HCA II at various pH.....	70
3-4 The pH profiles for k_{cat}/K_M catalyzed by wild type and mutant HCA II	71
3-5 The pH profiles for $RH_2O/[E]$ catalyzed by wild type and mutant HCA II.....	72
3-6 Activation of $RH_2O/[E]$ catalyzed by wild type and mutant HCA II by the addition of 4-methylimidazole	73
3-7 Active sites of wild type and Y7F HCA II.....	74

4-1	The LANSCE position-sensitive ^3He -filled detector.	93
4-2	Optical photograph of perdeuterated wild type HCA II.....	94
4-3	Backbone superposition of hydrogenated and perdeuterated wild type HCA II.....	95
4-4	Active site comparison of hydrogenated and perdeuterated wild type HCA II	96
4-5	The pH profiles for k_{cat}/K_M catalyzed by hydrogenated and perdeuterated HCA II.	97
4-6	The pH profiles for $R_{\text{H}_2\text{O}}/[E]$ catalyzed by hydrogenated and perdeuterated HCA II.	98
5-1	Classical carbonic anhydrase inhibitors bound to HCA II.....	108
5-2	Chemical structure of novel inhibitors	109
5-3	Active site structures of HCA II in complex with two novel inhibitors	110
5-4	HCA II active site with inhibitors superimposed	111
5-5	Interactions of BB3 and TDM with HCA II	112
5-6	HCA II with BB3 and TDM superimposed	113
6-1	Sequence alignment of AaCA1 with HCA I and II.....	125
6-2	The 12% Coomassie stained polyacrylamide gel of AaCA1 expression and purification	126
6-3	The pH profile of rate constants for catalysis by AaCA1	127
6-4	Molecular model of AaCA1.....	128
6-5	Active sites and surface charge distribution of AaCA1, HCA I, and HCA II	129

ABBREVIATIONS

Å	Angstrom
<i>A. aegypti</i>	<i>Aedes aegypti</i>
CA	carbonic anhydrase
CAPS	N-cyclohexyl-3-aminopropanesulfonic acid
CHES	N-cyclohexyl-2-aminoethanesulfonic acid
CO ₂	carbon dioxide
cm	centimeter
<i>E. coli</i>	<i>Escherichia coli</i>
g	gravitational force
gm	gram
H ⁺	proton/ hydrogen ion
HCA	human carbonic anhydrase
HCl	hydrochloric acid
HCO ₃ ⁻	bicarbonate ion
HEPES	N-(2-hydroxyethyl)-piperazine-N'-2-ethanesulfonic acid
IPTG	isopropyl-β-D-thiogalactopyranoside
k _{cat}	turnover number
k _{cat} /K _M	specificity constant
kD	kilo Daltons
K _i	inhibition constant

K_M	Michaelis-Menten constant
kV	kilovolt
LB	luria broth
M	molar
MES	2-(4-morpholino)-ethane sulfonic acid
MOPS	3-(N-morpholino)-propanesulfonic acid
μg	microgram
μl	microliter
μM	micromolar
mA	milliampere
mg	milligram
ml	milliliter
mm	millimeter
mM	millimolar
nm	nanometer
nM	nanomolar
pAMBS	para-aminomethylbenzenesulfonamide
pH	negative log of the hydrogen ion concentration
rmsd	root mean square deviation
TAPS	N-Tris(hydroxymethyl)methyl-3-aminopropanesulfonic acid
Tris	tris(hydroxymethyl)aminomethane
Zn	zinc

Abstract of Dissertation Presented to the Graduate School
of the University of Florida in Partial Fulfillment of the
Requirements for the Degree of Doctor of Philosophy

STRUCTURAL INSIGHTS INTO THE ACTIVE SITE OF ALPHA-CARBONIC
ANHYDRASES

By

Suzanne Zoë Fisher

December 2006

Chair: Robert McKenna

Major Department: Medical Sciences--Biochemistry and Molecular Biology

Carbonic anhydrases (CA) are ubiquitously expressed metalloenzymes that are found in all organisms, ranging from bacteria to humans. Human CA II (HCA II) is the most well-studied and utilizes a zinc-hydroxide mechanism to catalyze the reversible hydration of carbon dioxide to produce bicarbonate and a proton. Catalysis involves an intramolecular proton transfer event that delivers an excess proton from the zinc-bound water to an internal proton acceptor, His64. His64 then shuttles this proton to the bulk solvent, thus regenerating the active site for the next round of catalysis.

An extensive analysis of the structural and kinetic stability of wild type and several mutants of HCA II was conducted over a broad pH range. The results show that the enzyme, and the water network in the active site, is extremely stable. It is also the first observation of sulfate ion binding in the active site of wild type HCA II. Attempts to disrupt not only the proton shuttle His64, but other residues involved in stabilizing the water network were also successful as reflected in changes of the measured proton transfer rates. Overall, the results give insights into the structural requirements for efficient proton transfer as catalyzed by CA. To directly observe the active site waters

and protonation state of His64, perdeuterated wild type HCA II was produced, crystallized and the X-ray structure determined. This work lays the foundation for future proposed neutron diffraction experiments.

Classical, clinically used CA inhibitors (CAI) are not very water-soluble and this feature has implications for bioavailability of these drugs. The X-ray structures of two novel, water-soluble CAIs bound to HCA II were determined. They reveal that incorporation of spacer groups and fluorines can change the binding modes of CAIs. This work has implications for the clinical use and bioavailability of systemically applied CAIs and for targeting different isozymes of HCA.

A CA from mosquito larvae (AaCA1) was also expressed, purified, and structurally and kinetically characterized. AaCA1 is a high activity CA that shows inhibition with all the classical sulfonamide-based CAIs. This enzyme represents an interesting new drug target for the control of mosquito populations and further understanding of CA function in other organisms.

CHAPTER 1 INTRODUCTION

The Discovery of Carbonic Anhydrase

Prior to the discovery of carbonic anhydrase (CA) there were two main theories as to the physiological mechanism of carbon dioxide transport in blood. The first (bicarbonate theory) stated that carbon dioxide was transported as bicarbonate and upon reaching the lung, was converted by blood proteins to carbon dioxide and expelled. The second (direct combination theory) declared that carbon dioxide is carried directly by blood proteins, primarily hemoglobin, and can reversibly dissociate from them, upon reaching the lung (Forster, 2000). From 1917 to 1921 the bicarbonate theory gained a lot of support through the efforts of many physiologists. However, early experiments by Thiel in 1913 studied the uncatalyzed rate of carbon dioxide hydration and found it slow at near 0.02 s^{-1} . This low rate was obviously insufficient as red blood cells (RBCs) only have about 1 second in the lung to exchange carbon dioxide. In 1926 Henriques calculated the hydration rate under physiological conditions using velocity constants obtained by others and concluded that there must be a catalyst in blood that speeds up the hydration reaction. He also predicted that there must be another mechanism that does not purely rely on the bicarbonate theory (Henriques, 1928). Later experiments involved determination of the rate of carbon dioxide production from hemoglobin solutions. These showed that there was a dramatic increase in the rate compared to just buffer alone. These observations gave support to the direct combination theory, which led to the suggestion that carbamate binds to hemoglobin giving rise to a hypothetical complex called

carbhemoglobin (Henriques, 1928). As it later turned out, the hemoglobin purification technique was not perfect and actually contained a contaminant, carbonic anhydrase, that was mediating the observed catalysis. It was not until 1932 that Meldrum and Roughton isolated a non-hemoglobin protein from ox blood and showed that it was catalyzing the carbon dioxide hydration reaction. They named this protein carbonic anhydrase (Meldrum and Roughton, 1932). Then in 1933 the same authors published a paper that described the details of CA preparation and its catalytic properties. Their rather crude initial experiments tested an impressive array of CA properties including temperature and pH stability. Their results indicated that pure preparations of CA that were heated to 65 °C for 30 minutes still retained 40% activity and the protein was stable and active from pH 4.0 to 12.0. In the same paper they also showed that CA was potently inhibited by cyanide and azide (Meldrum and Roughton, 1933). Since the early discoveries and observations in the 1930's the CA field has grown enormously and a lot is known about the various isoforms, physiological functions, catalytic activity, and crystal structures.

A Fine Example of Convergent Evolution

From humans to plants, the ubiquitous zinc metalloenzyme CA catalyzes the reversible hydration of carbon dioxide (CO_2) to form bicarbonate (HCO_3^-) and a proton (H^+). There are five evolutionary distinct classes of CAs: α , β , γ , δ , and ϵ . The α -class was discovered first and is found primarily in mammals but has also been identified in such diverse organisms as the mosquito and plant green algae, *Chlamydomonas reinhardtii*. The β -class is found in plants but there are also examples found in *Escherichia coli* (*E. coli*) and *Synechococcus* (Hewett-Emmett and Tashian, 1996). The γ -class is found mainly in archaeobacteria and was initially discovered in the archeon

Methanosarcina thermophila (Alber and Ferry, 1996). *Arabidopsis thaliana* and *Synechococcus* seem to be the exceptions by having sequences that have similarity to all three classes (Hewett-Emmett and Tashian, 1996). The recently discovered δ - and ϵ -classes have not been extensively studied and are found in diatoms and cyanobacteria, respectively (Tripp *et al.*, 2001; So *et al.*, 2004). Most living organisms have genes that encode for CAs, except for *Mycoplasma genitalium* that appears to lack any CA-encoding gene (Fraser *et al.*, 1995).

There are numerous crystal structures of α -, β -, and γ -class CAs (Figure 1-1) that are available in the Protein Data Bank (www.pdb.org). Currently, there are well over 200 CA structures; most of these are α -class CAs and are, more specifically, represented by 5 human CA (HCA) isozyme structures, HCA I, II, as well as extracellular domains of HCA IV, XII, and XIV (Liljas *et al.*, 1972; Kannan *et al.*, 1975; Stams *et al.*, 1996; Whittington *et al.*, 2001; Whittington *et al.*, 2004). Crystal structures of the α -class (Figure 1-1(a)) include various mutants of different isoforms as well as complexes of the protein with inhibitors and/or activators. The first CA crystal structure of human isozyme II was determined in 1972 (Liljas *et al.*, 1972). More recently, the first β - and γ -CA crystal structures have been reported (Mitsuhashi *et al.*, 2000; Kisker *et al.*, 1996).

Visual inspection of the crystal structures of the three classes (α -, β -, and γ -classes) reveals a dramatic picture of the variation in topology of these zinc-containing enzymes (Figure 1-1 (a)-(c)) and it is no surprise that the different class members are found in phylogenetically diverse organisms (Strop *et al.*, 2001). The α -CAs act mainly as monomers except in the case of HCA XII that was shown to be a dimer (Whittington *et al.*, 2001). The structures of β - and γ -class CA reveal that they oligomerize to form

pseudo-dimers and trimers, respectively (Mitsuhashi *et al.*, 2000; Iverson *et al.*, 2000). Despite the obvious overall structural differences between these classes, closer inspection of the active sites reveal a remarkably similar architecture of the catalytic zinc center. The carbonic anhydrases are an excellent example of convergent evolution where distinctly varied life forms have found structurally alternative ways to construct an enzyme that has the same catalytic mechanism (Figure 1-1; Lindskog, 1997).

The many physiological functions of CA have been most extensively characterized in plants and mammals. In mammals CA is involved in many physiological processes such as acid/base homeostasis, renal acidification, bone resorption, cellular respiration, gluconeogenesis, formation of gastric acid, cerebrospinal fluid and aqueous humour production, tumor metastasis, and the interconversion of $\text{CO}_2/\text{HCO}_3^-$ in red blood cells (RBCs) during respiration (Henry, 1996; Breton, 2001; Chegwiddden and Carter, 2000).

Due to all these functions that are vital to all life processes CAs are found in virtually all tissue types. In plants CA is found in both the cytosol and the chloroplast where it is primarily involved with providing carbon for the fixation of inorganic carbon into sugar. Carbonic anhydrase provides either HCO_3^- or CO_2 as a source of inorganic carbon for either PEP carboxylase or RuBisCO (ribulose-1,5-bisphosphate carboxylase/oxygenase), respectively (Burnell, 2000). The functions of CA in bacteria are less well understood except for two well-documented cases. The first is the role of CA in *E. coli* where, as a part of the *cyn* operon, it prevents depletion of CO_2 during cyanate breakdown (Guilloton *et al.*, 1992). The second is in cyanobacteria where CA is part of the carboxysome shell. Carboxysomes are polyhedral microcompartments that consist of several shell proteins that “package” RuBisCO for carbon fixation. RuBisCO is

a notoriously slow enzyme and it is thought that CA, present in the carboxysomal shell, can convert HCO_3^- into CO_2 and deliver this substrate directly to RuBisCO in high local concentrations (So *et al.*, 2004).

Human Carbonic Anhydrases (HCAs)

In the human α -class there are fourteen identified expressed CA isoforms (HCA I – XIV) and there are examples of cytosolic (HCA I, II, III, and VII), transmembrane/membrane anchored (HCA IV, IX, XII and XIV), secretory (HCA VI and XI) and mitochondrial isoforms (HCA VA and VB) (Chegwidden and Carter, 2000; Duda and McKenna, 2004). The percentage sequence identity varies from 26 to 61% among all fourteen isoforms and they differ in catalytic efficiency and subcellular location (Table 1-1, Figure 1-2). Table 1-1 summarizes some of the properties for representative active α -CAs. Some of the isozymes, such as HCA II and IV, are high activity forms that work near the diffusion limit. Most of the ones listed in Table 1-1 fall in the medium activity level range while HCA III represents the isozyme with the lowest catalytic rate constants.

Figure 1-2 is a multiple sequence alignment of the CA domains of all fourteen HCAs, and the conserved and similar residues are marked as described in the figure legend. Figure 1-3 indicates the location, on the backbone of a CA domain, of all the conserved residues found in all fourteen HCAs. It is striking that these residues are not located directly in the active site but seem to cluster around it. This distribution implies that the variation seen in the active sites is necessary for the wide range of catalytic rates for different isozymes (Table 1-1). The conserved residues overall appear to have a role in maintaining the distinctive CA fold. Very few of these residues are found on the

surface and the resulting surface heterogeneity lends support for the different cellular locations and functions of the various HCAs (Table 1-1; Figure 1-3)

HCA I is found predominantly in RBCs while HCA II, also abundant in RBCs, is also found in cells of all tissue types (Tashian, 1992). HCA I and HCA II's presence in the RBCs are very important for converting HCO_3^- into CO_2 during respiration. Figure 1-4 shows the active sites of cytoplasmic HCA I, HCA II, and HCA III. The active sites of these three isozymes are highly conserved and the differences indicated in Figure 1-4 could account for the observed differences in their respective activities (Table 1-1). HCA III is a major part of the soluble protein in adipose and muscle tissue, but its function in these tissues remains elusive. Despite its abundance, recent studies with mouse knock-out models of HCA III showed no phenotype (Sly and Hu, 1995; Kim *et al.*, 2004).

HCA IV is the only glycosylphosphatidylinositol(GPI)-linked isoform and, in contrast to CA IV in other species, not glycosylated. The CA domain of HCA IV is located on the extracellular face of cells in many tissue types that include kidney, lung, and the eye (Sly and Hu, 1995; Chegwiddden and Carter, 2000).

Of the mitochondrial CAs there are two HCA V variants, CA VA and CA VB. HCA VA is expressed only in the liver while HCA VB expression is everywhere except the liver. HCA V is mainly involved with providing HCO_3^- to metabolic enzymes in the gluconeogenesis and ureagenesis pathways (Dodgson, 1991).

HCA VI is heavily glycosylated and the only secreted isoform in humans. It is found predominantly in saliva where it is involved with pH control of the mouth (Murakami and Sly, 1987). HCA VII is another cytoplasmic, soluble isoform that is expressed mainly in the brain, salivary gland, and lung. It is the most highly conserved

(compared to the consensus CA domain sequence) of all the active CA isoforms, but its function remains unknown (Chegwidden and Carter, 2000).

HCA VIII, X, and XI have no catalytic activity but contain a CA domain. These inactive isoforms are subsequently known as the CA-Related Proteins, or CA-RPs (Khalifah, 1971; Jewell *et al.*, 1991; Kato, 1990; Skaggs *et al.*, 1993). The lack of catalytic activity in the HCA-RPs is due to deleterious mutations of the zinc ligand histidines (Figure 1-2). CA-RP VIII is highly conserved across species and shares about 98% sequence identity between humans and mice (Bergenheim *et al.*, 1998). HCA-RP is widely expressed throughout the brain and its expression is developmentally controlled (Taniuchi *et al.*, 2002).

HCA IX was first identified in HeLa cells and is a glycosylated extracellular enzyme with a membrane-spanning region (Pastoreková *et al.*, 1992). It is normally expressed only in the gastrointestinal epithelial lining but is usually absent in normal tissues. HCA IX displays constitutive expression in tumors such as clear cell renal carcinoma and has potential as a biomarker for certain tumors (Murakami *et al.*, 1999; Ortova Gut, 2002). HCA XII is another transmembrane glycoprotein with its CA domain located on the extracellular side of cells. It is expressed mainly in colon, kidney, and prostate, but it was discovered due to overexpression of its mRNA in renal and lung cancer cells (Türeci *et al.*, 1998; Ulmasov *et al.*, 2000). The crystal structure revealed that this membrane protein exists as a dimer (Whittington *et al.*, 2001).

HCA XIII is the most recent addition to the HCA family and is predicted to be a cytosolic isoform, similar to HCA I and II. Not much is known about its function but it has been identified in thymus, spleen, and colon (Lehtonen *et al.*, 2004).

HCA XIV is the last of the human isoforms and shows 45% sequence identity to HCA XII (Fujikawa-Adachi *et al.*, 1999). It is also a single-membrane spanning glycoprotein with an extracellular catalytic domain but, unlike HCA XII, the crystal structure of murine CA XIV shows it to be monomeric (Whittington *et al.*, 2004). In humans, it is widely expressed but is found mainly in heart and kidney (Chegwidden and Carter, 2000).

Figure 1-5 shows the molecular surface and electrostatic charge distributions of several representative HCAs. HCA II and III are the most and least efficient of the catalytically active cytosolic HCAs, respectively. HCA II appears to be more negatively charged around the active site region compared to HCA III. HCA VI (Figure 1-5 (c)) is the only secreted isoform and is more hydrophobic around the active site compared to the other soluble forms shown in Figure 1-5 (a) and (b).

HCA-RP VIII is one of the acatalytic isoforms and its subcellular location is unknown. Compared to the other isoforms shown in Figure 1-5, HCA-RP VIII has a much higher overall negative charge distribution.

HCA IX is a membrane protein and the surface shown is for the catalytic CA domain (Figure 1-5 (e)). It has an asymmetric distribution of negative charge and hydrophobicity at the region adjacent to the active site. HCA XII is dimeric membrane protein (Figure 1-5 (f)) with the two active sites located on the same side of the dimer. These surface features of the HCAs reflect the variation in amino acid sequence among them. As is shown in Figure 1-3, the most conservation of sequence is not in the active site or the surface, but in the regions that form the scaffold of the metal binding center.

Structure of HCA II

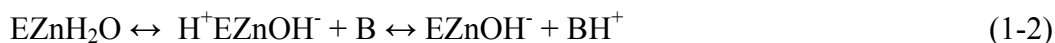
The first crystal structure of HCA II was determined over thirty years ago by Liljas and colleagues (Liljas *et al.*, 1972). The overall fold of HCA II can be described as a single-domain, mixed α/β , globular protein that is almost spherical with approximate dimensions of 5 x 4 x 4 nm³ (Figure 1-6; Lindskog, 1997). These enzymes are overall small and compact proteins with the possible exception of the N-terminal region (residues 1 to 24) that is more loosely connected to the rest of the molecule. N-terminal residues 1-4 are usually disordered in the crystal structures. A cluster of aromatic residues at the N-terminus of the enzyme consisting of Trp5, Tyr7, Trp16, and Phe20 has been suggested to assist in the anchoring of this region to the rest of the enzyme (Lindskog, 1997). It has been shown that the removal of the N-terminal region does not result in a major loss of protein stability or enzyme activity. Another cluster of aromatic residues located under the β -sheet consists of Phe66, Phe70, Phe93, Phe95, Trp97, Phe176, Phe179, and Phe226 (Lindskog, 1997). The active site folds first and independently of the N-terminal region (Aronsson *et al.*, 1995). The central feature of the HCA II structure can be described as a 10-stranded (β A- β J) twisted β -sheet, which is decorated on the surface by seven α -helices (Figure 1-6; α A- α G). The strands of the β -sheet are mainly antiparallel, with the exception of two pairs of parallel strands (Figure 1-6; β F and β G, β I and β J). There is a conserved loop region extending towards the active site that contains the proton shuttling residue, His64. The active site consists of a conical cleft that is ~ 15 Å deep with the catalytic Zn²⁺ placed at the bottom of the cleft (Figure 1-6).

The Zn²⁺ is tetrahedrally coordinated by four direct ligands: the imidazole groups of three conserved His residues (His94, His96, and His119) and a H₂O/ OH⁻ molecule

(Figure 1-7). The direct metal ligand histidines, in turn, are held in position by hydrogen bonding interactions with other residues, the indirect or second shell metal ligands. The side chains of Gln92 and Glu117 interact with His94 and His119, respectively, while the carbonyl oxygen of Asn244 coordinates His96. Thr199 makes a hydrogen bond with the solvent metal ligand and is optimally oriented for this by interacting with Glu106 (Christianson and Fierke, 1996).

Activity and Catalytic Mechanism of CAs

HCA II kinetics and catalytic mechanism have been studied extensively; however, it is thought that all α -CAs perform the same general activity, which is known as the zinc-hydroxide mechanism. The interconversion between CO_2 and HCO_3^- is a two-step reaction that can be described as a ping-pong mechanism (eq 1-1 and 1-2; Silverman and Lindskog, 1988; Lindskog, 1997; Christianson and Fierke, 1996).



The first step (eq 1-1) in the hydration direction is the binding of CO_2 in a hydrophobic region adjacent to the zinc atom. Substrate binding is then followed by a nucleophilic attack on the carbon by the zinc-bound hydroxide leading to the formation of HCO_3^- . Water can freely diffuse into the active site and displace HCO_3^- leaving a water molecule bound at the zinc atom. The second part of the reaction (eq 1-2) occurs at 10^6 s^{-1} and is the rate-limiting step of the overall reaction and involves the removal of an excess proton from the zinc-bound water to regenerate the hydroxide needed for catalysis (Khalifah, 1971; Steiner *et al.*, 1975; Silverman and Lindskog, 1988). The transfer of a proton out of the active site involves an intramolecular and intermolecular proton transfer

event. The intramolecular proton transport occurs between the Zn-bound solvent and the side chain of His64 through an intervening chain of hydrogen-bonded water molecules, W1, W2, W3a, and W3b (Figure 1-6; Lindskog and Silverman, 2000; Fisher *et al.*, 2005). Mutation of His64 to an alanine results in a 10-50 fold reduction in the proton transfer rate (Tu *et al.*, 1989). From His64 the intermolecular transfer event delivers the proton to bulk solvent/buffer. In eq 1-2, B signifies either an acceptor on the protein (His64) or an exogenous acceptor that becomes protonated, BH^+ (Silverman and Lindskog, 1988).

For CO_2 hydration in HCA II, both the k_{cat} and k_{cat}/K_m have pH profiles that appear as simple titration curves with a $pK_a \sim 7$ and with maximal activity at high pH (Silverman and Lindskog, 1988). HCA II is the most efficient isozyme ($k_{cat} = 1.4 \times 10^6 \text{ s}^{-1}$ at 25° C) of this class while HCA III is the slowest ($k_{cat} = 8 \times 10^3 \text{ s}^{-1}$ at 25° C) (Khalifah, 1971; Jewell *et al.*, 1991). HCA III has similar catalytic features to HCA II in that catalysis also occurs in the same two, separate steps (eq 1-1 and 1-2), but the enzyme is resistant to the classic HCA II inhibitors, the sulfonamides (e.g., acetazolamide and HCA III yield a K_i of 40 μM vs. 0.06 μM for HCA II; LoGrasso *et al.*, 1991). In fact, there seems to be a consistent, inverse relationship between the turnover number (k_{cat}) and level of inhibition by sulfonamide of CAs across species (Tufts *et al.*, 2003).

Substrate Binding in the CA Active Site

The precise location of CO_2 binding in the CA active site remains elusive. The binding site has been narrowed down to a hydrophobic region behind the Zn, but the exact interactions that mediate substrate binding are still unknown. The binding of CO_2 is weak and the binding of HCO_3^- is even weaker with approximate K_d of 100 and 500 mM, respectively (Krebs *et al.*, 1993; Lindskog and Silverman, 2000). It is thought that CO_2 binding in the hydrophobic pocket displaces the deep water that is normally hydrogen

bonded to the amide group of Thr199 (Håkansson *et al.*, 1992). CO₂ binding causes it to be polarized by the interaction with the backbone amide of Thr199 in addition to the electrostatic effects exerted by the zinc. This polarization causes the CO₂ to become susceptible to nucleophilic attack by the Zn-bound solvent, as described above.

The hydrophobic substrate binding pocket in HCA II is defined by four residues: Val121, Val143, Leu198, and Trp209 (Lipscomb, 1990; Merz, 1991). The crystal structure of a HCA II mutant (Thr200→His) in complex with HCO₃⁻ (PDB accession code: 1BIC, Xue *et al.*, 1993). The structure shows one of the HCO₃⁻ oxygen atoms acting as a metal ligand, replacing the Zn-bound solvent while the hydrogen is involved in an H-bond with the side chain of Thr199. The second oxygen atom acts as a fifth ligand to the Zn²⁺ and the third seems to be in an H-bond with the backbone amide of His199 (Earnhardt and Silverman, 1998). The structure of this mutant enzyme:product complex implicates Thr199 as a very important residue for orienting water molecules in the active site as well as the direct interaction with HCO₃⁻. A similar complex with the native enzyme has not been obtained, as the native form probably does not exhibit the same extent of binding to HCO₃⁻.

The use of competitive inhibitors to elucidate the substrate-binding site has yielded interesting but conflicting results. Imidazole is a competitive inhibitor of HCA I with a K_i of 20 mM and phenol is a competitive inhibitor of HCA II with a K_i of 10 mM (Khalifah, 1971; Tibell *et al.*, 1985). Crystal structures of HCA I in complex with imidazole and HCA II in complex with phenol show different binding modes of these inhibitors in the active site, making it hard to elucidate the possible binding mode of CO₂ (Kannan *et al.*, 1977; Nair *et al.*, 1994; Earnhardt and Silverman, 1998).

Measuring CA Activity

One of the techniques used to measure CA activity is stopped-flow spectrophotometry under steady state conditions using pH-indicator pairs. This technique is used to determine k_{cat} and K_{M} by measuring the initial rates of CO_2 hydration. The turn-over number k_{cat} reflects the part of catalysis that involves rate-limiting proton transfer, while $k_{\text{cat}} / K_{\text{M}}$ reflects the steps involved in $\text{CO}_2 / \text{HCO}_3^-$ interconversion (Khalifah, 1971; Steiner *et al.*, 1975).

Another technique used to measure CA activity is ^{18}O -exchange and this is done at chemical equilibrium. This method is based on the exchange of ^{18}O between ^{12}C and ^{13}C -containing species of CO_2 and water that occurs because of the hydration-dehydration reaction of CA. Two rates can be determined by this method, R_1 and $R_{\text{H}_2\text{O}}$. The first rate, R_1 , is a measure of the exchange between CO_2 and HCO_3^- at chemical equilibrium. The second rate determined by these methods, $R_{\text{H}_2\text{O}}$, indicates the rate of release from the enzyme of water carrying substrate oxygen. The rate of water release from the active site depends on the rate of proton transfer, thus $R_{\text{H}_2\text{O}}$ is used to measure proton transfer activity (Silverman *et al.*, 1979; Silverman 1982).

Analysis of the catalyzed reaction by CA at steady state and chemical equilibrium has led to a model of its mechanism of action that implicates two ionizing groups in the active site that have pK_a values near 7 (Steiner *et al.*, 1975; Silverman and Lindskog, 1988; Lindskog 1997). One of these groups corresponds to the zinc-bound water, which ionizes to a hydroxyl ion, and is responsible for the interconversion of $\text{CO}_2 / \text{HCO}_3^-$, while the other group, His64, is involved in proton transfer (Tu and Silverman, 1989).

HCA and Human Disease

Due to their wide-spread distribution and various physiological functions, the HCAs support many systemic and cellular $\text{HCO}_3^- / \text{CO}_2$ transport processes as well as biosynthetic pathways. There are not many examples of CA-associated diseases and this reflects its crucial role in so many fundamental life processes. In general, HCA deficiencies are rare and a possible reason is that HCAs are ubiquitously expressed and, in some cases, a different HCA can possibly compensate for the loss of a particular isoform (Sly and Hu, 1995).

A number of genetic variants of HCA I have been described and they generally differ only in one amino acid due to nucleotide substitutions. HCA I variants are less heat stable compared to the wild type version but the catalytic differences are very small or even insignificant. Individuals that either have a variant or lack HCA I completely, show no phenotype (Osborne and Tashian, 1974; Venta, 2000). Despite there being a lot more HCA I than HCA II in RBCs, maybe a loss of HCA I shows no phenotype because HCA II, a very active isoform compared to HCA I (Table 1-1), can functionally compensate for this loss.

HCA II is the most well-studied isoform of all the HCAs and part of the reason is that there are some severe diseases associated with mutant versions of this isoform. One of these is an inherited disease called HCA II deficiency syndrome. It manifests as a lack of erythrocyte HCA II and is associated with osteopetrosis, renal tubular acidosis and, in extreme cases, cerebral calcification that leads to mental retardation (Sly and Hu, 1995). A number of mutations that include nonsense, frameshift, and splicing mutations can lead to a lack of HCA II. Most of these changes cause HCA II deficiency syndrome, but a few other variants have been identified that do not lead to a change in activity or amount of

enzyme (Venta, 2000). The first mutation identified that is associated with the disease results in His107→Tyr substitution and leads to an unstable enzyme that shows a three-fold lower catalytic rate (Venta *et al.*, 1991; Tu *et al.*, 1993). HCA II deficiency syndrome is quite rare and is mostly found in homozygous individuals from families where some level of inbreeding has occurred (Sly and Hu, 1995).

No variants or deficiencies have been described for other HCAs. There is a polymorphism in HCA III where Ile31→Val and variation in activity is predicted based on the location of this substitution. Genetic knock-out studies in mice of murine CA III did not show any phenotype under all the standard muscle-stress tests and longevity of these animals was also not affected (Kim *et al.*, 2004).

Recent studies with CA IV and CA IX single and double knock-out mice implicated these isoforms in buffering and pH regulation of the extracellular space in the hippocampus. The CA IV knock-out mice offspring were produced in lower than expected numbers and females seemed to die more frequently than males during gestation and immediately after birth. CA IX knock-out mice had normal fertility and viability. The double knock-out mice were smaller than wild type and most of the females died before ten months of age. Electrophysiological measurements on brain slices from these animals showed that either one of these membrane-bound CAs can buffer the hippocampus after synaptic firing. A loss of both in the double knock-out mice completely ablated this buffering effect (Shah *et al.* 2005).

CA IX is a highly active isoform with an extracellular CA domain that has functionally been implicated with acid/base balance and intercellular communication. Aberrant expression of CA IX is associated with various tumors and has become of

significant clinical interest. In 2002 Ortova Gut *et al.* constructed a CA IX knock-out mouse and investigated the effects on gastrointestinal epithelia cells. Although these mice had normal stomach pH and acid secretion, they developed gastric hyperplasias and several cysts. These studies highlight the important role of CA IX in cell proliferation and differentiation (Ortova Gut *et al.*, 2002).

CA Inhibitors

Not long after the discovery of CA by Meldrum and Roughton (Meldrum and Roughton, 1932) these authors also investigated inhibition of CA by small molecule inhibitors such as azide and cyanate (Figure 1-8 (a) and (b); Meldrum and Roughton, 1933). In the 1940's, Mann and Keilin found that sulfonamide-based compounds are specific and strong inhibitors of CA (Mann and Keilin, 1940). Figure 1-8 shows several crystal structures of HCA II with small molecule inhibitors as well as the clinically used sulfonamide-based drugs. Since the early findings, many other strong and selective inhibitors have been investigated and these are the aromatic and heterocyclic sulfonamides of the R-SO₂NH₂ or R-SO₂NH(OH) form (Maren, 1967; Maren 1974). All the sulfonamide-based inhibitors interact with CA by the same mechanism: they bind to the metal ion and interfere with the ZnOH⁻ coordination by either displacing or replacing the hydroxide, thus disrupting the interconversion of CO₂ and HCO₃⁻ (Figure 1-8; Bertini and Luchinat, 1983).

Several crystal structures of complexes of various sulfonamide-based inhibitors with CA show similar interactions: the -NH group of the sulfonamide moiety binds directly to the metal and simultaneously donates a hydrogen bond to hydroxyl of Thr199. An oxygen of the sulfonamide also interacts with the amide backbone of Thr199 and thus displaces the deep water (Figure 1-8; Lindskog, 1997). The key group in determining this

displacement/replacement is the hydroxyl of Thr199 and this residue is sometimes referred to as the “gate keeper”.

Examples of clinically important drugs include acetazolamide (Diamox) and brinzolamide (Azopt) that have applications in the treatment of congestive heart failure, altitude sickness and epilepsy (Figure 1-8 (c) and (d); Mansoor *et al.*, 2000). The most common sulfonamide inhibitor in clinical use is acetazolamide, which is a strong inhibitor of HCA II with a K_i value near $0.01 \mu\text{M}$ (Maren and Conroy 1993). Analysis of acetazolamide bound to HCA II revealed the binding interactions of this compound. The thiadiazole ring is in van der Waals contact with Val121, Leu198, and Thr200 and the carbonyl oxygen of the amido group shares a hydrogen bond interaction with the side chain amide of Gln92. The methyl group was shown to interact with the side chain of Phe 131 (Vidgren *et al.*, 1990).

CA inhibitors are commonly prescribed to treat a major symptom of glaucoma, i.e. increased intraocular pressure. The inhibition of CA in the eye by topical application of the drug suppresses the secretion of Na^+ , HCO_3^- , and subsequently production of aqueous humor thus lowering intraocular pressure. (Maren, 1987).

In the following chapters the detailed active site structures of wild type and mutant CAs, and how it relates to proton transfer processes, will be presented. Chapter 2 will deal with pH stability of wild type and site-specific mutants as well as the position of a proton shuttling residue in the active site. These structural features will be correlated with kinetic measurements. In Chapter 3 a different approach will be discussed where, instead of moving the proton shuttle to different positions, mutations were made in the active site of HCA II in order to disrupt solvent networks that mediate proton transfer. That data will

also be correlated with kinetic measurements and implications for proton transfer will be discussed. Chapter 4 will be a discussion of initial experiments performed for the eventual determination of a neutron diffraction structure of perdeuterated wild type HCA II. A detailed structural comparison of overall and active site features between hydrogenated and perdeuterated HCA II will be presented. This work shows proof-of-principle for using HCA II crystals for neutron diffraction experiments. In Chapter 5, the unique binding modes of two novel CA inhibitors, as revealed by X-ray crystallography, will be discussed. These are new compounds and these inhibitors target different residues compared to other canonical CA inhibitors. Chapter 6 will deal with the characterization of a CA from the mosquito, *Aedes aegypti*. This work includes kinetic characterization, inhibition studies, and a homology model of the enzyme. Work presented in Chapters 5 and 6 have implications for the search and design of novel CA inhibitors with possible applications for controlling mosquito populations and treating certain cancers that have associated CA overexpression. Finally, Chapter 7 will contain a summary and concluding remarks on the work presented elsewhere in this thesis, as well as possible future directions for the topics discussed.

Table 1-1. Catalytic constants and subcellular locations of active α -CA isozymes.*

Isoform	k_{cat} (s^{-1})	k_{cat}/K_M ($M^{-1}s^{-1}$)	Subcellular Location	Activity Level
HCA I	2.0×10^5	5.0×10^7	Cytoplasm	Medium
HCA II	1.4×10^6	1.5×10^8	Cytoplasm	High
HCA III	1.0×10^4	3.0×10^5	Cytoplasm	Low
HCA IV	1.1×10^6	5.0×10^7	Membrane-bound	High
Murine CA V	3.0×10^5	3.0×10^7	Mitochondrial	Medium
Rat CA VI	7.0×10^4	1.6×10^7	Secreted	Medium
Murine CA VII	9.4×10^5	7.6×10^7	Cytoplasm	High
HCA IX	3.8×10^5	5.5×10^7	Transmembrane	Medium-high
HCA XII	4.0×10^5	7.4×10^7	Transmembrane	Medium-high

* Adapted from Chegwidien and Carter (2000). HCA XIII and XIV are not included as definitive rate constants have not been determined at the time of this writing.

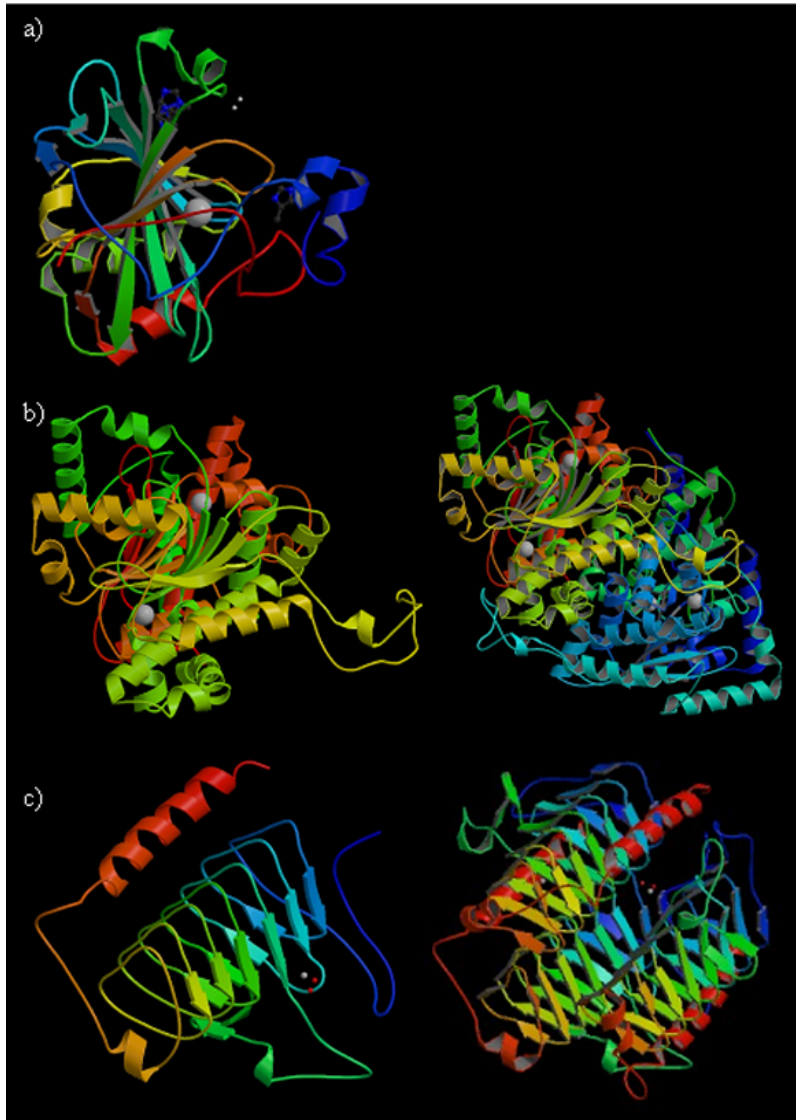


Figure 1-1. Ribbon diagram of CA from three classes. (a) α -class CA; (b) β -class CA; (c) γ -class CA. Panels on the right of (b) and (c) represent the biological assembly as a dimer and trimer, respectively. Coloring is from blue for the N-terminus to red for the C-terminus, gray spheres are Zn^{2+} . Figures were generated and rendered with Bobscrip and Raster3D (Esnouf 1997; Merritt and Bacon, 1997). PDB accession codes for (a), (b), and (c) are 1MOO, 1DDZ and 1QRG, respectively (Duda *et al.*, 2003; Mitsuhashi *et al.*, 2000; Iverson *et al.*, 2000).

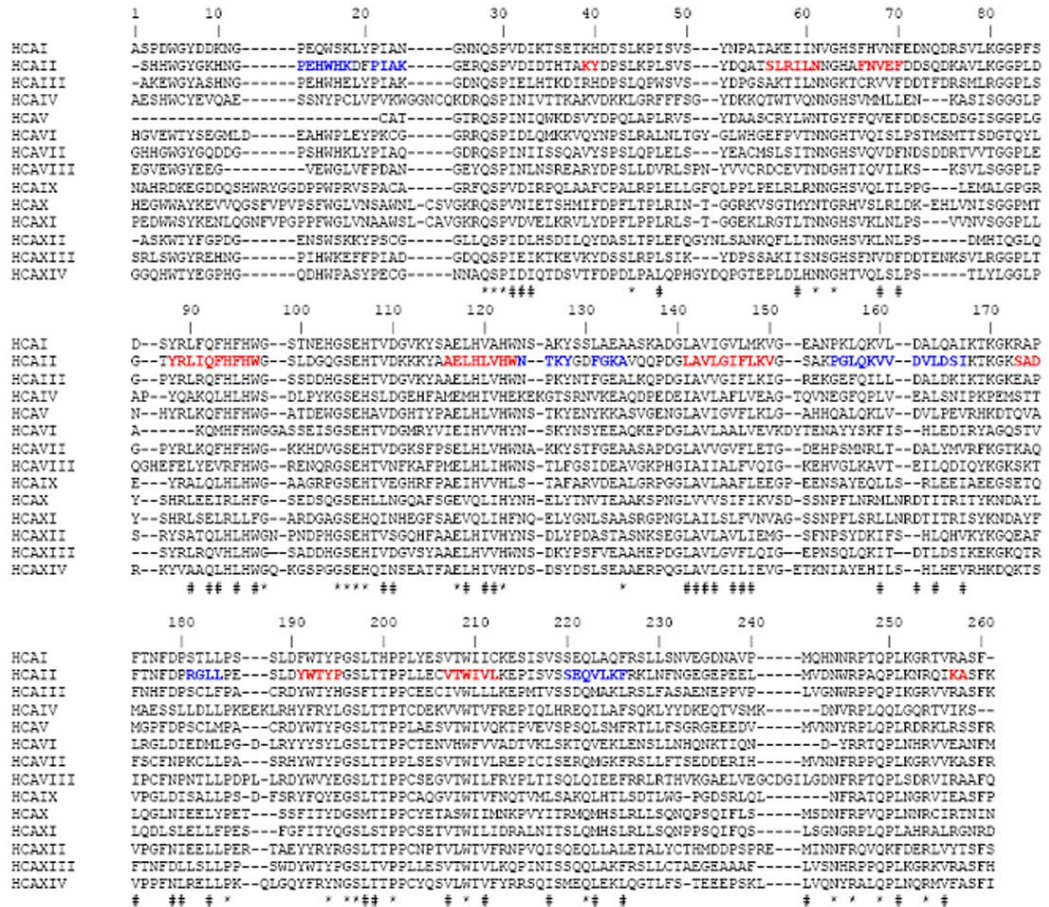


Figure 1-2. Multiple sequence alignment of fourteen HCA domains. Alignment was performed using ClustalW and residue numbering is according to HCA II (Thompson *et al.*, 1994). Conserved and similar substituted residues are indicated by * and #, respectively. Regions in bold that are red and blue signify β -strand and α -helical regions of HCA II.

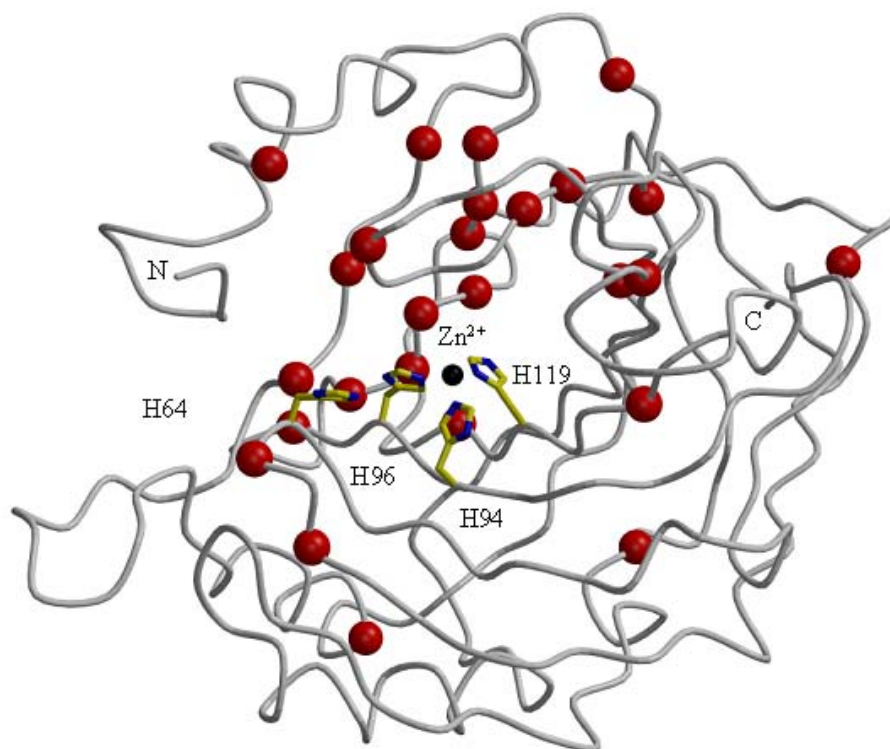


Figure 1-3. Conservation of HCAs. Gray ribbon backbone representation of HCA II with completely conserved residues of fourteen HCAs indicated as red spheres. Active site residues are shown as yellow ball-and-stick (HCA II numbering), the zinc atom is a black sphere and the N- and C-terminus as labeled.

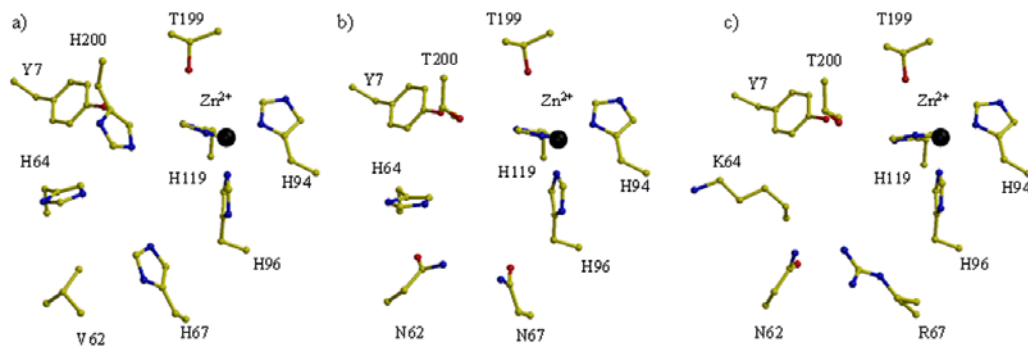


Figure 1-4. Active sites of HCA I, II, and III. (a) HCA I, (b) HCA II, and (c) HCA III. Active site residues are in yellow ball-and-stick and are as labeled, zinc atom = black sphere. Figure was generated with Bobscrip and Raster3D (Esnouf, 1997; Merritt and Bacon, 1997).

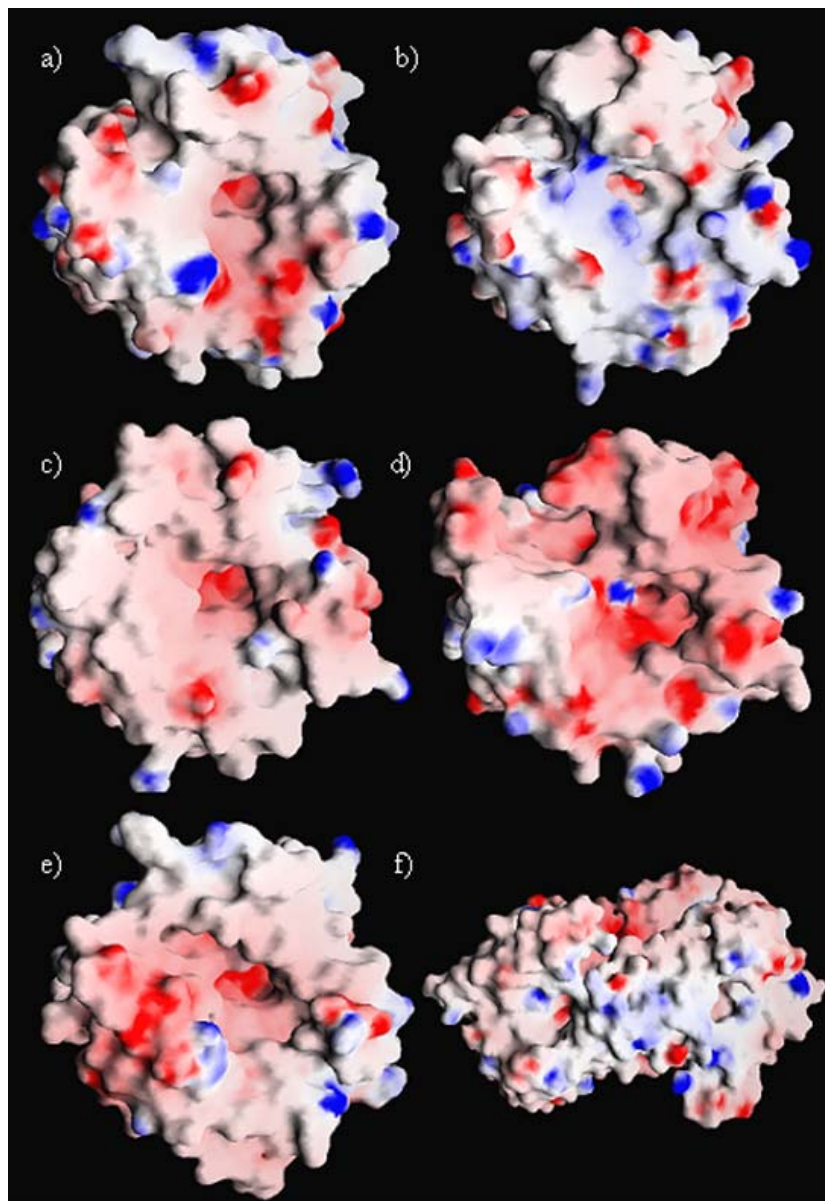


Figure 1-5. Molecular and electrostatic surface potentials of HCAs. (a) HCA II; (b) HCA III; (c) HCA VI; (d) HCA-RP VIII; (e) HCA IX; (f) HCA XII dimer. All models are shown in the same orientation with the active site in the center. Negative and positive charge is represented by red and blue, respectively. Figures were generated with GRASP (Nicholls *et al.*, 1991).

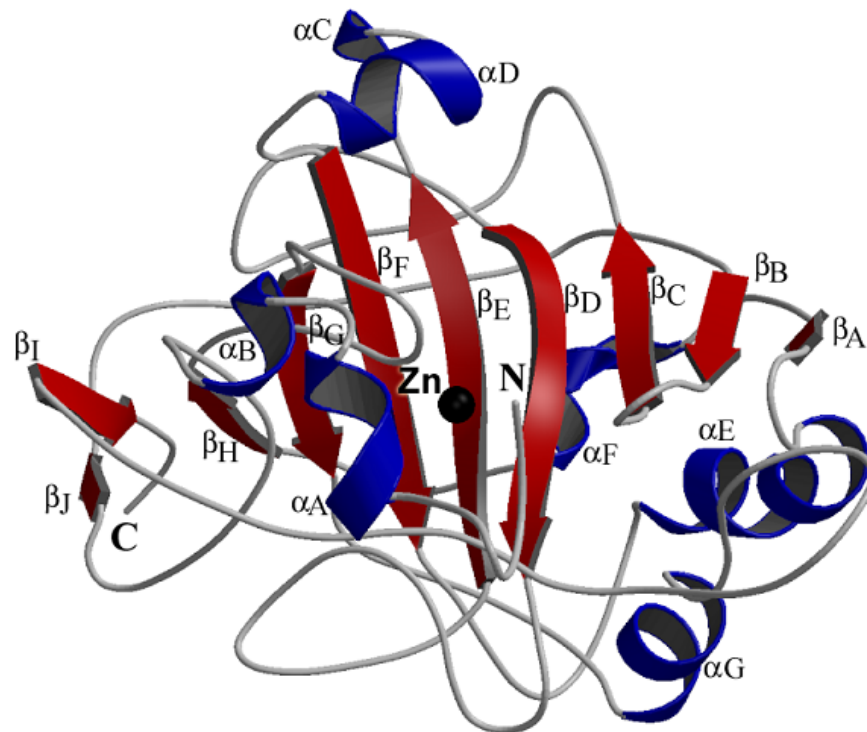


Figure 1-6. Ribbon diagram of HCA II with secondary structure elements. Red regions are β -strands ($\beta A - \beta J$), blue regions are α -helices ($\alpha A - \alpha G$). Zinc atom is shown as a black sphere and the N- and C-termini are labeled. Figure generated with Bobscript and Raster3D (Esnouf, 1997; Merritt and Bacon, 1997).

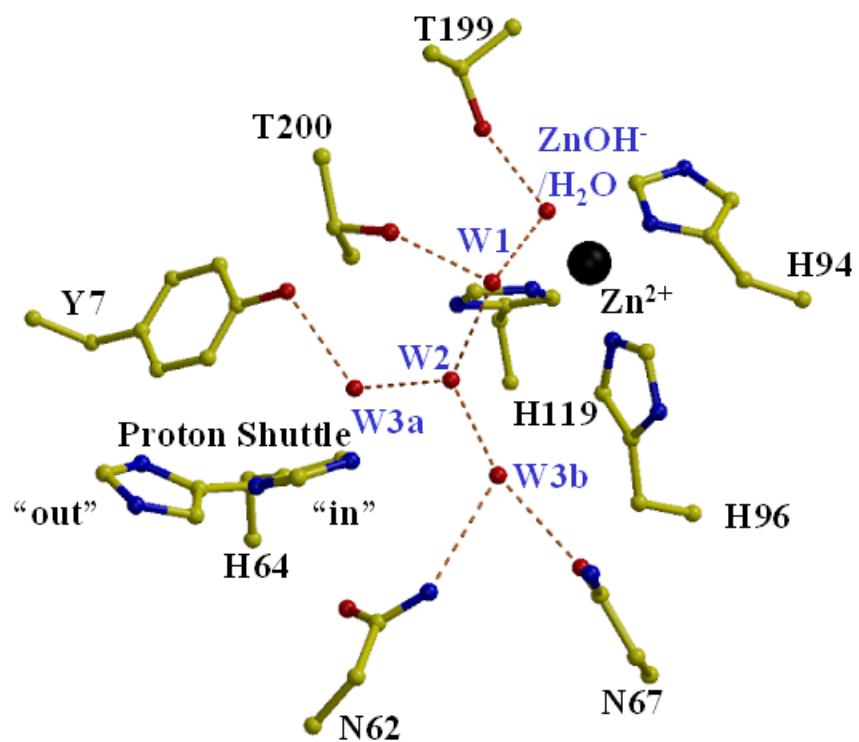


Figure 1-7. Active site of wild type HCA II. Catalytic residues are shown in yellow ball-and-stick, solvent molecules = red spheres, zinc atom = black sphere. Residues are as labeled and inferred hydrogen bonds are indicated by the dashed orange lines. Figure was generated with Bobscrip and rendered with Raster3D (Esnouf, 1997; Merritt and Bacon, 1997).

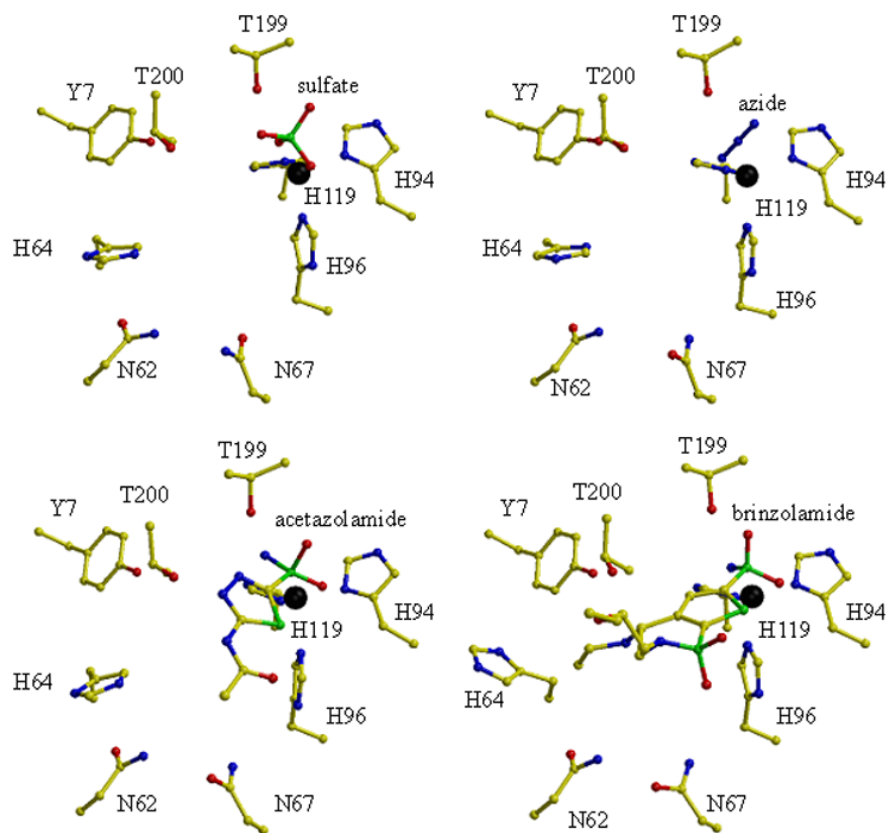


Figure 1-8. HCA II in complex with inhibitors. (a) Sulfate, (b) Azide, (c) acetazolamide, and (d) brinzolamide. HCA II active site residues are shown as yellow ball-and-stick and the black sphere is the zinc atom. PDB accession codes used (a)-(d): 1T9N, 1RAY, 1YDA, and 1A42 (Fisher *et al.*, 2005; Jonsson *et al.*, 1993; Nair *et al.*, 1995; Stams *et al.*, 1998). Figure was generated with Bobscrip and Raster3D (Esnouf, 1997; Merritt and Bacon, 1997).

CHAPTER 2
STRUCTURAL AND KINETIC ANALYSIS OF PROTON SHUTTLLING IN HUMAN
CARBONIC ANHYDRASE II

Introduction

Human carbonic anhydrase II (HCA II) is one of the most efficient enzymes with a turnover number near 10^6 s^{-1} and k_{cat}/K_M of $1 \times 10^8 \text{ M}^{-1}\text{s}^{-1}$. This fast rate indicates that the catalysis is limited by the rate of diffusion of substrate into the active site of HCA II (Khalifah, 1971). The overall catalytic mechanism was presented in some detail in Chapter 1 and will only be discussed here briefly. The first step in the interconversion of CO_2 and HCO_3^- is the hydration of CO_2 by the zinc-bound OH^- which is then followed by the displacement of HCO_3^- by water. The second step is the deprotonation of the zinc-bound water to regenerate the zinc-bound OH^- and involves both intramolecular and intermolecular proton transfer steps (Silverman, 1982; Silverman and Lindskog, 1988).

Imidazole and derivatives act as nucleophilic and general base catalysts. The structure of imidazole, with two almost identical N atoms, allow it to pick up a proton off one of its N atoms forming a cation and then delivering it to the second N atom. As the functional group of histidine, it is commonly associated with proton transport in proteins (Scheiner and Yi, 1996). His64 in HCA II acts as a proton shuttle between the zinc-bound solvent and buffer in solution and mutation of His64 to an alanine reduces enzymatic activity 10-50 fold. This mutation does not affect the hydration/dehydration part of catalysis, but the observed decrease in proton transfer can be rescued by supplying free imidazole in the reaction buffer. It has been postulated that the proton transfer between

the zinc-bound water and His64 occurs through intervening water molecules (Venkatasubban and Silverman, 1980; Tu *et al.*, 1989).

In other protein systems, such as cytochrome c oxidase and the bacterial photosynthetic reaction center, hydrogen-bonded water chains have been observed in several crystal structures and the location and geometry of these chains suggest that they participate in proton transfer reactions (Pomès and Roux, 1996). These chains are thought to be effective in long-range proton translocation and such hydrogen-bonded water chains have been called proton wires (Nagle and Morowitz, 1978). Protons do not move by diffusion as a hydrated proton (hydronium ion, H_3O^+), instead the high observed mobility of protons is thought to occur from successive protonation-deprotonation events. In these cases, protons “hop” from oxygen to oxygen along a pre-existing hydrogen-bonded water chain in a Grotthus-type mechanism (Pomès and Roux, 1996). Similar proton wires are observed in the active site of HCA II and these water molecules bridge the distance between the zinc-bound solvent and the proton shuttle, His64. The water molecules that span the 8 Å distance between zinc and His64 appears to be hydrogen bonded to each other but not to the imidazole group of His64 (Eriksson *et al.*, 1988). The proton transfer path in HCA II was first described by Steiner *et al.* based on assays that showed significant solvent hydrogen isotope effects. These experiments indicated that maximum velocity, k_{cat} , was limited in rate by the intermolecular proton transfer (Steiner *et al.* 1975).

The Brønsted relation, as applied to proton transfer, is a linear free-energy relationship that correlates the rate constant (k_{B}) for proton transfer with the difference in

acid/base strength (ΔpK_a) of the proton acceptor and donor, is shown in eq 2-1

(Silverman *et al.*, 1993; Silverman, 2000)

$$\log(k_B) = \beta[pK_a(\text{acceptor}) - pK_a(\text{donor})] + \text{constant} \quad (2-1)$$

The slope (β) of a Brønsted plot of $\log(k_B)$ versus ΔpK_a is used to investigate a reaction mechanism and can be used as an estimate of the extent of proton transfer between reactants and products in the transition state. Observed variation in the slope over a range of pK_a values has been interpreted through Marcus theory and yields 1) an intrinsic energy barrier for proton transfer, and 2) two work terms, w^f and w^p , that quantitate the energy required for aligning the reactants in the reaction complex in both the forward and reverse directions, respectively (Silverman *et al.*, 1993; Silverman, 2000; Kresge and Silverman, 1999).

Application of Marcus rate theory to Brønsted plots of the proton transfer processes in carbonic anhydrase has provided a way to experimentally determine the intrinsic energy barrier as well as separating different thermodynamic contributions from the observed activation energy (Silverman, 2000). The rate constant for proton transfer is maximal when the difference between the pK_a values of the proton acceptor and donor is near zero (Rowlett and Silverman, 1982; Silverman *et al.*, 1993). Further analysis of free energy plots has shown there is a significant energetically unfavorable pre-equilibrium that exists before a very rapid proton transfer event occurs. It was determined that catalysis proceeds with an intrinsic free energy of activation that is very small (~ 1.5 kcal/mol) but with a large work function w^f (~ 10 kcal/mol) (Kresge and Silverman, 1999; Silverman, 2000). The magnitude of this work function accounts for the relative low proton transfer rate in HCA II, at most 10^6 s^{-1} , compared to maximal rates of 10^{11} s^{-1}

measured for proton transfer between naphthol-related photo acids to acetate in solution (Pines *et al.*, 1997). It is not well understood what processes add to the work functions, but in HCA II this may involve the rearrangement and formation of a hydrogen bonded water chain as well as orientation of His64. These factors imply that setting up the active site environment for proton transfer takes far more energy than the actual proton transfer itself (Silverman *et al.*, 1993).

The shuttling of protons between bulk solvent and the zinc-bound solvent molecule may require some conformational mobility of His64 as the proton donor/acceptor. Considerable support for this comes from various crystal structures in which the proton shuttle residue His64 in HCA II and Glu84 in the archaeal carbonic anhydrase from *Methanosarcina thermophila* show two conformational rotamers in the active-site cavity (Nair and Christianson, 1991; Tripp and Ferry, 2000; Iverson *et al.*, 2000). A chemically modified cysteine residue acting as a proton shuttle in a mutant of CA V also shows evidence of multiple orientations (Jude *et al.*, 2002).

Structural studies by Nair and Christianson showed that His64 occupies different positions depending on the pH. At pH 5.7 the side chain of His64 rotates around χ_1 by 64° to occupy what is termed the “out” position ($\sim 12 \text{ \AA}$ away from the active site) compared to the structure at pH 8.5 that shows the side chain of His64 pointing towards the active site ($\sim 8 \text{ \AA}$ away from the active site) in what is known as the “in” conformation (Nair and Christianson, 1991). A similar observation was made for the Thr200→Ser mutant at pH 8.0 where His64 was observed to occupy an even further “out” position due to a rotation about χ_1 of 105° (Krebs and Fierke, 1991). In both cases,

the conformational mobility of His64 as a function of pH or the mutation at position 200 did not seem to adversely affect proton transfer kinetics (Nair and Christianson, 1991).

The current understanding of the requirements for rapid proton transfer, as measured for HCA II, involves several aspects that could be investigated by comparisons of kinetics and structure. The kinetic effect of the location of a histidine proton shuttle has been studied by introducing histidine residues at different positions in the active-site cavity of HCA II. These results show that a histidine residue at sites other than position 64 is able to participate in proton transfer; specifically, His67 appears capable of more efficient proton transfer than His62 (Liang *et al.*, 1993).

To further characterize and understand the relationship between efficient proton transfer and the existence of proton wires in HCA II, detailed comparisons of kinetics and active site water structure were conducted. These included structure determinations of wild-type HCA II and HCA II mutants (H64A/N62H and H64A/N67H) from pH 5.1 to 10.0. These data were correlated with catalytic activities that were measured by the exchange of ^{18}O between CO_2 and water from pH 5.0 to 9.0 as catalyzed by these enzymes to determine what common structural features are important for proton transfer.

Materials and Methods

Enzymes

Plasmids with the appropriate mutations in the cDNA of HCA II were provided by Professor Sven Lindskog, Umeå University, Sweden. Expression of wild type and mutant HCA II was performed in *E. coli* BL21(DE3) pLysS cells that were grown to an optical density of ~ 0.60 as measured at a wavelength of 600 nm. Protein expression was induced by the addition of 1 mM isopropyl- β -D-1-thiogalactopyranoside (IPTG) and 1 mM zinc sulfate was also added for uptake in the expressed protein. At 4 hours post-induction,

cells were harvested by centrifugation and the cell pellets frozen at $-20\text{ }^{\circ}\text{C}$ overnight. Cell pellets were lysed by freeze/thawing and solubilized in 0.2 M sodium sulfate, 50 mM Tris-Cl (pH 9.0). The soluble cell fraction was obtained by centrifuging the lysates at $100,000 \times g$ for 1 hour at $4\text{ }^{\circ}\text{C}$. Enzymes were further purified from the supernatant by affinity chromatography using p-amino-methyl-benzenesulfonamide (pAMBS; a specific binder to the active site of α -CAs) coupled to agarose beads as described elsewhere (Khalifah, 1977). Purity of the protein was verified by electrophoresis on a 12% polyacrylamide gel stained with Coomassie. The concentration of HCA II was determined by measuring the absorbance at 280 nm and using a molar absorptivity of $5.4 \times 10^4 \text{ M}^{-1}\text{cm}^{-1}$ (Coleman, 1967).

Crystallography

Crystals of wild type and mutant HCA II were obtained using the hanging drop method (McPherson, 1982). The crystallization drops were prepared by mixing 5 μl of protein (10.5 mg/ml concentration in 50 mM Tris-HCl, pH 7.8) with 5 μl of the precipitant solution (50 mM Tris-HCl, pH 7.8, 2.5-2.9 M ammonium sulfate) at $4\text{ }^{\circ}\text{C}$ against 600 μl of the precipitant solution. Useful crystals were observed within five days after crystallization setup. The pH of the wild type crystals were obtained by equilibrating crystals in appropriate buffers (50 mM sodium acetate, pH 5.1; 50 mM MES, pH 6.1; 50 mM Tris-HCl, pH 7.0, 7.8 and 9.3; 50 mM CAPS, pH 10.0) and 3.0 M ammonium sulfate. The pH of the double mutant crystals were obtained by using the same approach as above using the buffers (50 mM Tris-HCl, pH 6.0 and 7.8) and 3.0 M ammonium sulfate. Crystals were allowed to equilibrate for 4-12 hours at 4°C before data collection

to ensure that complete solvent exchange in the crystal lattice occurred (the pH stated was that as measured at the start of the experiment).

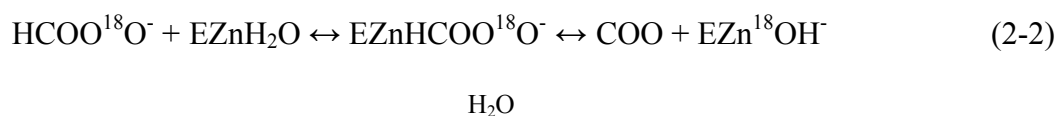
X-ray-diffraction data sets were obtained using an R-AXIS IV++ image plate system with Osmic mirrors and a Rigaku HU-H3R Cu rotating anode operating at 50 kV and 100 mA. The detector to crystal distance was set to 100 mm for H64A/N67H, and 120 mm for H64A/N62H and wild type HCA II X-ray data collection. Each data set was collected at room temperature from a single crystal mounted in a quartz capillary. The oscillation steps were 1° with a 3 minute exposure per image. X-ray data processing was performed using DENZO and scaled and reduced with SCALEPACK software (Otwinowski and Minor, 1997). Data set statistics for the wild type and mutant structures at different pHs are given in Tables 2-1 and 2-2, respectively.

All models were built using the program O, version 7 (Jones *et al.*, 1991). Refinement was carried out with the software package CNS, version 1.1 (Brünger *et al.*, 1998). The wild type HCA II structure (Protein Data Bank accession number 2CBA; Håkansson, 1992), which was isomorphous with all the data sets collected, was used to phase the data sets. To avoid phase bias of the model, the zinc ion, mutated side chains and water molecules were removed. After one cycle of rigid body refinement, annealing by heating to 3000 K with gradual cooling, geometry-restrained position refinement, and temperature factor refinement, the $2F_o - F_c$ Fourier maps were generated. These density maps clearly showed the position of the zinc and the mutated residues, which were subsequently built into the respective models. After several cycles of refinement, solvent molecules were incorporated into the models using the automatic water-picking program in CNS until no more water molecules were found at a 2.0σ level. Refinement of the

models continued until convergence of the R_{work} and R_{free} was reached. Final model statistics for wild type and mutant structures are given in Tables 2-1 and 2-2, respectively.

Activity Analysis by ^{18}O Exchange

These assays were performed by Dr. Chingkuang Tu in the Silverman lab and the details of determining the rate constants for catalysis by HCA II are discussed in detail below. The ^{18}O exchange method is based on the measurement, using membrane-inlet mass spectrometry, of the exchange of ^{18}O between CO_2 and H_2O at chemical equilibrium (Silverman, 1982) (eqs 2-2 and 2-3).



An Extrel EXM-200 mass spectrometer with a membrane inlet probe was used to measure the isotopic content of CO_2 . Solutions contained a total concentration of all species of CO_2 of 25 mM and the ionic strength was maintained by the addition of 0.2 M sodium sulfate. This approach yields two rates for the ^{18}O exchange catalyzed by carbonic anhydrase. The first is R_1 , the rate of exchange of CO_2 and HCO_3^- at chemical equilibrium, as shown in eq 2-4.

$$R_1/[E] = k_{\text{cat}}^{\text{ex}}[S]/(K_{\text{eff}}^{\text{S}} + [S]) \quad (2-4)$$

Here $k_{\text{cat}}^{\text{ex}}$ is a rate constant for maximal interconversion of substrate and product, $K_{\text{eff}}^{\text{S}}$ is an apparent binding constant for substrate to enzyme, and $[S]$ is the concentration of substrate, either CO_2 or HCO_3^- . The $k_{\text{cat}}^{\text{ex}}/K_{\text{eff}}^{\text{S}}$ ratio is, in theory and in practice, equal to $k_{\text{cat}}/K_{\text{M}}$ obtained by steady state methods. The binding of CO_2 and HCO_3^- to the active site of HCA II is weak (Krebs *et al.*, 1993), and in this work too it is assumed that $[\text{CO}_2]$

$\ll K_{\text{eff}}^S$. The pH dependence of k_{cat}/K_M depends on the ionization state of the zinc-bound water, as shown in eq 2-5.

$$k_{\text{cat}}/K_M = (k_{\text{cat}}/K_M)_{\text{max}}(1 + [\text{H}^+]/(K_a)_{\text{ZnH}_2\text{O}})^{-1} \quad (2-5)$$

A second rate determined by the ^{18}O exchange method is $R_{\text{H}_2\text{O}}$, the rate of release from the enzyme of water bearing substrate oxygen (eq 2-3). This is the component of the ^{18}O exchange that is enhanced by exogenous proton donors (Silverman, 1982). The pH dependence of $R_{\text{H}_2\text{O}}/[E]$ is often bell-shaped, consistent with the transfer of a proton from a single predominant donor to the zinc-bound hydroxide. In these cases, the pH profile is adequately fit by eq 2-6 in which k_B is a pH-independent rate constant for proton transfer, and $(K_a)_{\text{donor}}$ and $(K_a)_{\text{ZnH}_2\text{O}}$ are the noninteracting ionization constants of the proton donor BH^+ of eq 2-3 and the zinc-bound water.

$$k_B^{\text{obs}} = k_B / \{ [1 + (K_a)_{\text{donor}}/[\text{H}^+]] [1 + [\text{H}^+]/(K_a)_{\text{ZnH}_2\text{O}}] \} \quad (2-6)$$

Results and Discussion

Crystallography

All crystals of wild type, H64A/N62H, and H64A/N67H HCA II were isomorphous in the $P2_1$ space group with mean unit cell dimensions: $a = 42.7 \pm 2.0 \text{ \AA}$, $b = 41.6 \pm 1.0 \text{ \AA}$, $c = 72.9 \pm 2.0 \text{ \AA}$, and $\beta = 104.6 \pm 2.0^\circ$. Wild type crystals from pH 5.1 to 10.0 all diffracted to 2.0 \AA , while crystals of H64A/N62H and H64A/N67H diffracted to between 1.63 and 1.90 \AA . Tables 2-1 and 2-2 contain summaries of the diffraction data set and model statistics from wild type and mutant HCA II crystals, respectively.

A least squares superposition of wild type HCA II structures (at pH 5.1, 6.1, 7.0, 9.0, and 10.0) onto the structure at pH 7.8 indicated no significant differences between them and had an average root mean square deviation (rmsd) of less than 0.1 \AA for all atoms. Superposition of H64A/N62H HCA II at pH 6.0 and 7.8, as well as H64A/N67H

at pH 6.0 and 7.8, onto the pH 7.8 wild type HCA II structure showed an average rmsd near 0.15 Å for all atoms. When the mutants were compared to each other, the rmsd was only 0.07 Å.

The rmsd of bond lengths and angles for all structures were between 0.038 and 0.005 Å and between 1.3 and 2.1°, respectively. Ramachandran statistics for all amino acids were ~ 90% in most favored region and ~ 10% in the additionally allowed region with no residues in the generously and disallowed regions.

Effect of pH on the Wild Type HCA II Active Site

The tetrahedral coordination of the zinc atom by His94, His96, His199, and a non-protein atom (either H₂O/OH⁻ or sulfate) was intact over the broad pH range from 5.1 – 10.0 used in this study. At pH 5.1 a sulfate ion bound directly to the zinc atom was observed (Figure 2-1). The sulfate binding displaced the zinc-bound H₂O/OH⁻ but had no effect on the coordination of the zinc atom. In all the wild type structures determined from pH 5.1 to 10.0, there was a highly conserved, well-ordered water network extending from the zinc-bound solvent (or sulfate) to the imidazole of His64. These networks consist of four water molecules, W1, W2, W3a, and W3b. W1 is hydrogen bonded to W2, which is in turn hydrogen bonded to W3a and/or W3b. W1 is held in place by interactions with not only W2, but also with the hydroxyl group of Thr200. W3a and W3b interact with Tyr7 and Asn62/Asn67, respectively (Figure 2-1). W2 is the only water molecule held entirely in place by interactions with other water molecules. The configuration of these networks leads to two possibilities for a proton transfer pathway from the zinc-bound solvent to the proton shuttle His64; W1 → W2 → W3a → His64 or W1 → W2 → W3b → His64. However, the distances between the distal waters, W2, W3a, and W3b, and His64 were all too long (> 3.4 Å) to constitute viable hydrogen

bonds and it is unclear how the proton will make the jump from one of these waters to His64. Other studies with HCA VI alkylated with an imidazole-containing reagent showed a completed, hydrogen-bonded water chain and was associated with a very small rate of proton transfer (10^3 s^{-1} compared to 10^6 s^{-1} for His64 in wild type HCA II; Jude *et al.*, 2002). Thus, the observation in the crystal structure of a completed, hydrogen-bonded water chain that links the proton donor and acceptor is not a requirement for the rapid proton shuttling on the scale determined for HCA II.

It should also be noted that the hydrogen bonds in crystal structures are assigned based on the distance and geometries between hydrogen bond donors and acceptors. Hydrogen atoms are invisible by X-ray crystallography at these resolutions and subsequently these assignments can be extremely misleading as there is no way to observe the ionization of waters or amino acid side chains. Currently, the only definitive way to observe hydrogen bond are with either ultra-high resolution ($< 1 \text{ \AA}$) X-ray crystallography or macromolecular neutron diffraction studies.

The only observed structural difference between wild type HCA II at the various pHs was the positional occupancy of His64 (Figure 2-1). The occupancies of His64 were determined from $F_o - F_c$ omit maps, where His64, W1, W2, W3a, and W3b were removed for the calculation to avoid model bias. The residual electron density volumes were used to determine the relative occupancies of His64 in the “in” and “out” positions. At pH 5.1, His64 was predominantly in the “in” position and this could be due to electrostatic effects exerted by the sulfate ion. Consequently, the “out” conformer was modeled as a water molecule. At pH 6.1, 7.0, and 7.8 the occupancies were 60, 70, and 80% in the “in” conformation. There was no increased occupancy at higher pH and at pH 9.0 and 10.0

His64 was still 80% in the “in” conformation (Figure 2-1). The overall trend from this data shows that with increasing pH, His64 favors the “in” conformation and this result is consistent with the work of others (Nair and Christianson, 1991). The side chain torsion angles for the “in” and “out” conformers were ($\chi_1 = 48^\circ$, $\chi_2 = -98^\circ$) and ($\chi_1 = -43^\circ$, $\chi_2 = -90^\circ$), respectively. Thus, over a range of pHs it was observed that His64 occupies both positions with equivalent occupancy and this phenomenon is consistent with its function as a proton shuttle. The physiological function of His64 as a shuttle in catalysis is supported by these observations as hydration and dehydration occur at nearly the same rates. Structural and kinetic studies with 4-methylimidazole and H64A HCA II suggest that binding of this exogenous proton donor/acceptor to a position that mimics the “out” position of His64, is not as efficient in proton transfer as His64. Perhaps the motion of this residue is somehow related to its efficacy as a proton shuttle. When His64 occupies the “in” position it can pick up an excess proton from one of the active site solvent molecules and then move rapidly to the “out” position and deliver it to bulk solvent.

Effect of pH on the Mutant HCA II Active Site

The hydrogen bonding pattern and solvent network is different for the H64A/N62H and H64A/N67H HCA II mutants compared to each other and wild type (Figure 2-2). Even though both mutants display similar solvation levels in the active site, the organization of the water molecules has been altered. It is interesting that both mutants have sulfate bound at pH 6.0, while in wild type sulfate was only observed at pH 5.1 (Figure 2-2 (a), (c)). However, at pH 7.8 there is not sulfate present in either wild type or mutant HCA II. The sulfate binds in the same orientation in all the structures determined in this study: it displaces the zinc-bound solvent and simultaneously engages in a hydrogen bond with the hydroxyl group of Thr199, thus maintaining the tetrahedral

coordination of the zinc. Sulfate has been shown to be inhibitory to HCA II at low pH and it was thought that it interacted with the zinc (Simonsson and Lindskog, 1982). These data suggest that the inhibition at low pH by sulfate may be due to the binding of a protonated sulfate ion in a similar mode to other protonated inhibitors such as HSO_3^- and the sulfonamide drugs (Liljas *et al.*, 1994).

There are several structures of mutant HCA II in complex with sulfate but the results presented here show for the first time a sulfate bound to the zinc center of wild type HCA II and this occurs only at very low pH (Xue *et al.*, 1993(a)).

In both mutants the introduced His side chains extend into the active site cavity towards the zinc. In contrast to His64 in wild type HCA II, neither one of the His in the mutants display any conformational mobility. In H64A/N62H HCA II at pH 7.8 there is a complete hydrogen bonded solvent network that extends from the zinc-bound solvent to His62 (W1 \rightarrow W2 \rightarrow W3b; Figure 2-2 (b)). Due to the long distance (3.2 Å) between W3b and His62 this interaction represents a very weak hydrogen bond. The water W3b that His62 is hydrogen bonded to is also connected to the side chain of N67.

In H64A/N67H HCA II at pH 7.8, His67 is connected directly to W2 with a bond distance of 3.2 Å and W3b has been completely displaced by the side chain of His67 (W1 \rightarrow W2; Figure 2-2). His67 is also hydrogen bonded to the side chain of N62 and this interaction might prohibit rotational freedom of the His during catalysis.

The His at position 67 is ~ 6.6 Å away from the zinc while His62 is over 8 Å away (Table 2-3). This extra distance is spanned by an additional water molecule and the solvent network appears more branched in H64A/N62H HCA II compared to H64A/N67H HCA II. The observed network of two water molecules between the proton

donor and acceptor seen in H64A/N67H HCA II at pH 7.8 is similar to one of the possible pathways (W1 → W2) as seen in wild type HCA II from pH 6.1 to 10.0, except that in wild type all of the distal waters are over 3.2 Å away from the proton shuttle.

Catalysis

The pH dependence of the hydration/dehydration rate, $k_{\text{cat}}/K_{\text{M}}$, and the proton transfer-dependent rate constant, $R_{\text{H}_2\text{O}}/[\text{E}]$, for the release of ^{18}O labeled water from the active site, was measured. The pH range was from pH 5.0 to 9.0 for wild type and both mutants. These data was compared to ^{18}O exchange data obtained for a mutant, H64A HCA II, that lacks a proton shuttle in the active site. The data for wild type HCA II shows that the enzyme is remarkably stable and highly active over the pH range studied (Figures 2-3 and 2-4).

The data in Figure 2-3 show the $k_{\text{cat}}/K_{\text{M}}$ for CO_2 hydration for each of the mutants (H64A, H64A/N62H, and H64A/N67H HCA II) superposed onto data for wild type HCA II. The data shows that the mutants have very similar values to wild type and this serves as a control indicating that the mutations do not cause gross structural changes that interfere with the first step of catalysis.

The data in Figure 2-3 were fit to a single ionization with pK_{a} values as given in Table 2-3 and these are characteristic of the pK_{a} of the zinc-bound water (Lindskog, 1997). The pK_{a} for the proton donor and acceptor in wild type HCA II are very close in value to each other (6.9 and 7.2) and this might be another requirement for efficient proton transfer between them. In both mutants the differences between the pK_{a} values are larger compared to wild type and could contribute to the lower observed rate of proton transfer between His and the zinc-bound water (Table 2-3).

The pK_a values for the zinc-bound water given in Table 2-3 are in agreement with values obtained by others that measured the pH dependent esterase activity of HCA II (Liang *et al.*, 1993). For H64A/N67H HCA II it appears from the plot in Figure 2-3 that a single pK_a is not sufficient to fit the data and this implies that a second ionization, probably that of His67, is influencing the k_{cat}/K_M .

The proton transfer activity data shown in Figure 2-4 indicate that all three mutants are significantly impaired compared to wild type HCA II, with H64A being the slowest. These data showed only slightly better rates for H64A/N62H HCA II compared to H64A HCA II (Figure 2-4). However, there was significant enhancement of catalysis for H64A/N67H HCA II at $pH < 6.5$ compared with that of H64A HCA II. The solid lines of Figure 2-4 represent least-squares fits to eq 6, which assumes that the observed enhancement of $R_{H_2O}/[E]$ above that of H64A HCA II is due to the proton transfer activity of the inserted His to the zinc-bound hydroxide.

Other studies using stopped flow methods at steady state have shown that this mutant had a turnover number, k_{cat} , that is 20% of that observed for wild type (Liang *et al.*, 1993). The data presented here was determined by ^{18}O exchange methods at chemical equilibrium and showed that this mutant had a maximal rate constant for proton transfer that is 25% that of wild type (Table 2-3). It should be noted that there is typically up to 20% error in these measurements and this is due to the scatter of the points and the limited pH range.

Conclusion

HCA II shows remarkable structural and kinetic stability over a wide range of pH (5.1 to 10.0). The only structural difference is the side chain of His64 that displays two conformational states that are almost equally occupied at physiological pH. In wild type,

H64A/N62H, and H64A/N67H HCA II structures there is either no completed hydrogen-bonded water chain between proton donor and acceptor or the distal water is very weakly bound to the proton shuttling residue. A His inserted at position 67 shows appreciable proton shuttling activity (25% of wild type), compared to a His at position 62 (4% of wild type). In these examples, the distance between the proton shuttling His and the zinc-bound solvent and the number of waters that spans this distance, might be more important for efficient proton shuttling than observing a complete hydrogen-bonded chain of waters to the His residue. The results suggest that the optimal distance for the His to the zinc is between 6.6 and 7.5 Å and that the number of intervening water molecules should not exceed two for the support of efficient and fast proton transfer.

Table 2-1. Data set and model statistics for wild type HCA II from pH 5.1 to 10.0.

HCA II	pH 5.1	pH 6.1	pH 7.0	pH 7.8	pH 9.0	pH 10.0
Resolution (Å)	20.0 – 2.00 (2.07 – 2.00)*	20.0 – 2.00 (2.07 – 2.00)	20.0- 2.00 (2.07 – 2.00)	20.0 – 2.00 (2.07 – 2.00)	20.0 – 2.00 (2.07 – 2.00)	20.0 – 2.00 (2.07 – 2.00)
Total Number of Unique Reflections	15898 (1546)	16365 (1575)	15878 (1554)	16212 (1539)	16751 (1665)	16714 (1598)
Completeness (%)	93.1 (90.0)	95.9 (94.0)	93.5 (91.8)	95.1 (91.9)	98.6 (99.2)	97.8 (95.4)
Redundancy	1.9 (1.9)	2.7 (2.7)	2.3 (2.3)	3.2 (3.2)	2.6 (2.5)	2.6 (2.6)
$R_{\text{symm}}^{\dagger}$	0.063 (0.199)	0.120 (0.447)	0.051 (0.140)	0.073 (0.217)	0.092 (0.198)	0.081 (0.143)
$R_{\text{cryst}}^{\ddagger} / R_{\text{work}}^{\text{§}}$	0.195/0.209	0.145/0.205	0.130/0.184	0.128/0.201	0.134/0.173	0.134/0.175
Ave B-factor (Å ²)	16/20/28	23/27/30	18/22/28	14/18/27	17/21/28	17/21/28
Main/side/solvent Number of solvent	112	91	112	150	112	115

* Data in parenthesis are for the highest resolution shell.

$$\dagger R_{\text{symm}} = \sum |I - \langle I \rangle| / \sum \langle I \rangle$$

$$\ddagger R_{\text{cryst}} = \sum | |F_o| - |F_c| | / \sum |F_o|$$

§ R_{free} is calculated the same as R_{cryst} except it is for data omitted from refinement (5% of reflections for all data sets)

Table 2-2. Data set and model statistics for H64A/N62H and H64A/N67H HCA II at pH 6.0 and 7.8.

HCA II	H64A/N62H pH 6.0	H64A/N62H pH 7.8	H64A/N67H pH 6.0	H64A/N67H pH 7.8
Resolution (Å)	20.0 – 1.80 (1.86 – 1.80)*	20.0 – 1.90 (1.97 – 1.90)	20.0 – 1.63 (1.69 – 1.63)	20.0 – 1.80 (1.86 – 1.80)
Total Number of Unique Reflections	22162 (2132)	18130 (1813)	29130 (2583)	21547 (2070)
Completeness (%)	95.0 (91.60)	91.8 (92.9)	93.5 (83.7)	92.7 (89.0)
Redundancy	3.0 (3.0)	2.5 (2.3)	3.1 (2.9)	2.8 (2.6)
$R_{\text{symm}}^{\dagger}$	0.074 (0.395)	0.072 (0.316)	0.059 (0.329)	0.068 (0.292)
$R_{\text{cryst}}^{\ddagger} / R_{\text{work}}^{\text{§}}$	0.171/0.206	0.168/0.217	0.178/0.210	0.166/0.209
Ave B-factor (Å ²)	16/20/30	16/20/29	17/21/30	16/20/30
Main/side/solvent Number of solvent	129	137	120	132

* Data in parenthesis are for the highest resolution shell.

$$\dagger R_{\text{symm}} = \frac{\sum |I - \langle I \rangle|}{\sum \langle I \rangle}$$

$$\ddagger R_{\text{cryst}} = \frac{\sum ||F_o| - |F_c||}{\sum |F_o|}$$

§ R_{free} is calculated the same as R_{cryst} except it is for data omitted from refinement (5% of reflections for all data sets).

Table 2-3. pH-Independent rate constants for proton transfer and pK_a for proton donor and acceptors in wild type and mutant HCA II.

Enzyme	k_B (μs^{-1}) ^a	$(pK_a)_{His}$	$(pK_a)_{ZnH_2O}$	Zn-His distance
Wild Type ^b	0.8 ± 0.1	7.2 ± 0.1	6.9 ± 0.1	7.5
H64A	~ 0.02	N/a	6.9 ± 0.1	N/a
H64A/N62H	0.2 ± 0.1 ^c	5.3 ± 0.3	7.2 ± 0.1	6.6
H64A/N67H	~ 0.03 ^c	5.7 ± 0.4	7.3 ± 0.1	8.2

^a Values are from a least-squares fit of eq 6 to the data of Figures 2-3 and 2-4.

^b From Duda *et al.*, 2001

^c Values are uncertain due to the scatter of the data.

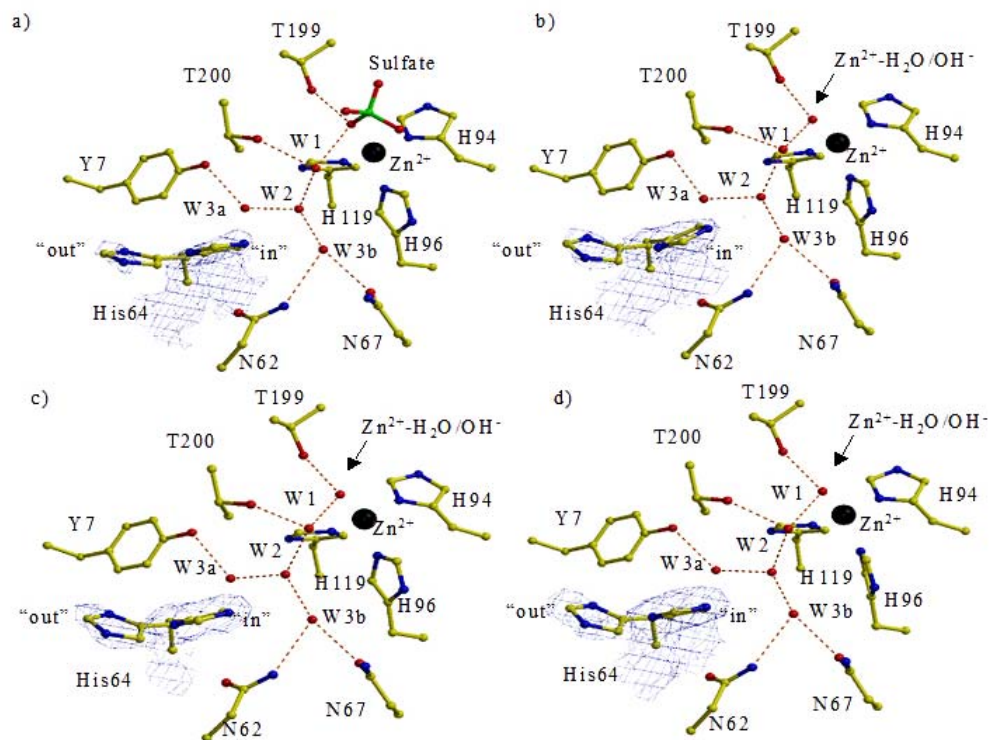


Figure 2-1. Crystal structures of wild type HCA II active site. Panels (a) through (d) are shown in the same orientation, (a) pH 5.1, (b) pH 6.1, (c) pH 7.0, and (d) pH 10.0. Active site residues are shown in yellow ball-and-stick and the zinc as a black sphere. Water molecules are as labeled and are shown as red spheres. $2F_o - F_c$ electron density maps for His64 are shown in blue and are contoured at 1.0σ . Dashed lines represent inferred hydrogen bonds based on geometry and distance between donor and acceptor atoms. Figure was generated and rendered with Bobscrip and Raster3D (Esnouf, 1997; Merritt and Bacon, 1997).

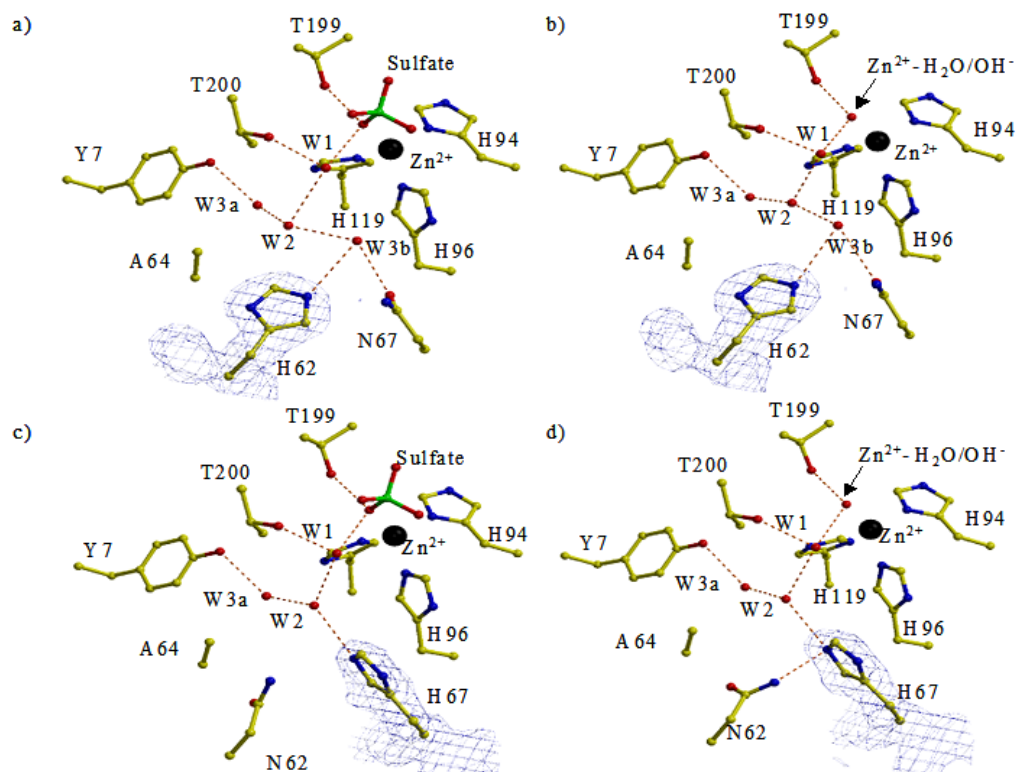


Figure 2-2. Crystal structures of mutant HCA II active site. Panels (a) through (d) are shown in the same orientation, (a) H64A/N62H pH 6.0, (b) H64A/N62H pH 7.8, (c) H64A/N67H pH 6.0, and (d) H64A/N67H pH 7.8. Active site residues are shown in yellow ball-and-stick and the zinc as a black sphere. Water molecules are as labeled and are shown as red spheres. $2F_o - F_c$ electron density maps for His62/His67 are shown in blue and are contoured at 1.0σ . Dashed lines represent inferred hydrogen bonds based on geometry and distance between donor and acceptor atoms. Figure was generated and rendered with Bobscrip and Raster3D (Esnouf, 1997; Merritt and Bacon, 1997).

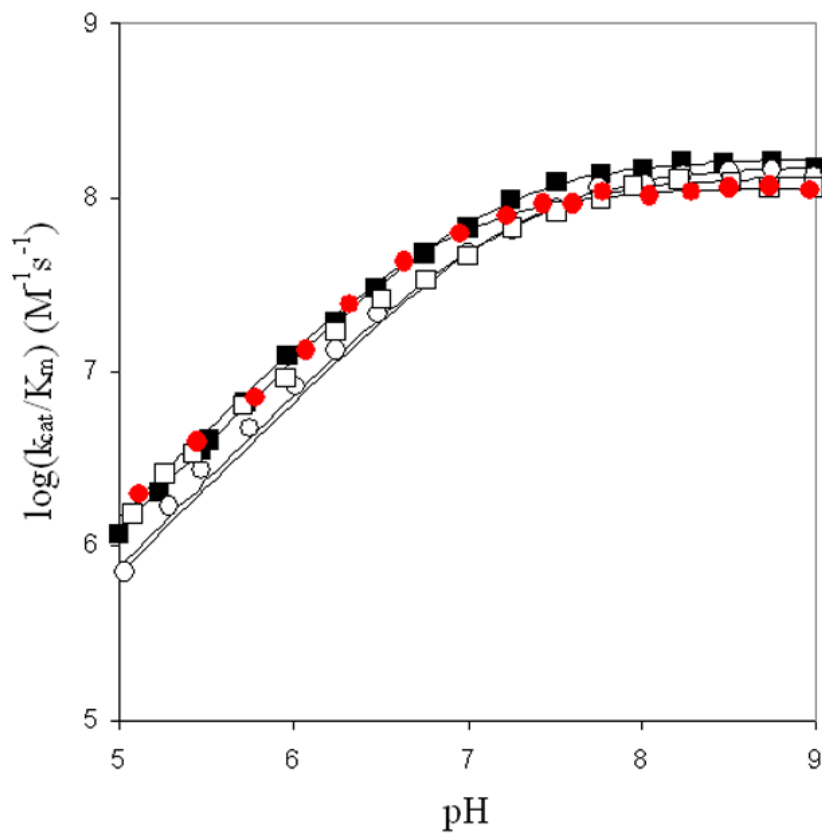


Figure 2-3. The pH profiles for k_{cat}/K_M catalyzed by wild type and mutant HCA II. (●) Wild type, (■) H64A, (○) H64A/N62H, (□) H64A/N67H. Data were obtained at 25° in the absence of exogenous buffers using a total concentration of all species of CO_2 of 25 mM, with the ionic strength maintained at 0.2 M by addition of sodium sulfate. The solid lines are fit to a single ionization (eq 5) with the pK_a given in Table 2-3.

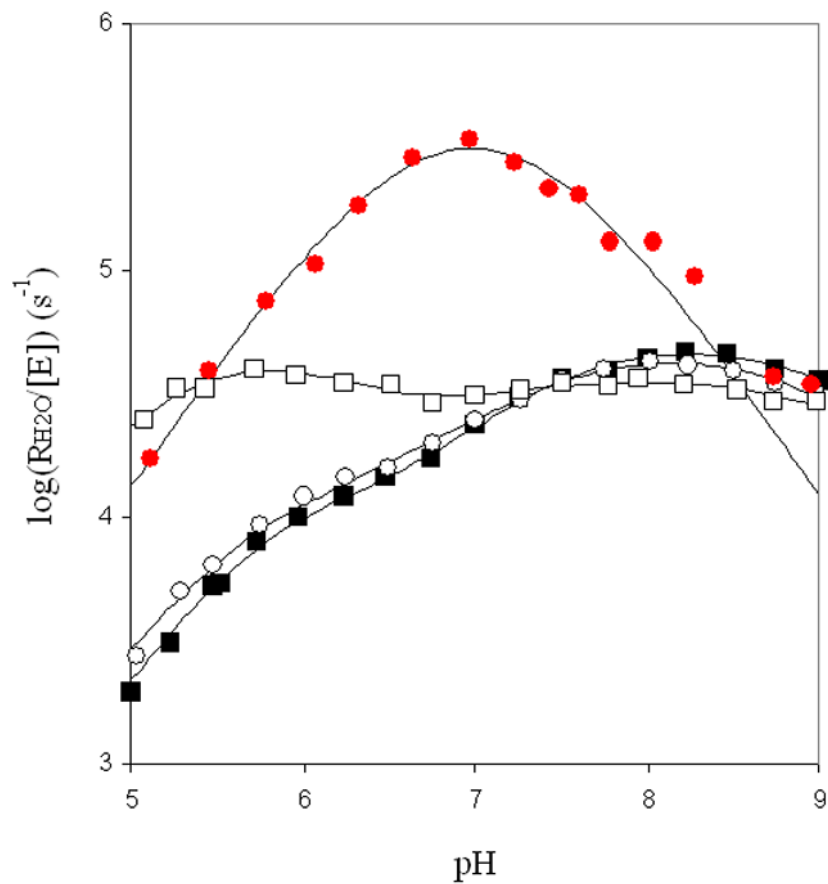


Figure 2-4. The pH profiles for $\text{RH}_2\text{O}/[\text{E}]$ catalyzed by wild type and mutant HCA II. (●) Wild type, (■) H64A, (○) H64A/N62H, (□) H64A/N67H. Data were obtained at 25° in the absence of exogenous buffers using a total concentration of all species of CO_2 of 25 mM, with the ionic strength maintained at 0.2 M by addition of sodium sulfate.

CHAPTER 3

STRUCTURAL AND KINETIC EFFECTS OF HYDROPHOBIC MUTATIONS IN THE ACTIVE SITE OF HUMAN CARBONIC ANHYDRASE II

In Chapter 2, studies of the structural and kinetic effects of moving the proton shuttle to various locations in the active site of human carbonic anhydrase II (HCA II) were presented. Kinetic and structural data over various pHs were obtained and correlated with observed changes in the active site and proton transfer rates. In Chapter 3, a different approach to studying proton transfer was undertaken and is discussed. Site-direct mutagenesis of several key active site residues were performed with the expectation that these mutations would affect proton transfer rates and the architecture of the hydrogen bonded solvent network found in the active site of HCA II.

Introduction

HCA II is the most efficient of all the HCAs with a maximal turnover rate of 10^6 s^{-1} (Khalifah, 1971). Catalytic rates of HCA II and the mechanism has been described in detail in Chapters 1 and 2. Briefly, the second part of the catalysis by HCA II involves two proton transfer steps: the first between the zinc-bound solvent and an internal proton acceptor, His64, and the second between His64 and an exogenous proton acceptor such as the bulk solvent of buffer (Silverman, 1982; Silverman and Lindskog, 1988, Tu *et al.*, 1989). The first proton transfer event involves several water molecules (W1, W2, W3a, and W3b; Figure 3-1) and this network is also described in detail in Chapter 1 (Fisher *et al.*, 2005). With the exception of W2, all other water molecules are coordinated by hydrogen bonding interactions to several key active site residues such as Tyr7, Asn62,

and Asn67. Figure 3-1 shows a view of the wild type HCA II active site with these residues and water molecules as labeled.

The proton shuttle residue, His64, is located on the edge of the active cavity, about 8 Å away from the zinc. This distance makes a direct proton transfer impossible and as a result the excess proton has to exit the active site via the conserved and ordered water molecules shown in Figure 3-1 (Steiner *et al.*, 1975; Eriksson *et al.*, 1988). In several crystal structures determined at various pHs, His64 has been shown to occupy two distinct conformations, the so-called “in” and “out” positions. However, the presence of the dual conformation is not always observed and under some conditions (such as pH or in the presence of inhibitors) it appears to be either all in the “in” or all in the “out” position (Nair and Christianson, 1991; Krebs and Fierke, 1991; Fisher *et al.*, 2005). It should be noted that at the resolution of these studies, an occupancy change of 0-10% would be impossible to observe.

To better understand the role of the conserved water network and the implications of side chain mobility of His64 for efficient proton transfer, three hydrophilic amino acids in the active site of HCA II were replaced by site-directed mutagenesis with hydrophobic residues: Y7F, N62L, and N67L. Effects of these substitutions were evaluated by measuring kinetic proton transfer rates, the conformation of His64, and the structural effects on overall active site architecture as well as the water network.

Materials and Methods

Enzymes

Plasmids with the appropriate mutations in the cDNA of HCA II were produced by site-directed mutagenesis using the Qiagen QuikChange kit. Mutagenic primers were designed and the procedures performed as per manufacturers instructions. Residue Tyr7

was mutated to a Phe, and residues Asn62 and Asn67 were separately mutated to Leu. All mutations were verified as correct by sequencing the entire coding region of the HCA II plasmid. Protein expression was performed in *E. coli* BL21(DE3) pLysS cells and the resulting enzymes were purified using affinity chromatography (Khalifah, 1977). A detailed description of these procedures can be found in the Materials and Methods section of Chapter 2. Prior to any crystallization or activity assays the purity of the protein was verified by electrophoresis on a 12% polyacrylamide gel stained with Coomassie. The concentration of HCA II was determined by measuring the absorbance at 280 nm and using a molar absorptivity of $5.4 \times 10^4 \text{ M}^{-1}\text{cm}^{-1}$ (Coleman, 1967).

Crystallography

Crystals of mutant HCA II were obtained using the hanging drop method at room temperature (McPherson, 1982). The first set of crystals of all three mutants at pH 8.2 were obtained by mixing 5 μl of protein (10-15 mg/ml concentrations in 50 mM Tris-HCl, pH 7.8) with 5 μl of the precipitant solution (50 mM Tris-HCl, pH 8.2, 2.5-2.9 M ammonium sulfate) against 1000 μl of the precipitant solution. For the N62L and N67L structures determined at pH 6.0, previously grown crystals were soaked overnight in 50 mM sodium acetate, pH 6.0, 2.6 M ammonium sulfate. For Y7F at pH 10.0, previously grown crystals were soaked overnight in 50 mM CAPS, pH 10.0, 2.6 M ammonium sulfate. Y7F crystals were also grown using a different precipitant solution that consisted of 100 mM Tris-Cl, pH 9.0, 1.3 M sodium citrate. Useful crystals under all conditions appear within 7 days of crystallization set-up.

X-ray diffraction data was collected using a R-AXIS IV++ image plate system with Osmic mirrors and a Rigaku HU-H3R Cu rotating anode operating at 50 kV and 100mA. The detector to crystal distance was set to 100 mm. Each data set was collected at room

temperature from 1-3 crystals mounted in quartz capillaries. The oscillation steps were 1° with a 7 minute exposure time. Diffraction data of the Y7F crystals grown with sodium citrate were collected at the Advanced Photon Source (APS) on beamline SER-CAT 22-ID using a wavelength of 0.979 Å. The crystal to detector distance was set at 120 mm with a 1 second exposure time per image. Images were recorded on a Mar300 CCD with 1° oscillations. X-ray data processing was performed using DENZO and scaled and reduced with SCALEPACK (Otwinowski and Minor, 1997). Structure determination and refinement was carried out with Crystallographic and NMR System (CNS) version 1.1 (Brünger *et al.*, 1998). All manual building was performed with Coot (Emsley and Cowtan, 2005). The structure of wild type HCA II (PDB accession code 1TBT) was isomorphous with all the data collected and was used to phase the data sets (Fisher *et al.*, 2005). To avoid phase bias of the model, the zinc atom, water molecules, and mutated side chains were removed. After one cycle of rigid body refinement, annealing by heating to 3000 K with gradual cooling, geometry restrained position refinement, and temperature factor refinement, the $F_o - F_c$ and $2F_o - F_c$ Fourier maps were generated. Visual inspection of these maps clearly showed the electron density for the zinc atom and the mutated side chains and these were subsequently incorporated into their respective models. After several cycles of refinement, solvent molecules were incorporated into the models using the automated water-picking program implemented in CNS until no more waters were found at the 2.0σ level. Refinement of the models continued until the R-factors converged. Tables 3-1 and 3-2 show the data set and final model statistics.

Kinetics and Activity Analysis

Determination, by membrane-inlet mass spectrometry, of R_1 and R_{H_2O} was performed using the ^{18}O exchange method by Dr. Chingkuang Tu in the lab of Dr. Silverman

(Silverman, 1982). The methodology for obtaining these rate constants was described in detail in the Materials and Methods section of Chapter 2 and will not be repeated here. Initial rates of CO₂ hydration were measured by following the change in absorbance of a pH indicator on an Applied Photophysics (SX.18MV) stopped-flow spectrophotometer and these assays were also done by Dr. Chingkuang Tu in the Silverman lab. The pK_a values and wavelengths for the pH indicator-buffer pairs used to create pH profiles were as follows: MES (pK_a = 6.1) and chlorophenol red (pK_a = 6.3), λ = 574 nm; MOPS (pK_a = 7.2) and p-nitro phenol (pK_a = 7.1), λ = 401 nm; HEPES (pK_a = 7.5) and phenol red (pK_a = 7.5), λ = 557 nm; TAPS (pK_a = 8.4) and m-cresol purple (pK_a = 8.3), λ = 578 nm; CHES (pK_a = 9.3) and thymol blue (pK_a = 8.9), λ = 596 nm. Final buffer concentrations were 50 mM, and total ionic strength was kept at 0.2 M by the addition of sodium sulfate. CO₂ solutions were prepared by bubbling CO₂ into water at 25 °C with final concentrations after mixing ranging from 0.7 – 17 mM. The mean initial rates at each pH were determined from 5 to 8 reaction traces comprising the initial 10% of the reaction. The uncatalyzed rates were determined in a similar manner and subtracted from the total observed rates. Determination of the kinetic constants k_{cat} and $k_{\text{cat}}/K_{\text{M}}$ were carried out by a nonlinear least-squares method (Enzfitter, Elsevier-Biosoft).

Results and Discussion

Structural Effects of Hydrophobic Mutations

All crystals were isomorphous and belonged to the space group P2₁ with the following mean unit cell dimensions: $a = 42.7 \pm 0.4 \text{ \AA}$, $b = 41.6 \pm 0.5 \text{ \AA}$, $c = 72.9 \pm 0.2 \text{ \AA}$, $\beta = 104.6 \pm 0.5^\circ$. The HCA II mutant data sets at pH 8.2 were processed to 1.65 – 1.70 Å resolution, while the other pH data sets were processed to 1.8 Å resolution. A summary of the data set and final model statistics is given in Tables 3-1 and 3-2.

The N62L mutant structure determined at pH 8.2 shows that the water network is conserved compared to wild type (Figure 3-1 and 3-2 (a)). However, as expected, the hydrogen bond between Leu62 and W3b is lost. The side chain of His64, which is often observed in a dual conformation in wild type structures, is completely in the “in” position. Leu62 has moved away from the solvated area in the active site and now occupies a hydrophobic region that also contains Leu60. The displacement of Leu62 removes the hydrophobic side chain away from the water network and as a result does not affect it at all.

In contrast to N62L, the N67L mutant displays a disrupted water network compared to wild type HCA II (Figure 3-1 and 3-2 (b)) and His64 appears to be all in the “out” position. Unlike the orientation of Leu62 that has been rotated away from the active site compared to an Asn at that position, Leu67 occupies a similar position to Asn67. It might be the presence of this hydrophobic residue that disrupts the water network. The differences in the His64 side chain orientations and water network should be due to electrostatic changes in the active site and not steric effects as the effective size of the side chains are similar.

In the Y7F mutant structure determined at pH 8.2, the water network appears mainly conserved. However, due to the loss of the hydroxyl group by changing Tyr7 to a Phe, the essential hydrogen bond to W3a is missing and as a result this water molecule is not observed here anymore. Phe7 occupies a similar position compared to Tyr7 as seen in wild type (Figure 3-1 and 3-3(a)). His64 in this mutant is also all in the “in” position and appears to make a very weak hydrogen bond to W2.

An unusual observation is the presence of a sulfate ion bound to the zinc atom. It has been observed that sulfate will only bind to wild type HCA II at very low pH (~ pH 5.1) and it seems that this mutation could be facilitating a higher affinity of the active site for sulfate (Fisher *et al.*, 2005).

From other structural studies of wild type HCA II it is known that the presence of sulfate does not affect the water network but it is not known if the presence of sulfate affects the orientation of His64 (Fisher *et al.*, 2005). As the Y7F structure at pH 8.2 showed a sulfate bound and His64 is only in the “in” position, the pH of the other two mutant crystals was lowered to pH 6.0 to get sulfate to bind.

These structure revealed that sulfate did bind at the lower pH and that it did not affect the orientation of His64 as His64 was still either all in the “in” (as in the case of N62L) or all in the “out” (as in the case of N67L) (Figure 3-2 (c) and (d)). The water networks in both N62L and N67L structures at pH 6.0 were completely disrupted (Figure 3-2 (c) and (d)). Leu62 at pH 6.0 had moved compared to the structure at pH 8.2 and is now pointing into the active site and might be a contributing factor in the water network disruption. The side chain of Leu67 at pH 6.0 also moved compared to its structure at pH 8.2 (Figure 3-2 (c) and (d)). Apart from repelling solvent from these areas, it is not clear if the movement of these two residues at lower pH is significant.

In an attempt to remove the sulfate in the Y7F mutant, the pH was increased to pH 10.0. Surprisingly, this structure showed that sulfate was still present even at this extreme pH. However, His64 and the water network was undisturbed and appeared the same as the structure at pH 8.2 (Figure 3-3 (a) and (b)). These observations rule out the idea that the presence of sulfate affects the orientation of His64 as it is observed that His64 can

occupy the “in” conformation in the absence or presence of sulfate (Figure 3-2, compare panels (a) and (b) with (c) and (d)). To further study this, it was necessary to see the active site of Y7F in the absence of any sulfate. To this end, a different crystallization condition using sodium citrate instead of ammonium sulfate was tried and made it possible to determine the structure of Y7F at pH 9.0 in the absence of any sulfate (Figure 3-3 (c)). Except for the lack of sulfate it can be seen that His64 and the water network appears the same as they did in the other two structures at pH 8.2 and 10.0 (Figure 3-3 (b) and (c)). The observation of different orientations of His64 can be used to comment on the relationship between this orientation and the efficiency of proton transfer. Inspection of His64 in the more efficient wild type, Y7F, and N62L HCA II this residue occupies the “in” conformation. This is in contrast with the less efficient N67L HCA II where His64 appears more in the “out” conformation. These observations alone do not provide adequate evidence that His64 in the “in” position is necessary or sufficient for fast proton transfer rates.

Kinetic Effects of Hydrophobic Mutations

The measurements of $k_{\text{cat}}/K_{\text{M}}$ for the hydration of CO_2 was obtained by both ^{18}O exchange methods at chemical equilibrium and by stopped-flow methods at steady state. As expected, these data shown in Table 3-3 indicate no significant changes between wild type and the mutants, however, the values for N67L appear a bit lower than the others in Table 3-3. This was found for both the maximal values of $k_{\text{cat}}/K_{\text{M}}$ and for the apparent pK_a near 7.0 of the zinc-bound water calculated from the pH profile of $k_{\text{cat}}/K_{\text{M}}$ (Figure 3-4). This supports the structural data that there are no substantial changes in the active site structures and implies no changes in the chemistry of catalyzed interconversion of CO_2

and bicarbonate. It is not surprising that these mutations do not affect the first part of catalysis as residues 7, 62, and 67 are more than 7 Å away from the active site zinc.

Other studies involved mutating residues closer to the zinc, such as Thr199 and Glu106, and the results show that those residues are essential for efficient interconversion of CO₂ and bicarbonate (Liang *et al.*, 1993; Krebs *et al.*, 1993). These observations support the mechanism of the first stage of catalysis which involves a direct nucleophilic attack by the zinc-bound hydroxide on CO₂, with Thr199 and Glu106 enhancing the nucleophilicity of the zinc-bound hydroxide and optimally orienting it for reaction with CO₂ (Merz, 1990).

In the second stage of catalysis long-range proton transfer occurs between the zinc-bound solvent and the bulk solution using intervening water molecules and His64 as a proton shuttle (Tu *et al.*, 1989; Lindskog, 1997). In contrast to the first stage of catalysis, as reflected by the values of k_{cat}/K_M (Figure 3-4), the mutants in this study all displayed altered proton transfer rates when compared to wild type HCA II (Figure 3-5). The effect is best seen when inspecting the pH profiles of $R_{\text{H}_2\text{O}}/[E]$, the rate constant for the release of isotopically labeled water from the enzyme to solution, which in turn depends on the rate of proton transfer (Figure 3-5).

Proton transfer by N62L HCA II is the most complicated and difficult to interpret as it displays two small bell-shaped curves and seems to have lost its pH dependence. N67L HCA II shows a similar profile to wild type HCA II, just at a lower rate. The most surprising result here is the data for Y7F HCA II as it has a rate constant for proton transfer that is appreciably larger than for wild type (Table 3-3 and Figure 3-5).

Addition of an exogenous activator of proton transfer activity, 4-methylimidazole (4-MI), does not appear to appreciably increase the rate of N62L or N67L HCA II (Figure 3-6). Wild type HCA II is activated, compared to N62L and N67L HCA II, with maximal activation occurring at around 50 mM 4-MI. Y7F HCA II is activated to a larger extent compared to wild type with the addition of 4-MI (Figure 3-6). These data implies that the active site of Y7F HCA II is more accessible to external buffers and that the removal of a hydroxyl group, by mutating Tyr7 to a Phe, thus enhancing the activation by 4-MI over that observed for wild type, N62L, and N67L HCA II.

Solvent Structure and Implications for Proton Transfer

In crystal structures of wild type HCA II, each of the side chains Tyr7, Asn62, and Asn67 appear to make hydrogen bonds with water molecules W3a and W3b (Figure 3-1; Fisher *et al.*, 2005). In fact, the side chains of Asn62 and Asn67 interact with the same water molecule, W3b. This water structure in N62L at pH 8.2 seems unaffected by the mutation as just the hydrogen bond to W3b is lost but the water is still present due to its interaction with Asn67. The reason why Leu62 does not interfere with the water is that it has moved away from the solvated active site into a more hydrophobic region also occupied by Leu60. Overall, the water structure seems conserved with that observed in wild type HCA II. However, when the pH was lowered to pH 6.0 this residue moved back into the active site and subsequently completely disrupted the solvent structure (Figure 3-2 (c)). The data for N62L, showing His64 in the “in” conformation and an intact solvent structure at pH 8.2, would suggest an unchanged proton transfer rate. Yet, probably due to electrostatic effects, the side chain of Leu62 and the water network is easily disrupted upon a change in pH and this instability of the solvent structure could account for the slower measured proton transfer rate compared to wild type HCA II.

In contrast to N62L, Leu67 in the N67L HCA II mutant extends into the active site and effectively disrupts the ordered water structure at both pH 6.0 and 8.2 (Figure 3-2 (b) and (d)). The only water molecule that is conserved is the zinc-bound solvent that could be either a hydroxide or a water molecule. The other two waters have been displaced and do not make contact with any active site residues shown here. Also, as mentioned above, His64 is observed to be always in the “out” position, regardless of the presence of sulfate bound to the zinc. Proton transfer by this mutant displays the characteristic bell-shaped pH dependency, just at a lower rate compared to wild type HCA II (Figure 3-5). Due to these observations it is likely that the typical pH dependency of proton transfer does not correlate with an ordered solvent structure in the HCA II active site.

The Y7F HCA II mutant shows the most efficient proton transfer, even when compared to wild type HCA II. At pH 8.2, 9.0, and 10.0 the solvent structure is highly conserved and His64 is always in the “in” conformation. The net effect of the loss of W3a, due to the Tyr7 to Phe mutation, produces a single-line array of water molecules that bridges the zinc-bound solvent to His64.

It has been suggested by others that a single array of waters is much more efficient than a branched system at facilitating proton transfer. Also, an unbranched hydrogen-bonded array of water can promote most efficient proton transfer by a concerted mechanism rather than a step-wise and appears to proceed through an intermediate with partial hydronium ion character (Cui and Karplus, 2003; Voth *et al.*, 1998). There are various explanations for the very fast movement of protons in solution and these include Grotthuss’s idea of so-called structural diffusion. Other structural models for the proton in solution, or hydrated proton, includes the elementary proton (H^+), hydronium ion

(H_3O^+), the Zundel, and Eigen cation models (Eigen, 1964; Marx *et al.*, 1999). The Zundel cation is a H_5O_2^+ complex where the proton is shared between two water molecules. The Eigen cation consists of a H_9O_4^+ complex where the central H_3O^+ is strongly hydrogen bonded to three H_2O molecules in a secondary hydration configuration (Eigen, 1964; Marx *et al.*, 1999). According to Eigen, weaker hydrogen bonds are formed at the periphery of the H_9O_4^+ complex and that directed breaking and formation of these bonds lead to structural diffusion of the entire complex. The diffusion of the hydrate complex is the rate-limiting step in the mobility of a proton in solution (Eigen, 1964).

Recent studies with infrared spectroscopy of acid-base proton transfer reactions suggest the existence of a fairly stable H_3O^+ intermediate structure that is coordinated in an Eigen configuration by three water molecules. Other conclusions were that the proton transfer between acid and bases occur by a sequential, Grotthus-type proton hopping mechanism that is mediated by hydrogen bonded water networks or bridges (Mohammed *et al.*, 2005).

The highly conserved core water structure as seen in wild type HCA II consists of W1, W2, W3a, and W3b (Figure 3-7, green box). It shares many structural features of an Eigen cation in that the geometry of the structure is almost planar with $\sim 120^\circ$ between W2 and the surrounding waters. Also, the hydrogen bond distances between W2 and the others is $\sim 2.8 \text{ \AA}$ for all three. Based on the structural properties of the solvent core it could be an Eigen cation with W2 representing the excess hydrated proton as a H_3O^+ . The Eigen cation is relatively stable entity and can be observed on the nano- to picosecond scale (Mohammed *et al.*, 2005). This core structure is a somewhat branched water network in that the excess proton can get access to His64 through either one of W2, W3a,

or W3b. The X-ray crystal structure represents an energy minimized, stable structure and perhaps this solvent structure kinetically traps the excess proton. It is likely that in solution during a normal catalytic cycle, these solvent structures are constantly being broken and reformed and the crystal structure just shows the most energetically stable species. In the Y7F HCA II mutant, W3a has been removed by the introduction of the hydrophobic Phe residue. This results in a linear array with only W2 having access to His64 and could also disrupt the stability of the Eigen cation as seen in wild type HCA II. This could serve as a structural explanation for why the proton transfer proceeds so much faster in this mutant compared to wild type HCA II. Even though this mutant is faster than wild type, natural selection did not choose to have a Phe at position 7 and a possible reason is that it appears to be somewhat unstable, especially at low pH (Figure 3-5). Additionally, in contrast to wild type HCA II, where the distance between W2 and His64 is too long ($\sim 3.5 \text{ \AA}$), the distance between W2 and His64 is now $\sim 3.2 \text{ \AA}$ and constitutes a weak hydrogen bond and this could contribute to the enhanced proton transfer rates.

Conclusion

To disrupt the hydrogen bonded water network in the active site of HCA II, several key catalytic amino acids, involved with coordinating these waters, were mutated to hydrophobic residues that are similar in size. Asn62 and Asn67 were mutated to Leu (N62L and N67L) and Tyr7 was mutated to a Phe (Y7F). X-ray crystal structures and rate constants for the hydration of CO_2 and proton transfer were determined for all three mutants at different pHs. The structural and kinetic data for N62L and N67L shows that the water networks were readily disrupted, especially at low pH, and both displayed considerably low proton transfer rates compared to wild type and Y7F HCA II. The most surprising result was the enhanced proton transfer rate over that of wild type observed for

Y7F HCA II. This mutant also displayed a similar water network as wild type HCA II, except for the loss of one active site water. To examine whether the presence or absence of sulfate affected the orientation of His64, structures of the mutants were determined at several different pHs. Lowering the pH for N62L and N67L HCA II caused sulfate to bind and it was determined that it had no effect on the orientation of His64. The structure of Y7F HCA II at pH 8.2 and 10.0 showed that sulfate was still bound. Subsequently, Y7F HCA II was crystallized in the absence of any ammonium sulfate and this too showed that sulfate had no effect on His64. Correlations between the structural and kinetic data suggest that a single, linear array of water bridging His64 and the zinc-bound solvent might be more efficient at proton transfer than a branched structure.

Table 3-1. Data set and final model statistics for N62L HCA II and N67L HCA II.

HCA II	N62L pH 6.0	N62L pH 8.2	N67L pH 6.0	N67L pH 8.2
Resolution (Å)	20.0 – 1.80 (1.86 – 1.80)*	20.0 – 1.70 (1.76 – 1.70)	20.0- 1.80 (1.86 – 1.80)	20.0 – 1.65 (1.71 – 1.65)
Total Number of Unique Reflections	20541 (2031)	25698 (2422)	21266 (2142)	27340 (2590)
Completeness (%)	88.2 (86.9)	91.0 (87.4)	91.7 (92.6)	93.1 (88.9)
Redundancy	4.1 (4.0)	3.2 (3.3)	3.4 (3.2)	3.1 (3.1)
$R_{\text{symm}}^{\dagger}$	0.106 (0.339)	0.085 (0.448)	0.075 (0.349)	10.8 (28.6)
$R_{\text{cryst}}^{\ddagger} / R_{\text{work}}^{\text{J}}$	0.189 / 0.226	0.179 / 0.217	0.187 / 0.224	18.6 / 20.1
Ave B-factor (Å ²) Main/side/solvent	16.8 / 20.1 / 28.7	16.1 / 19.5 / 29.6	18.6 / 22.2 / 29.5	18.2 / 21.4 / 29.6
Number of solvent	108	132	97	116

* Data in parenthesis are for the highest resolution shell.

$$\dagger R_{\text{symm}} = \frac{\sum |I - \langle I \rangle|}{\sum \langle I \rangle}$$

$$\ddagger R_{\text{cryst}} = \frac{\sum ||F_o| - |F_c||}{\sum |F_o|}$$

^J R_{free} is calculated the same as R_{cryst} except it is for data omitted from refinement (5% of reflections for all data sets).

Table 3-2. Data set and final model statistics for Y7F HCA II.

HCA II	Y7F pH 8.2	Y7F pH 10.0	Y7F (citrate) pH 9.0
Resolution (Å)	20.0 – 1.70 (1.76 – 1.70)*	20.0 – 1.80 (1.86 – 1.80)	20.0- 1.15 (1.19 – 1.15)
Total Number of Unique Reflections	25613 (2444)	20874 (1951)	85073 (8284)
Completeness (%)	92.7 (89.8)	89.4 (83.9)	99.1 (96.8)
Redundancy	3.9 (3.9)	3.1 (3.2)	4.2 (3.2)
$R_{\text{symm}}^{\dagger}$	0.060 (0.322)	0.071 (0.238)	0.079 (0.364)
$R_{\text{cryst}}^{\ddagger} / R_{\text{work}}^{\text{J}}$	0.181 / 0.199	0.179 / 0.200	0.193 / 0.184
Ave B-factor (Å ²) Main/side/solvent	16.6 / 20.1 / 29.4	15.1 / 18.5 / 28.3	10.5 / 13.5 / 23.4
Number of solvent	115	115	270

* Data in parenthesis are for the highest resolution shell.

$$\dagger R_{\text{symm}} = \frac{\sum |I - \langle I \rangle|}{\sum \langle I \rangle}$$

$$\ddagger R_{\text{cryst}} = \frac{\sum ||F_o| - |F_c||}{\sum |F_o|}$$

^J R_{free} is calculated the same as R_{cryst} except it is for data omitted from refinement (5% of reflections for all data sets).

Table 3-3. Maximal values of rate constants for hydration of CO₂, proton transfer, and pK_a of the zinc-bound water.

	k_{cat}/K_M (M ⁻¹ s ⁻¹) ^a	pK _a	R _{H2O} (μs ⁻¹)
Wild type	120	6.9 ± 0.1	0.3
Y7F	120	7.1 ± 0.1	1.0
N62L	140	7.3 ± 0.1	0.1
N67L	90	6.5 ± 0.2	0.1

^aThe standard errors for k_{cat}/K_M are 10% or less.

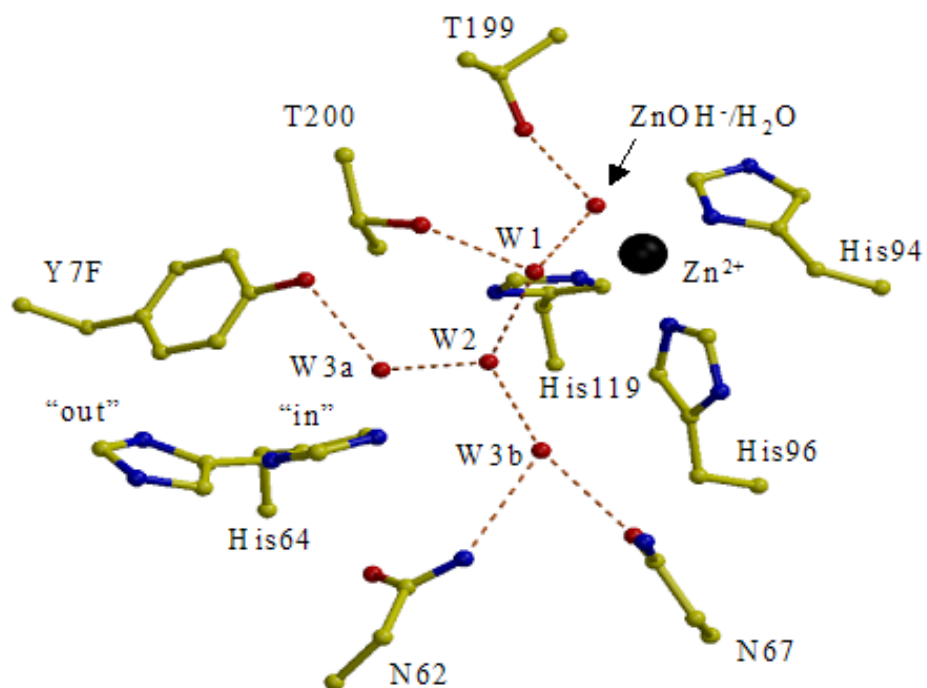


Figure 3-1. Active site of wild type human carbonic anhydrase II. The zinc atom is shown as a black sphere and active site residues are in yellow ball-and-stick and are as labeled. Water molecules are shown as red spheres and are as numbered. Figure was generated with BobScript and rendered with Raster3D (Merritt and Bacon, 1997; Esnouf, 1997).

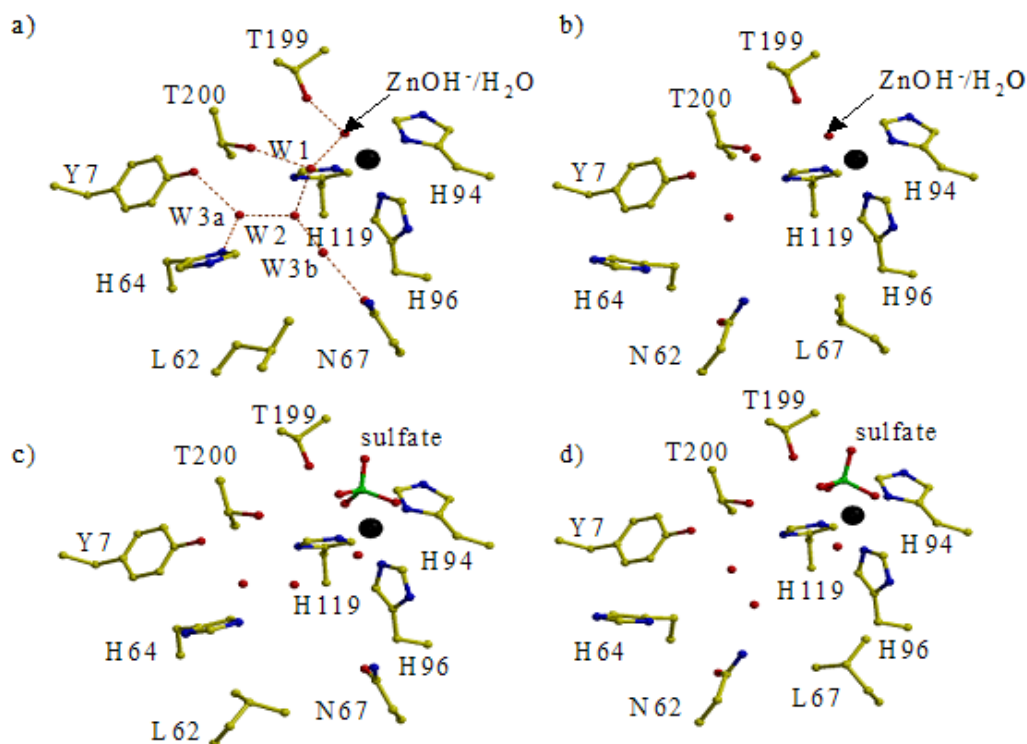


Figure 3-2. Active site of N62L and N67L at pH 8.2 and pH 6.0. (a) N62L HCA II at pH 8.2; (b) N67L HCA II at pH 8.2; (c) N62L at pH 6.0; (d) N67L HCA II at pH 6.0. Active site residues are shown in yellow ball-and-stick and are as labeled. The black sphere is the zinc atom and waters are shown as red spheres. Sulfate ions are in green ball-and-stick and are labeled. Figure was generated and rendered with BobScript and Raster3D, respectively (Esnouf, 1997; Merritt and Bacon, 1997).

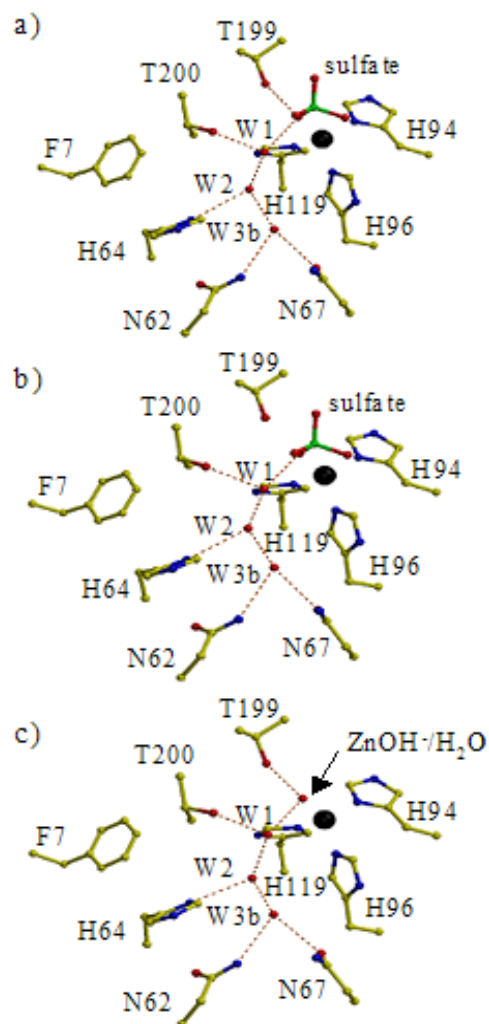


Figure 3-3. Active site of Y7F HCA II at various pH. (a) Y7F HCA II at pH 8.2; (b) Y7F HCA II at pH 10.0; (c) Y7F HCA II at pH 9.0 with no sulfate. Active site residues are shown in yellow ball-and-stick and are as labeled. The zinc atom and water molecules are shown as black and red spheres, respectively. Figure was generated with BobScript and rendered with Raster3D (Esnouf, 1997; Merritt and Bacon, 1997).

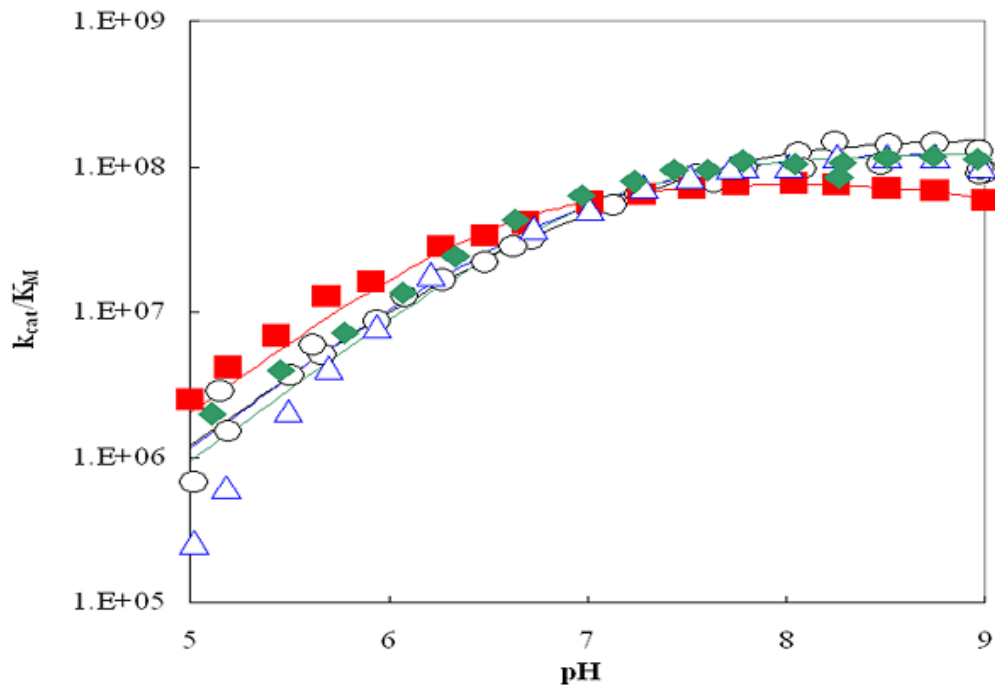


Figure 3-4. The pH profiles for k_{cat}/K_M catalyzed by wild type and mutant HCA II. (◆) Wild type, (■) N67L, (○) N62L, (△) Y7F HCA II. Data were obtained at 25° in the absence of exogenous buffers using a total concentration of all species of CO₂ of 25 mM, with the ionic strength maintained at 0.2 M by addition of sodium sulfate. The solid lines are fit to a single ionization with the pK_a given in Table 3-3.

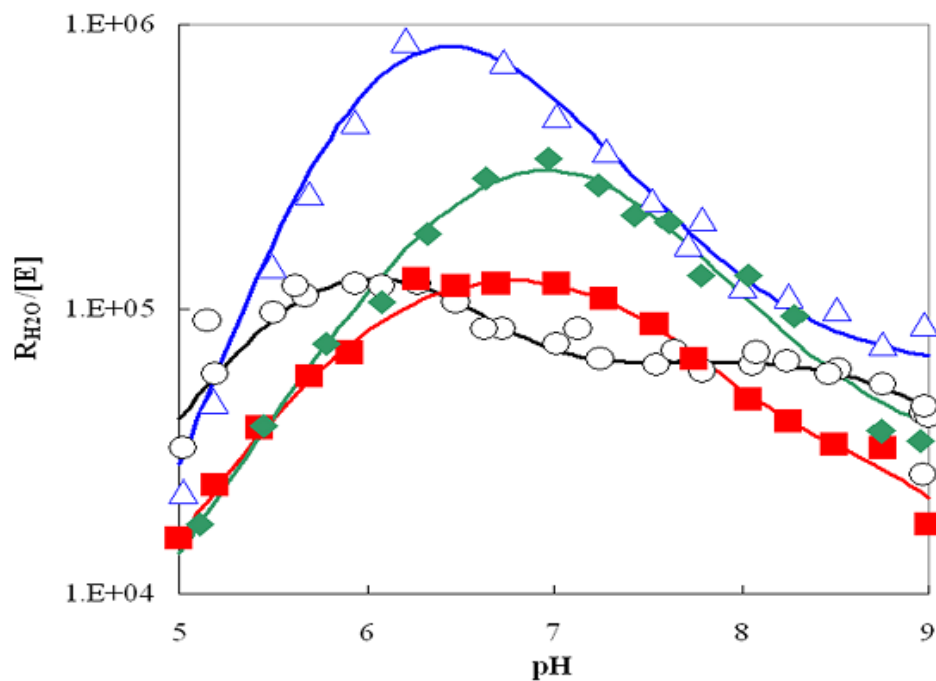


Figure 3-5. The pH profiles for $R_{H_2O}/[E]$ catalyzed by wild type and mutant HCA II. (◆) Wild type, (■) N67L, (○) N62L, (△) Y7F HCA II. Data were obtained at 25° in the absence of exogenous buffers using a total concentration of all species of CO_2 of 25 mM, with the ionic strength maintained at 0.2 M by addition of sodium sulfate.

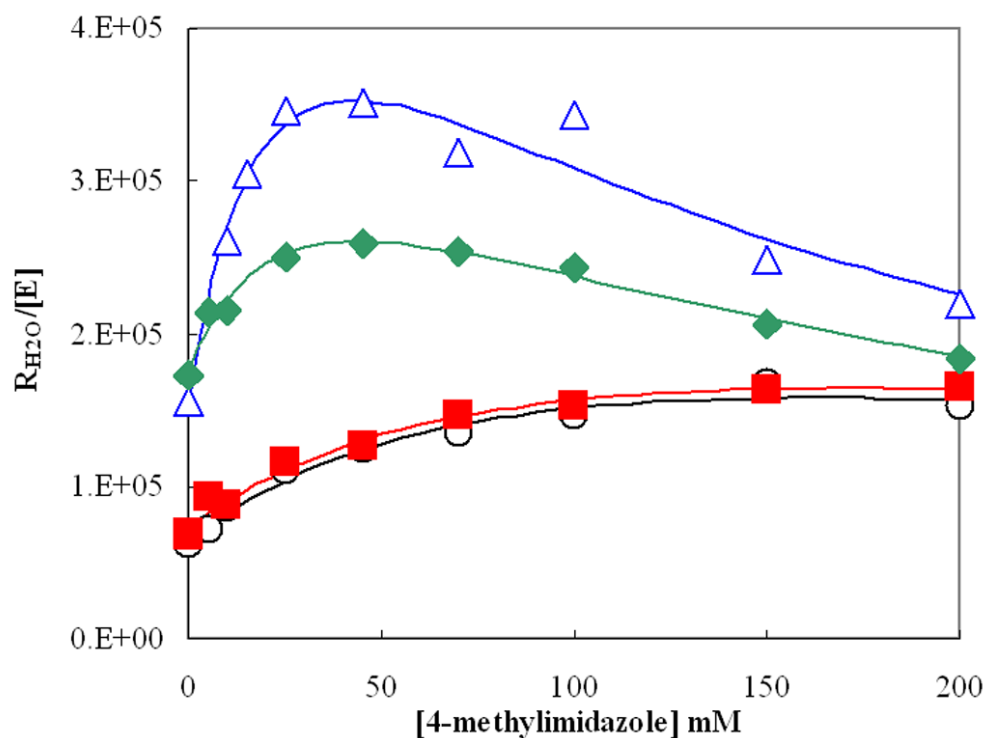


Figure 3-6. Activation of $\text{RH}_2\text{O}/[\text{E}]$ catalyzed by wild type and mutant HCA II by the addition of 4-methylimidazole. (◆) Wild type, (■) N67L, (○) N62L, (△) Y7F HCA II. Data were obtained at 25° by the ^{18}O exchange method using a total concentration of all species of CO_2 of 25 mM and adding increasing amounts of 4-methylimidazole, with the ionic strength maintained at 0.2 M by addition of sodium sulfate.

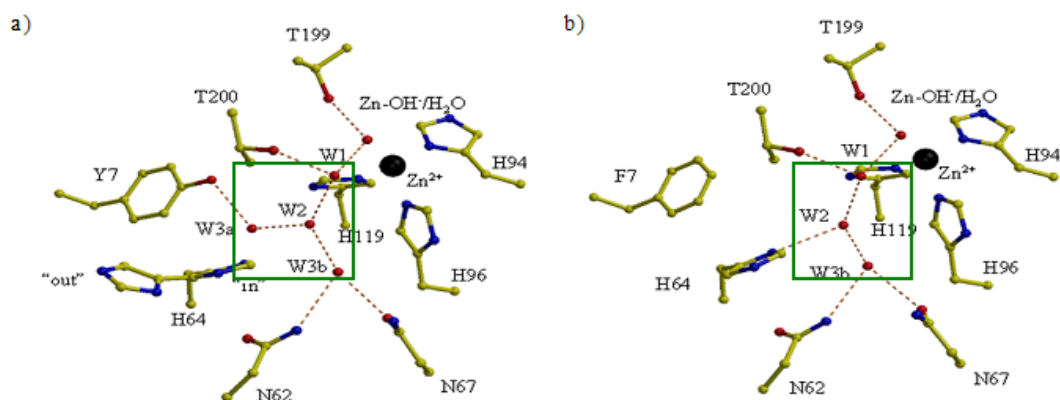


Figure 3-7. Active sites of wild type and Y7F HCA II. (a) Wild type, and (b) Y7F HCA II. Residues are shown in yellow ball-and-stick with the zinc atom as a black sphere. Water molecules and inferred hydrogen bond are shown as red spheres and dashed lines, respectively. The green boxes surround the core solvent structure in the active sites. Figure was generated with BobScript and rendered with Raster3D (Esnouf, 1997; Merritt and Bacon, 1997).

CHAPTER 4 WORKING TOWARDS A NEUTRON STRUCTURE OF PERDEUTERATED HUMAN CARBONIC ANHYDRASE II

Chapters 2 and 3 included work towards a better understanding of the proton transfer mechanism that is part of the catalysis by human carbonic anhydrase II (HCA II). The methods employed included kinetic measurements of rate constants for proton transfer as well as detailed structural studies of the active site residues and water structure. However, X-ray crystallography is not the best technique for investigating waters because hydrogen atoms, which make up about half of all the atoms in a protein, are virtually invisible to X-rays. Neutron macromolecular crystallography is currently the only direct technique for observing hydrogen H (or deuterium D) atoms and can give atomic details even at modest resolutions (~ 2.0 Å). This chapter will describe how and why neutrons are different from X-rays and will include recent progress towards obtaining a neutron structure of perdeuterated HCA II.

Introduction

Neutron crystallography can provide unique information about hydration states of proteins, ionization states of key catalytic amino acids, water molecules, and position of H atoms. H atoms are a fundamental part of many enzymatic processes, some of which involve proton transfer between residues in the protein and substrates, products, ligands, as well as mediating the binding, through water molecules, of pharmacological agents (Langan *et al.*, 2004).

Assigning positions of hydrogen atoms is possible in X-ray crystallography if atomic or sub-atomic resolution data can be collected ($\leq 1.2 \text{ \AA}$). Even in the case of high resolution X-ray diffraction it is often still hard or impossible to confidently assign the positions of hydrogen H atoms associated with water molecules. H atoms that are associated with well-ordered parts of the protein (such as the main or side chains) can be assigned, but H atoms in disordered regions or part of water molecules are much harder to assign (Coates *et al.*, 2001; Habash *et al.*, 2000).

The extent of diffraction by X-rays depends on the number of electrons. As H and D have only 1 electron, they diffract X-rays very poorly compared to more electron-rich atoms such as carbon C, nitrogen N, oxygen O, and sulfur S. The scattering amplitude of atoms by X-rays increase linearly with increasing numbers of electrons (Table 4-1). This is in contrast to how atoms behave in a neutron beam as each atom has a unique scattering amplitude that is a property of the nucleus and has to be determined experimentally (Table 4-1).

H and/or D atoms are more easily located by neutron analysis as the scattering lengths of H ($-3.7 \times 10^{-15} \text{ m}$, or -3.7 fm) is equal in magnitude but opposite in sign when compared to other atoms found in proteins. D atoms have a scattering length (6.7 fm) that is very close to the range of O (5.8 fm), N (9.4 fm), C (6.6 fm) and S (3.1 fm) making it easier to locate by this method (Coates *et al.*, 2001). The real strength of using neutrons over X-rays are the different scattering properties of H and D atoms. The negative scattering amplitude of H with neutrons can potentially be exploited to observe them by just looking at negative nuclear density. This kind of contrast labeling has been successfully used to determine levels of H/D exchange and using the data for further

elucidation of the mechanism or activity of enzymes (Habash *et al.*, 1997). A classic example is the study of a carbon monoxide myoglobin derivative that was subject to H/D exchange prior to neutron diffraction. The results gave information on the hydration shells around the protein as well as region in the heme binding site that did not exchange (Norvell *et al.*, 1975). However, there are two problems with having H in proteins crystals for diffraction experiments. The first is the low coherent scattering cross section of H atoms and the second is the large incoherent scattering cross section that leads to a very large undesirable background (Table 4-1).

The heavy isotope of H, deuterium D, behaves the same with X-rays but have very different properties with neutrons. D atoms have a scattering amplitude similar to the other atoms found in proteins and also a small incoherent scattering cross section (Table 4-1). For these reasons, it is often most favorable to replace as many H atoms with D atoms as is practical by either H/D exchange methods, such as soaking crystals in deuterated solutions, or by producing deuterated materials. As the H/D exchange process does not lead to fully deuterated (perdeuterated) materials, most often it is better to synthesize or purchase perdeuterated materials. Perdeuteration, as opposed to just soaking crystals in deuterated solutions, and subsequent neutron diffraction data collection vastly improves location of D atoms because, as mentioned above, D and O have similar scattering lengths and both are positive in sign. The resulting nuclear density indicates the orientation of D₂O and thus allows the location of the two D atoms (Coates *et al.*, 2001; Habash *et al.*, 2000; Myles *et al.*, 1998). In the case of H atoms in water molecules the negative density from the H can smear out or cancel the positive scattering contribution from the O atoms (Habash *et al.*, 2000). Another bonus to using perdeuterated materials

are estimates that, due to the small incoherent scattering cross section of D atoms, one can achieve at least a 40-fold reduction in the background compared to having any H atoms around. Also, having perdeuterated materials cuts back on the need for very large crystals and it is now possible to collect data from crystals that are only 0.15 mm³, as in the case of aldose reductase (Niimura *et al.*, 2005).

Neutron macromolecular crystallography is a powerful technique that complements high resolution X-ray crystallography well as a combination of the two techniques allows analysis of key hydrogen atom positions and solvent structure (Myles *et al.*, 1998).

Before collecting neutron diffraction data, crystals are usually subjected to H/D exchange by soaking the crystals in deuterated solutions. Some of the advantages to this procedure include the fact that very high incoherent background scattering from hydrogen is eliminated and that it is a lot cheaper than purchasing deuterated materials. Soaking also allows the exchange of solvent accessible hydroxyl and amide groups as well as replacing H₂O with D₂O and this information can be used assess solvent accessibility, flexibility or disorder of a protein (Niimura *et al.*, 2005).

The major drawback of neutron diffraction is the low flux of neutrons available for sample irradiation. The diffraction intensity can be calculated from eq 4-1:

$$I = (I_0 \times F^2 \times V \times A) / (v_0)^2 \quad (4-1)$$

In eq 4-1, I is the diffraction intensity, I₀ incident neutron intensity, F² structure factor, V volume of the crystal, A detector area covered by sample, and v₀ is the volume of the unit cell (Niimura, 1999). This means that the diffraction intensity strongly depends on the size of the crystal, intensity of the incident neutron beam, and the area detector. Recent advances in area detector technology, data collection, and processing

strategies in neutron protein crystallography allow studies of larger biological molecules and smaller crystals than previously thought possible. The biggest challenge is to grow a very large, single crystal ($\sim 1 \text{ mm}^3$) with a small unit cell volume (Niimura, 1999). A data collection strategy that is used to optimize the number of neutrons available, is Laue diffractometry where a range of wavelengths are used. This is in contrast to a monochromatized beam, as used in most X-ray diffraction experiments, where most of the useful neutrons are removed and only a single wavelength is used. Due to the low flux of the beam, this is a wasteful methodology and Laue diffraction allows the user to simultaneously measure diffraction in different directions from different lattice planes. Laue methods allow for a more efficient survey of reciprocal space with fewer crystal settings, and along with large area detectors effectively increases the flux on the sample (Myles *et al.*, 1998; Schultz *et al.*, 2005).

The single biggest advance in neutron protein crystallography, has been the design of better area detectors. Neutron imaging plate (NIP) technology has been developed in which a neutron converter, such as ^6Li or Gd, is mixed with photostimulated luminescence materials that are layered on a flexible plastic backing. The dynamic range, spatial resolution, and flexibility make the NIP suitable for detecting diffracted neutrons. NIPs are available in different sizes (200 mm x 200 mm and 200 mm x 400 mm) and these can be arranged side-by-side to make a combined detector of any desired size (Niimura, 1999). The neutron-sensitive image plate in use at the Institut Laue-Langevin (European Molecular Biology Laboratories, Grenoble) consists of 4 large Gd-doped phosphor plates that are packed together to give an active area of 400 x 800 mm (Myles, 1998). Image plates have high counting rates and good dynamic range, but they cannot

relay real-time information and do not have timing characteristics to determine a neutron's wavelength.

This is crucial for spallation sources where a spectrum of neutron wavelengths are used and time-of-flight is determined in order to resolve which neutrons gave rise to which reflections. For these applications, an advanced cylindrical detector was built by Brookhaven National Laboratory and is in use at the Protein Crystallography Station at Los Alamos Neutron Science Center (LANSCE). It has a height of 200 mm and a curved horizontal dimension that subtends 120° at the sample position. This detector is filled with ^3He that decay into a charged pairs upon neutron absorption. This induced charge is detected by a two-dimensional multiwire array and is used to determine the x and y position of each event (Langan *et al.*, 2004). Figure 4-1 shows a photograph of the detector in use at LANSCE.

There are very few examples in the literature of neutron protein structures and these include lysozyme, endothiasepsin, xylose isomerase, and aldose reductase. For all these projects, the investigators were unable to obtain pertinent structural information about catalysis using ultra-high resolution X-ray structure alone. Using neutron diffraction, the functionally important H atoms were identified and led to elucidation of enzyme mechanism (Langan *et al.*, 2004). However, all of these neutron structures were determined from protein crystals that were subject to H/D exchange. The only perdeuterated neutron structure so far is of myoglobin and was reported in recent years (Shu *et al.*, 2000; Niimura *et al.*, 2005).

As discussed in Chapter 1-3, the rate-limiting step in catalysis of HCA II is the intermolecular transfer of a proton from the zinc-bound solvent ($\text{H}_2\text{O}/\text{OH}^-$) to the proton

shuttling residue, His64. This distance ($\sim 7.5 \text{ \AA}$) is spanned by well-defined solvent molecules that are connected to each other and several critical side chains via a hydrogen-bonded network (Christianson and Fierke, 1996; Lindskog, 1997). Despite the availability of high-resolution crystal structures of HCA II to 1.05 \AA , there is currently no definitive information available on the absolute positions and orientations of H atoms from either the solvent network or the ionization state of active site residues (Duda *et al.*, 2003). As mentioned above, it is very hard to directly observe H atoms even in high-resolution X-ray crystal structures and neutron diffraction studies of perdeuterated crystals can be a powerful complementary technique to elucidate proton donors/acceptors and ionization states in macromolecules. Key questions that need to be answered include which solvent molecules are H_2O or OH^- molecules and which residues are proton donors or acceptors. Another controversial topic is the nature of the zinc-bound solvent in terms of whether it is a OH^- or H_2O in the crystal structure. Even in sub-atomic resolution structures of HCA II there have been no conclusive answers to any of these questions.

Despite all the advantages to neutron protein crystallography, there are very few neutron studies compared to X-ray. The main reasons are that there are few sources around the world and the available neutron beams have low flux, compared to synchrotron sources for X-rays. There is also no foreseeable way to increase the flux of neutrons from nuclear reactors due to the inherent limitations of the fission reaction that produces them. In contrast to reactor sources, spallation sources produce neutrons by the bombardment of a heavy metal target, such as mercury or tungsten, with pulsed high-energy protons. The main advantage, besides the higher flux attained, is that the neutrons produced in this way have a time-of-flight component so that fast or high energy neutrons

arrive at the detector before the slower or low energy neutrons. This allows the energy and wavelength of each neutron to be calculated and this information can be applied to the structure determination and make the process more efficient.

Structure and catalytic activity analysis and comparison of perdeuterated HCA II with hydrogenated HCA II shows that these structures are highly isomorphous and active, especially with regards to the active site architecture and the solvent network, and this indicates that using perdeuterated HCA II is appropriate for neutron macromolecular crystallography. This work lays the foundation for planned future neutron structure determination and structural analysis.

Materials and Methods

Production and Crystallization of Perdeuterated HCA II

Transformed *Escherichia coli* (*E. coli*) BL21 pLysS(DE3) cells were plated out on Luria broth agar plates supplemented with 1mM ampicillin. The plates were incubated overnight at 37 °C. The next day, an appropriate colony was selected and placed into 15 mL Spectra 9-d deuterated minimal media supplemented with 1mM ampicillin made in D₂O. This initial culture was grown for 24 hours and then the entire 15 mL was used to inoculate 150 mL Spectra 9-d minimal media supplemented with 1 mM ampicillin made in D₂O. After 18 hours, the cells were harvested by centrifugation and the resulting pellets were resuspended in 5 mL of Spectra 9-d media. The cells were then placed in 800 mL of fresh Spectra 9-d media supplemented with 1 mM ampicillin in D₂O. The large scale culture was then grown for 2-3 hours and protein expression was induced by the addition of 0.6 mM isopropyl- β -D-1-thiogalactopyranoside in D₂O and incubated for 6 hours at 37 °C while shaking at 220 rpm. Cells were harvested by centrifugation and stored at -20 °C. Upon freeze/thawing, the cell lysates were processed and the protein

purified as previously described (Khalifah *et al.*, 1977). After purification, the protein was rapidly back-exchanged into deuterated buffers and concentrated. Purity of perdeuterated HCA II was determined by SDS-PAGE.

The deuteration level of the protein sample was determined by time-of-flight electrospray mass spectrometry. The software *Isotopic Pattern Calculator v.1.6.5* for Macintosh (<http://www.shef.ac.uk/chemistry/chemputer/isotopes.html>) was used to calculate the theoretical isotopic distribution and the pattern was then matched to the experimental spectrum.

Crystals of perdeuterated HCA II were obtained by the hanging drop vapor diffusion method at room temperature (McPherson, 1982). Crystallization drops were prepared by mixing 5 μ L of concentrated protein solution (10-15 mg/mL) with 5 μ L precipitant solution consisting of 2.6 M ammonium sulfate, 50 mM Tris-Dl (pD 8.0) made in D₂O. Useful crystals appeared within 7 days of crystallization set-up.

Crystallography

Crystals were cryoprotected prior to data collection by quick-dipping them in 30% glycerol in mother liquor. The crystals were then quick frozen to 100 K in a N₂-gas stream on the beamline. Synchrotron diffraction data were collected at the ESRF beamline ID29. Several crystals were used during data collection and the crystal to detector distance was set at 105, 125, and 185 mm. X-ray data processing was performed using DENZO and scaled and reduced with SCALEPACK (Otwinowski and Minor, 1997). Several data sets were collected and three were ultimately processed and scaled together from 20.0 – 1.5 Å for a total of 220 degrees of data. All manual model building was done with Coot and model refinement was carried out using CNS version 1.1 (Emsley and Cowtan, 2004; Brünger *et al.*, 1998). The wild type structure of HCA II

(PDB accession code 1TBT; Fisher *et al.*, 2005) was isomorphous with the perdeuterated HCA II data and was subsequently used to phase the experimental data. In order to avoid phase bias of the model, the zinc atom and water molecules were removed from the phasing model. After one cycle of rigid body refinement, annealing by heating to 3000 K with gradual cooling, geometry-restrained position, and individual temperature factor refinement, F_o-F_c and $2F_o-F_c$ electron density maps were generated. These maps clearly showed the position of the zinc atom which was then included in the model and subsequent refinements. After several further cycles of refinement, water molecules were incorporated into the model using the automated water picking program, as implemented in CNS 1.1, until no more waters were found at the 2.0 σ level (Brünger *et al.*, 1998). Manual model building in Coot and refinement continued until convergence of R_{free} and R_{work} was reached (Emsley and Cowtan, 2004). Table 4-2 contains the data collection and model refinement statistics.

Activity Analysis by ^{18}O Exchange Methods

The rate constants for the hydration and proton transfer reactions were determined by Dr. CK Tu in the Silverman lab using ^{18}O exchange methods. All assays were performed as detailed in Chapter 2 except it was all done under deuterated conditions. Hydrogenated and perdeuterated HCA II were exchanged into D_2O and incubated for 3 hours prior to the assays.

Results and Discussion

Despite a small lag in cell growth, the transformed cells adapted readily to deuterated minimal media conditions and overexpression of HCA II with a yield of 30 mg/mL pure protein per liter of cells was achieved. Mass spectrometry of the purified perdeuterated HCA II showed that over 98% deuteration was obtained. By varying the

protein to precipitant ratio, optimal conditions for growing large (0.2 x 0.2 x 1.0 mm) perdeuterated crystals within a week were determined (Figure 4-2).

Structural Effects of Perdeuteration

The perdeuterated HCA II crystals diffracted to 1.5 Å and belonged to the monoclinic space group P2₁, with unit cell parameters: $a = 42.1$, $b = 41.0$, $c = 72.0$ Å, $\beta = 104.4^\circ$. The scaling R_{merge} was 0.090 and isomorphous with hydrogenated wild type HCA II crystals (Fisher *et al.*, 2005). All data collection and refinement statistics are given in Table 4-2. The final R_{cryst} and R_{free} to 1.5 Å resolution were 19.5 and 20.6 %, respectively. The model was of good quality with root mean square deviations (rmsd) for bond lengths and angles of 0.005 Å and 1.4°, respectively.

All final model statistics are given in Table 4-2. A superposition of hydrogenated HCA II (PDB accession code 1TBT; Fisher *et al.*, 2005) onto the structure of perdeuterated HCA II gave a rmsd of only 0.2 Å for all C α atoms (Figure 4-3).

Visual inspection of the backbone representations for hydrogenated and perdeuterated HCA II clearly shows that there is no appreciable difference between the two and this shows that deuteration has minimal effect on overall fold and three dimensional structure of HCA II (Figure 4-3).

When only the active site residues (Tyr7, Asn62, Asn67, His64, His94, His96, His119, Thr199, and Thr200) and solvent molecules (Zn-H₂O/OH⁻, W1, W2, W3a, and W3b) are superposed, the rmsd decreases to less than 0.1 Å. See Figure 4-4 (a) and (b) for a visual comparison of the active site architecture. The relative positions and distances between the solvent molecules and the active site residues that coordinate them are very similar, within experimental error, and are shown in Table 4-3 and Figure 4-4.

It is well-known and described in the literature that perdeuteration of proteins can have subtle effects on the physical, chemical and functional properties of proteins. A comparative study with perdeuterated cytochrome P450cam in terms of structural stability and dynamics showed that enzyme catalysis was unaffected but that the perdeuterated protein had a midpoint transition temperature that was 4 °C lower than its hydrogenated counterpart (Brockwell *et al.*, 2001; Meilleur *et al.*, 2004). However, apart from the thermal stability differences, there were no structural or kinetic differences and these results imply that the perdeuterated enzyme is a good representation of the native hydrogenated protein (Meilleur *et al.*, 2004).

Similarly, for HCA II, there appears to be no difference in the overall structure, but more importantly, the active site architecture is conserved, even down to the solvent structure which is of great importance.

Two neutron studies using quasi-Laue diffraction and H/D exchanged crystals successfully located H/D atoms at medium resolution (around 2 Å). Using these methods it is possible to gain more information from medium resolution neutron diffraction than is possible with ultra-high resolution X-ray data alone. In one study, the structure of D₂O soaked concanavalinA solved with neutron methods showed the location of 62 D₂O molecules. Furthermore, it was possible to assign both D atoms for all 62 D₂O molecules. This is a significant improvement to the 12 H₂O molecules that were assigned using the 0.95 Å X-ray data (Habash *et al.*, 2000).

In another study of endothiapepsin at 1.95 Å resolution using neutron diffraction methods, it was possible to elucidate the essential catalytic hydrogen atoms of the

aspartate residues responsible for protease activity. These hydrogen atoms were unobservable using 1.0 Å X-ray diffraction data analysis alone (Coates *et al.*, 2001).

As growing a large protein crystal is often the most challenging aspect of a neutron diffraction experiment, the large size (0.2 x 0.2 x 1.0 mm) and diffraction quality (1.5 Å with X-rays) of the perdeuterated HCA II crystals are the first step towards obtaining a neutron structure. The conservation of the key active site solvent molecules, as shown in Figure 4-4 (b), is also encouraging, as accurate assignment of the associated H/D atoms is important for an meaningful interpretation.

Kinetic Effects of Perdeuteration

Activity assays with perdeuterated and hydrogenated HCA II, soaked in D₂O for 3 hours prior to the assays, using the ¹⁸O exchange method under deuterated conditions did not show any difference in rate constants for the hydration/dehydration reaction (Figure 4-5). This result was to be expected as the nucleophilic attack by the zinc-OH⁻ on the incoming CO₂ does not involve any proton transfer and this step should not be affected by the presence of D atoms. Figure 4-5 shows the pH profile of the k_{cat}/K_M for the hydration of CO₂ catalyzed by hydrogenated and perdeuterated HCA II.

As far as proton transfer is concerned, a difference between the two enzyme species was not predicted or expected. The active site of HCA II is highly hydrated and solvent accessible and, in theory, the amino- and carboxyl groups of residues should be able to rapidly exchange their H atoms for D atoms. Similarly, the solvent molecules should easily exchange for D₂O.

The expectation was that due to the rapid exchange, the hydrogenated HCA II soaked in D₂O prior to the assays, should not display different kinetics compared to the perdeuterated enzyme. However, as shown in Figure 4-6, the pH profile for $R_{H_2O}/[E]$

clearly shows a difference between the two, with the perdeuterated HCA II catalyzing the proton transfer reaction at a lower rate compared to the hydrogenated, D₂O soaked HCA II. These kinetic isotope effects suggest that the non-exchangeable H atoms are affecting the proton transfer reaction. The effect might be an additive effect over the entire structure instead of specific key residues that mediate either catalysis or the coordinating of active site solvent molecules.

Overall, there are no appreciable kinetics effects of perdeuteration on the hydration/dehydration reaction catalyzed by HCA II (Figure 4-5). In addition, the effects on proton transfer are minor with regards to the magnitude, since the overall bell-shape and pH dependency has not been compromised (Figure 4-6). The activity data, along with the structural data, supports the idea that perdeuteration has a very subtle and slight effect, if any, on the structure and catalysis of HCA II.

Conclusion

Neutron protein crystallography is a powerful tool for studying perdeuterated protein crystals for the direct determination of key solvent molecules and H/D atoms. As a first step toward obtaining a neutron structure, perdeuterated HCA II was produced and analyzed. Known crystallization conditions were adapted to the deuterated system and the a high-quality X-ray crystal structure to 1.5 Å resolution was determined. These data showed that the overall structure and fold of perdeuterated HCA II was virtually identical to its hydrogenated counterpart. More importantly, the active site residues and key solvent molecules were completely conserved and this model will serve as the starting point for planned neutron studies. Measurement of catalysis by perdeuterated HCA II showed that the hydration/dehydration reaction was unaffected and the proton transfer displayed a minor isotope effect. This work shows the proof-of-principle that

perdeuterated HCA II is a good and accurate representation of hydrogenated HCA II and serves as a comparable entity for studies of hydrogenated HCA II.

Initial neutron diffraction tests are underway at the Protein Crystallography Station of the Los Alamos Neutron Science Center. Low resolution diffraction was observed and suggests that larger crystals are required for more data acquisition. However, with the new high-intensity Spallation Neutron Source at Oak Ridge National Laboratory nearing completion, the construction of the Macromolecular Neutron Diffractometer (MaNDi) should facilitate faster data collection times from smaller crystals.

Table 4-1. Scattering amplitudes and cross sections of atoms by X-rays and neutrons.

Atom type	X-rays (fm) ^a	Neutrons (fm) ^a	Neutrons ρ^{coh} (barns) ^b	Neutrons ρ^{incoh} (barns) ^b
Hydrogen	1	-3.8	1.8	82.0
Deuterium	1	6.5	5.4	7.6
Carbon	6	6.6	5.5	5.5
Nitrogen	7	9.4	11	11.4
Oxygen	8	5.8	4.2	4.4
Sulfur	16	3.1	1.2	1.2
Iron	26	9.6	11.4	11.8

^a fm = 1×10^{-15} m

^b barn = 1×10^{-24} cm²

Table 4-2. Data collection and model refinement statistics.

Data Collection Statistics	Perdeuterated HCA II
Molecular Weight (Da)	30664
Temperature (K)	100
Wavelength	1.005
Resolution (Å)	20.0 - 1.50 (1.55 - 1.50)*
No. unique reflections	37372 (3689)
Completeness (%)	97.0 (96.8)
Redundancy	3.0 (2.3)
R_{sym}^{\dagger}	0.09 (0.17)
Refinement Statistics	
No. protein atoms / Solvent atoms	2058 / 222
$R_{\text{free}} / R_{\text{work}}^{\ddagger}$	0.195 / 0.206
Rmsd bond lengths (Å) / angles (°)	0.005 / 1.396
Average B-factors (Å ²)	
Main / Side / Solvent / Zinc atom	10.5 / 12.9 / 23.3 / 4.9
Ramachandran Statistics	
Most favored (%)	87.6
Additional & Generously Allowed (%)	12.4

*Data in parenthesis is for the highest resolution shell.

$$\dagger R_{\text{sym}} = \frac{\sum |I - \langle I \rangle|}{\sum I}$$

$$\ddagger R_{\text{free}} = \frac{\sum |F_{\text{obs}}| - k \sum |F_{\text{calc}}|}{\sum |F_{\text{obs}}|}$$

Table 4-3. Distances between solvent molecules and active site residues for hydrogenated and perdeuterated HCA II.

Residues and Solvent Molecules	Hydrogenated (Å)	Perdeuterated (Å)
Zn ²⁺ - ZnH ₂ O/OH ⁻ (D ₂ O/OD ⁻)	2.0	1.9
ZnH ₂ O/OH ⁻ (D ₂ O/OD ⁻) - W1	2.6	2.8
W1 - W2	2.8	2.8
W2 - W3a	2.7	2.8
W2 - W3b	2.9	2.8
ZnH ₂ O/OH ⁻ (D ₂ O/OD ⁻) - T199	2.7	2.6
W1 - T200	2.7	2.7
W3a - Y7	2.7	2.7
W3b - N62	2.7	2.6
W3b - N67	3.2	3.0



Figure 4-1. The LANSCE position-sensitive ^3He -filled detector.

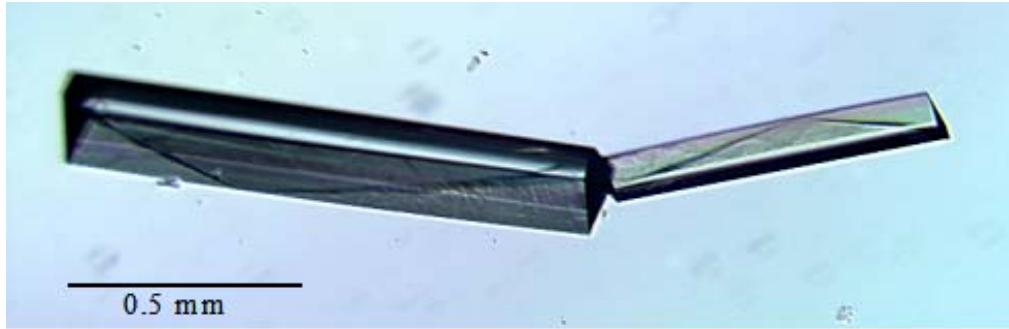


Figure 4-2. Optical photograph of perdeuterated wild type HCA II.

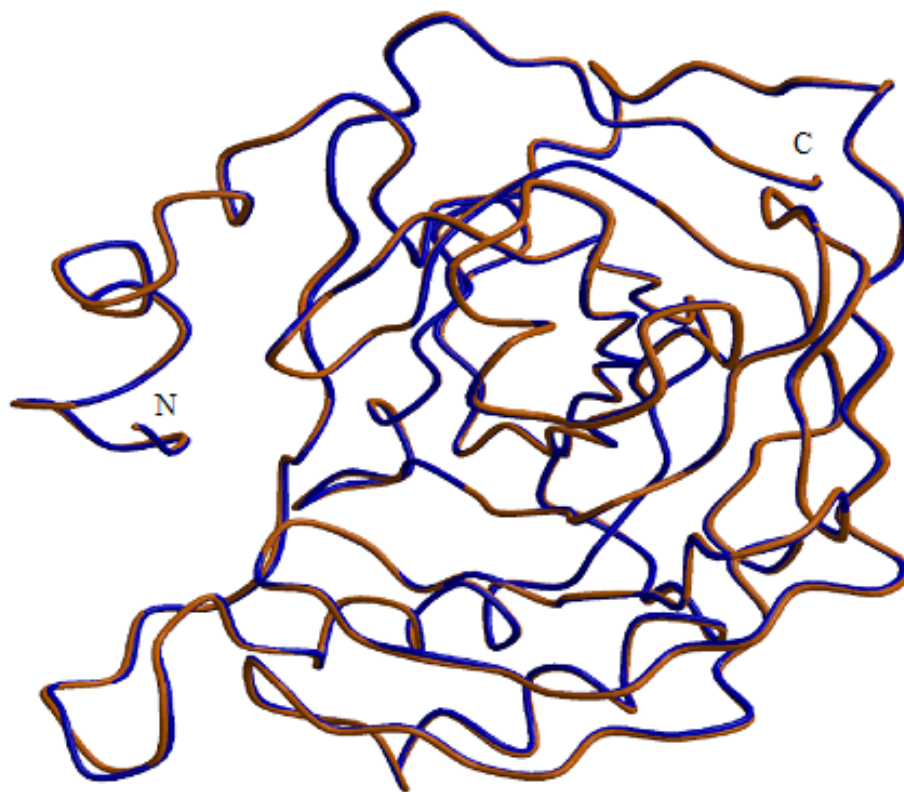


Figure 4-3. Backbone superposition of hydrogenated and perdeuterated wild type HCA II. The orange and blue coils represent the hydrogenated and perdeuterated HCA II, respectively. N and C termini are as indicated. Figure was generated with BobScript and rendered with Raster3D (Merritt and Bacon, 1997; Esnouf, 1997).

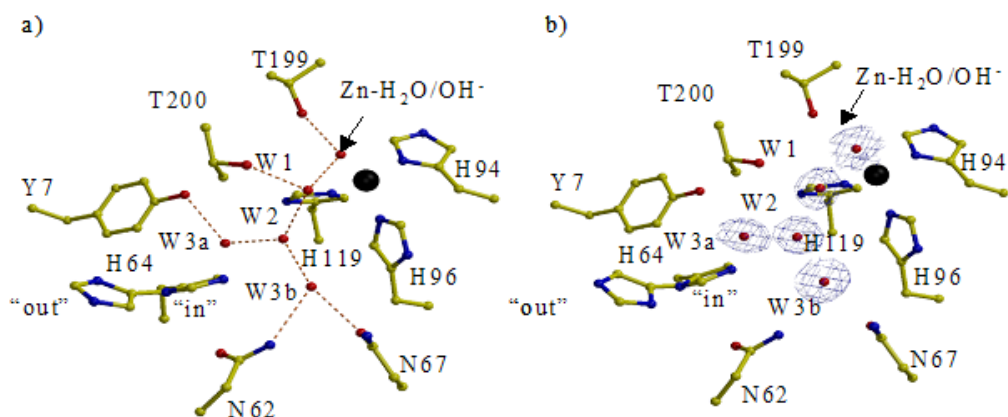


Figure 4-4. Active site comparison of hydrogenated and perdeuterated wild type HCA II. (a) Hydrogenated HCA II, (b) Perdeuterated HCA II. Active site residues are shown in yellow ball-and-stick with the catalytic zinc atom as a black sphere. Solvent molecules are shown as red spheres and inferred hydrogen bonds are orange dashed lines. Blue $2F_o - F_c$ electron density is shown only for active site waters and it contoured at 1.5σ . Figure was generated with Bobscript and rendered with Raster3D (Merritt and Bacon, 1997; Esnouf, 1997).

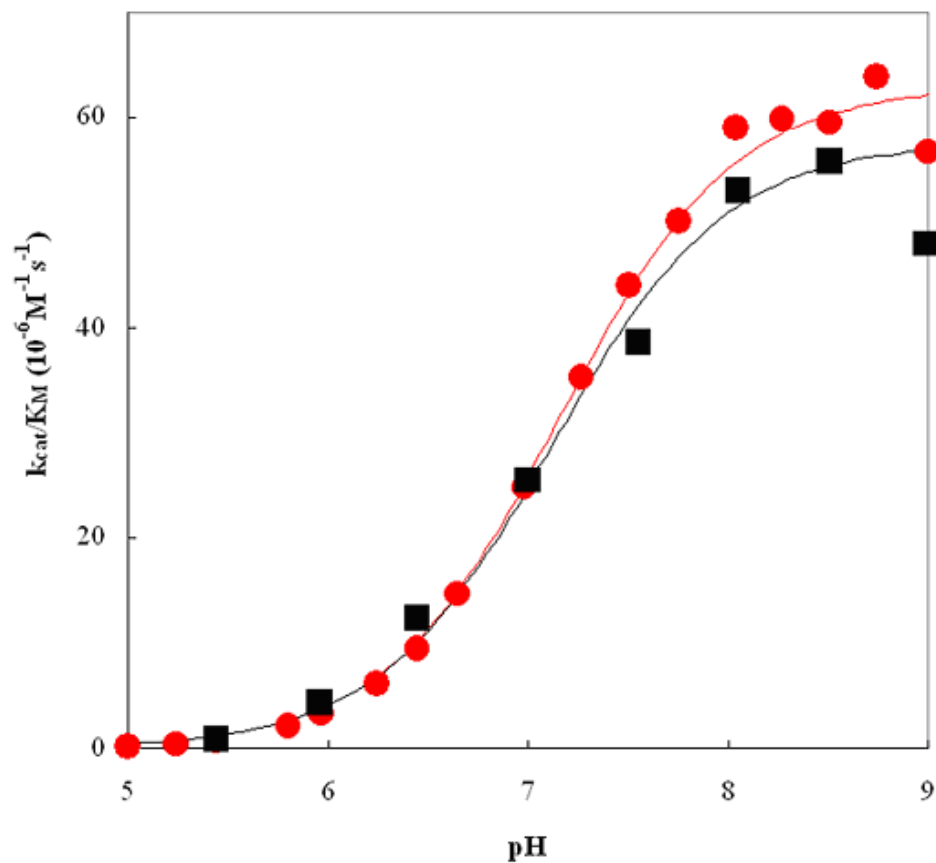


Figure 4-5. The pH profiles for k_{cat}/K_M catalyzed by hydrogenated and perdeuterated HCA II. (●) Perdeuterated soaked in D_2O , (■) Hydrogenated soaked in D_2O . Data were obtained at 25° in the absence of exogenous buffers using a total concentration of all species of CO_2 of 25 mM, with the ionic strength maintained at 0.2 M by addition of sodium sulfate. The solid lines are fit to a single ionization as described in Chapter 2.

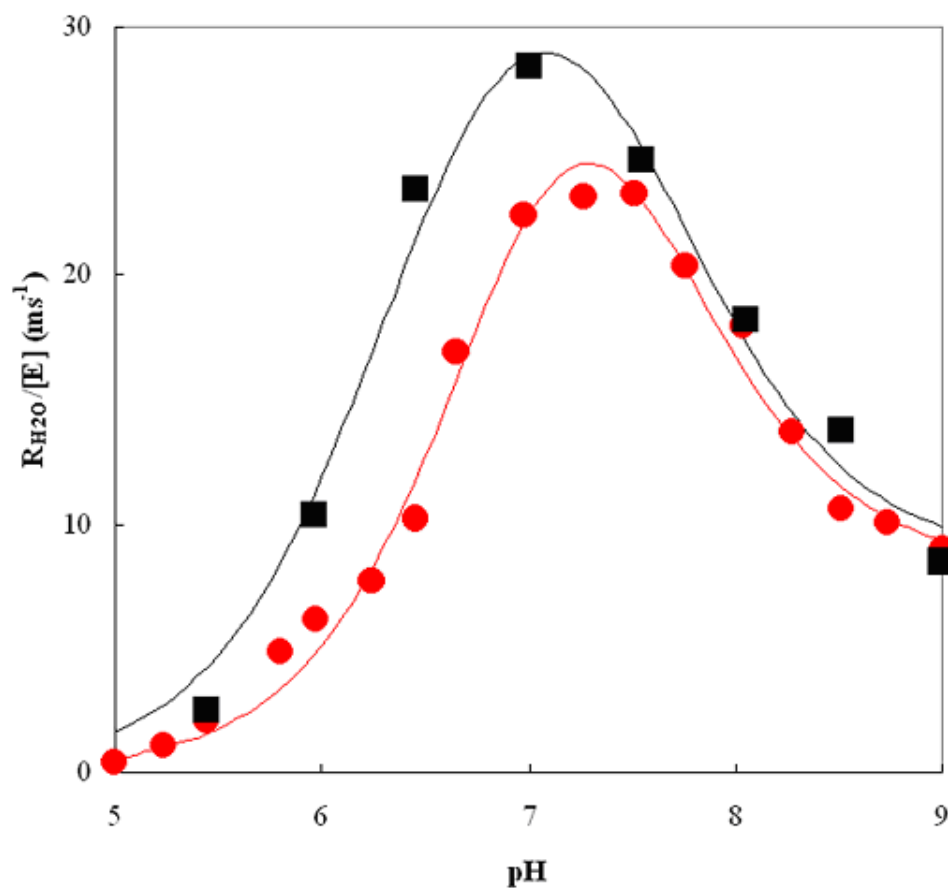


Figure 4-6. The pH profiles for $R_{H_2O}/[E]$ catalyzed by hydrogenated and perdeuterated HCA II. (●) Perdeuterated soaked in D_2O , (■) Hydrogenated soaked in D_2O . Data were obtained at 25° in the absence of exogenous buffers using a total concentration of all species of CO_2 of 25 mM, with the ionic strength maintained at 0.2 M by addition of sodium sulfate.

CHAPTER 5 NOVEL INHIBITORS AND THEIR BINDING MODES TO HCA II

Introduction

There is a wealth of information available on various CA inhibitors (CAI) and their kinetic and structural characterizations (For general review, see Mansoor *et al.* in *The Carbonic Anhydrases*, 2000; Supuran *et al.*, 2004). Briefly, various anions have historically been useful for studying the properties of the metal active site of CA and it is clear that most monovalent anions bind and inhibit CA activity to varying extents. These CAIs bind to the metal ion and interfere with the $ZnOH^-$ coordination by either displacing or replacing the hydroxide, thus disrupting catalysis (Bertini *et al.*, 1983).

The key group in determining this displacement/replacement is the hydroxyl of Thr199 and this residue is sometimes referred to as the gate keeper. Thr199 is a hydrogen bond acceptor and anionic inhibitors (eg. azide and cyanate) that have protonated groups can bind directly to the zinc ion, thus substituting the OH^- group and efficiently disrupts catalysis (Merz, 1990). Inhibitors that bind in this way maintain hydrogen bonding with Thr199 and participate in tetrahedral coordination of the metal center.

Another important class of strong, selective inhibitors is the aromatic and heterocyclic sulfonamides of the $R-SO_2NH_2$ or $R-SO_2NH(OH)$ form. Several crystal structures of complexes of various sulfonamide inhibitors with CA show similar interactions: the ionized NH group binds directly to the metal and simultaneously donates a hydrogen bond to the hydroxyl of Thr199 and an oxygen of the sulfonamide interacts

with the amide backbone of Thr199 and thus displaces the deep water (Figure 5-1; Nair *et al.*, 1995).

Clinically important drugs include acetazolamide (Diamox) and dorzolamide (Trusopt) and these compounds have application in the treatment of congestive heart failure, altitude sickness and glaucoma (Mansoor *et al.*, 2000) and now may also be useful in controlling mosquito populations, as described in Chapter 6.

CAIs are commonly prescribed for the treatment of glaucoma symptoms such as increased intraocular pressure. The application of topical inhibitors to the eye inhibits CA and decreases the secretion of sodium, bicarbonate, and aqueous humor thus lowering pressure in the eye (Maren, 1987). There is also considerable interest in CAIs for the treatment of cancer as aberrant expression of extracellular HCA isoform IX (HCA IX) has been associated with certain types of solid tumors. This overexpression has been observed in several cancers, including non-small-cell lung cancer and renal-cell carcinoma. The overabundance of HCA IX in solid tumors could help these cells in adapting to hypoxic conditions and, due to the acidification of the extracellular matrix, assist in metastasis (Wykoff *et al.*, 2000; Giatromanolaki *et al.*, 2001). Current CAIs that are clinically used are not very water soluble and it is thought that a drug with better solubility would have improved bioavailability (Kim *et al.*, 2005).

Two novel compounds, BB3 (2-amino-1,3,4-thiadiazolyl-5-difluoromethanesulfonamide) and TDM (2-dimethylamino-5-sulfonamido(aminomethyl)-1,3,4-thiadiazole), have an additional spacer group, either –CF₂– or –CHNH₂–, between the sulfonamide and thiadiazole ring moieties (Figure 5-2). These drugs have better solubility than the conventional glaucoma treatments and still bind CA with nanomolar

affinity (Boyle *et al.*, 2005). To investigate BB3 and TDM binding and their interactions with the HCA II active site, the crystal structures of the co-complexes were determined by X-ray crystallography to 1.60 and 1.15 Å, respectively.

Materials and Methods

Expression, Purification, and Crystallization

HCA II was overexpressed in *Escherichia coli* BL21(DE3)pLysS and affinity purified using p-aminomethylbenzenesulfonamide coupled to agarose, as described elsewhere (Khalifah *et al.*, 1977). Fractions were assessed for yield and purity by silver stained SDS-PAGE and fractions containing HCA II were pooled accordingly. HCA II was dialyzed against 50 mM Tris-Cl, pH 7.8 and then concentrated to ~ 15 mg/ml with Amicon Ultra centrifugation filtration devices. Protein concentration prior to crystallization was determined by measuring the optical density at 280 nm and assuming a molar absorbance of $5.5 \times 10^4 \text{ M}^{-1}\text{cm}^{-1}$. Hanging drop crystals were prepared by mixing 5 µl of protein (~ 15 mg/ml in 50 mM Tris-Cl pH 7.8) with 5 µl precipitant (50 mM Tris-Cl pH 7.8, 2.6 M ammonium sulfate) (McPherson, 1982). The drops were equilibrated at room temperature against 1000 µl reservoir solution. Diffraction quality crystals appeared within 2-3 days. The inhibitors were solubilized in water to a final concentration of 20 µM. For the drug soaks, sitting drops using microbridges, were set up with 10 µl drop size. Prior to adding single, pre-grown crystals the soluble drugs were added to a final concentration of 1 µM. Crystals were allowed to soak for at least 24 hours prior to data collection.

Synchrotron X-ray Data Collection

All crystals were quick-dipped in cryoprotectant (30% glycerol in reservoir solution) before flash-freezing at 100 K for X-ray data collection. Diffraction data for the

BB3-complex were collected at Brookhaven National Laboratory beamline X29 on a Quantum 315 CCD detector using a wavelength of 1.100 Å. Crystal to detector distance was set to 100 mm and a total of 297 images were collected with an oscillation angle of 1°. Diffraction data for the TDM-complex were collected at Cornell High Energy Synchrotron Source beamline A1 on a Quantum 210 CCD detector with a wavelength of 0.978 Å. The crystal to detector distance was 100 mm and a total of 410 images were collected with an oscillation angle of 1°. All data set statistics for both complexes are given in Table 5-1.

Structure Determination and Model Refinement

Diffraction data were indexed and reduced with DENZO and SCALEPACK from the HKL program suite (Otwinowski and Minor, 1997). The data were phased with molecular replacement methods as implemented in the software package Crystallography and NMR Systems (CNS) version 1.1 (Rossmann, 1990; Brünger *et al.*, 1998). The structure of wild type HCA II was used as a starting model (PDB accession code 1TBT; Fisher *et al.*, 2005). After initial cycles of rigid body refinement, simulated annealing to 3000 K with gradual cooling, geometry-restrained positional, and individual temperature factor refinement, $F_o - F_c$ omit electron density maps were calculated. Visual inspection of these maps clearly revealed the position of the zinc, solvent, and the inhibitors. Coordinates and topology files for the inhibitors were generated with the PRODRG server (<http://davapc1.bioch.dundee.ac.uk/programs/prodrng>) and were subsequently built into the respective electron density (Schüttelkopf and van Aalten, 2004). After the initial refinement routines in CNS the R_{work} and R_{free} were 0.193 and 0.224 for the BB3 complex and 0.225 and 0.236 for the TDM complex, respectively.

At this point the refinement was moved into SHELXL97 with the conjugate gradient least squares (CGLS) mode using default restraints for protein geometry (Sheldrick and Schneider, 1997; Engh and Huber, 1991). After each round of CGLS refinement, F_o-F_c and $2F_o-F_c$ electron density maps were generated and the model and maps visually inspected using the molecular graphics program Coot (Emsley and Cowtan, 2004). Manual adjustments to side chains and inhibitor positions were done at this point. After several rounds of refinement, automated water placement was performed with SHELXPRO using F_o-F_c omit maps with a 4σ cut-off (Sheldrick and Schneider, 1997). For the high resolution TDM complex structure all non-hydrogen atoms were refined anisotropically using the SHELXL97 default anisotropic displacement parameters (Sheldrick and Schneider, 1997). For BB3 only the zinc and sulfur atoms were refined anisotropically. Manual model building in Coot involved modeling of alternate conformations (Ile22 and Lys39 for TDM complex) and addition/removal of solvent. Refinement of both structures continued until the R factors converged. The final R_{cryst} and R_{free} were 0.167 and 0.212 for BB3, and 0.136 and 0.166 for TDM, respectively. All model geometries were analyzed by PROCHECK and enzyme:inhibitor interactions were determined with LIGPLOT (Laskowski *et al.*, 1993; Wallace *et al.*, 1995). Data refinement and final model statistics are given in Table 5-1.

Results and Discussion

The crystal structures of HCA II, in complex with BB3 and TDM, reported here were isomorphous with previously determined HCA II and had unit cell dimensions as shown in Table 5-1. The final, refined models had good geometry and all backbone torsion angles fell within acceptable regions on a Ramachandran plot. The model of the

BB3 complex (to 1.6 Å) had an R_{cryst} and R_{free} of 0.167 and 0.212, while TDM (to 1.15 Å) had an R_{cryst} and R_{free} of 0.136 and 0.166, respectively (Table 5-1).

Both compounds used in this study contain the classically employed sulfonamide moiety that anchors the rest of the inhibitor in the active site. From the structure it is clear that the ionized –NH group displaces the zinc-bound solvent and makes a hydrogen bond with Thr199 in the same way that has been observed in other complexed structures (Figure 5-1 to 5-4). The N3 from the sulfonamide group of BB3 and TDM is 2.8 and 2.9 Å away from the hydroxyl of the side chain of Thr199, respectively (Figure 5-5). The novel compounds are different from the classical CAIs in that they contain a spacer group between the zinc-anchoring sulfonamide group and thiadiazole ring (Figure 5-2). BB3 contains a difluoromethane group while TDM contains an aminomethyl group. It is clear from the high resolution electron density maps that these compounds adopt unique binding modes compared to other clinically used CAIs (Figure 5-4).

In the BB3 complex structure the difluoromethane group allows rotational flexibility between the sulfonamide and thiadiazole ring. This feature allows the aromatic ring of BB3 to fold back and π -stack with the imidazole of His96, one of the zinc ligands (Figure 5-5 (a)). This folding back is unique as the other CAIs adopt a more extended conformation that leads out of the active site. Also, as can be seen from the features of the electron density, the ring of BB3 is planar. Apart from the π -stacking interaction, there is also an inferred hydrogen bond between F2 of BB3 and OG1 of Thr200 with a distance of 2.5 Å. There are also two other direct hydrogen bonds between N1 and NH2 of the thiadiazole ring and residues Gln92 and Asn62. The only indirect hydrogen bond is between NH2 and Asn62 that occurs through a solvent molecule, W369 (Figure 5-5 (a)).

To address the issue of whether the observed π -stack is a result of the spacer group insertion or a specific feature of the difluoromethane group, an analogous compound (TDM) was synthesized that contained an aminomethyl group as the spacer (Figure 5-2). In the crystal structure of the TDM-HCA II complex, no π -stacking interaction with any His was observed. Also, the thiadiazole ring shows puckering, compared to BB3 that has a planar ring. (Figure 5-3 (b)). The ring also occupied a different position compared to BB3 and acetazolamide (Figure 5-4). To more clearly demonstrate the different binding modes, both BB3 and TDM were superimposed in the active site of HCA II with the view rotated to highlight these differences, as indicated in Figure 5-6.

There are two indirect hydrogen bonds from TDM to Asn67 that are mediated by two solvent molecules, W316 and W599 (Figure 5-5 (b)). In contrast to the hydrogen bond between F2 and Thr200 of BB3, there is no hydrogen bonding interaction between the aminomethyl spacer group of TDM and Thr200. This is due to the ring being in a different position compared to BB3 and this has displaced the aminomethyl group away from any potential interactions. The dimethyl moiety of TDM occupies a hydrophobic region of the HCA II active site comprised of Phe131 and Leu198 (Figure 5-5 (b)).

Conclusion

Carbonic anhydrases are interesting and clinically relevant targets for the development of new inhibitors. Such compounds will have implications for both pharmaceutical, industrial, and research applications. CAIs are routinely prescribed for the treatment of various diseases, such as glaucoma and altitude sickness, and recently has shown potential for treating certain tumor types. Classical CAIs have poor solubility and bioavailability and new compounds with better chemical properties could have novel clinical uses. This work showed the binding and interactions of two new water-soluble

compounds, BB3 and TDM, and their interactions with HCA II by X-ray crystallographic methods. These compounds are unique in that they contain two different kinds of spacer groups between the sulfonamide and thiadiazole groups. The spacers confer interesting properties on the inhibitors and cause them to bind in different modes than what have been observed before. These alternate binding locations in the active site of HCA II could provide useful information for the future development of isoform specific inhibitors.

Table 5-1. Data collection, refinement and final model statistics.

	BB3	TDM
Space group	P2 ₁	P2 ₁
Unit cell parameters (Å, °)	$a = 42.3, b = 41.4,$ $c = 72.1, \beta = 104.1$	$a = 42.5, b = 41.6,$ $c = 72.7, \beta = 103.9$
Resolution (Å)	20.0 – 1.60 (1.66 – 1.60)*	20.0 – 1.15 (1.19 – 1.15)
No. unique reflections	32031 (3154)	87379 (7896)
Completeness (%)	99.9 (100.0)	97.9 (89.3)
Redundancy	4.4 (4.3)	7.0 (4.1)
Overall I/σ(I)	17.1 (4.2)	26.4 (4.7)
R _{sym} [§]	0.066 (0.209)	0.099 (0.323)
R _{cryst} [∫] / R _{free} [‡]	0.167 / 0.212	0.136 / 0.166
Rmsd bond lengths/angles	0.009 / 1.490	0.010 / 1.315
Average B-factors		
Main/side/solvent/inhibitor	16.7/23.2/31.8/21.5	14.1/17.5/32.9/16.5
No. solvent molecules	246	310
Ramachandran Statistics (%)		
Most favored/ additionally allowed	87.9/12.1	88.8/11.2

*Data in parenthesis is for the highest resolution shell.

$$^{\S} R_{\text{sym}} = \frac{\sum |I - \langle I \rangle|}{\sum I}$$

$$^{\int} R_{\text{cryst}} = \frac{\sum |F_{\text{obs}}| - k \sum |F_{\text{calc}}|}{\sum |F_{\text{obs}}|}$$

[‡] R_{free} is calculated the same way as R_{cryst} except for 5% of data omitted from refinement.

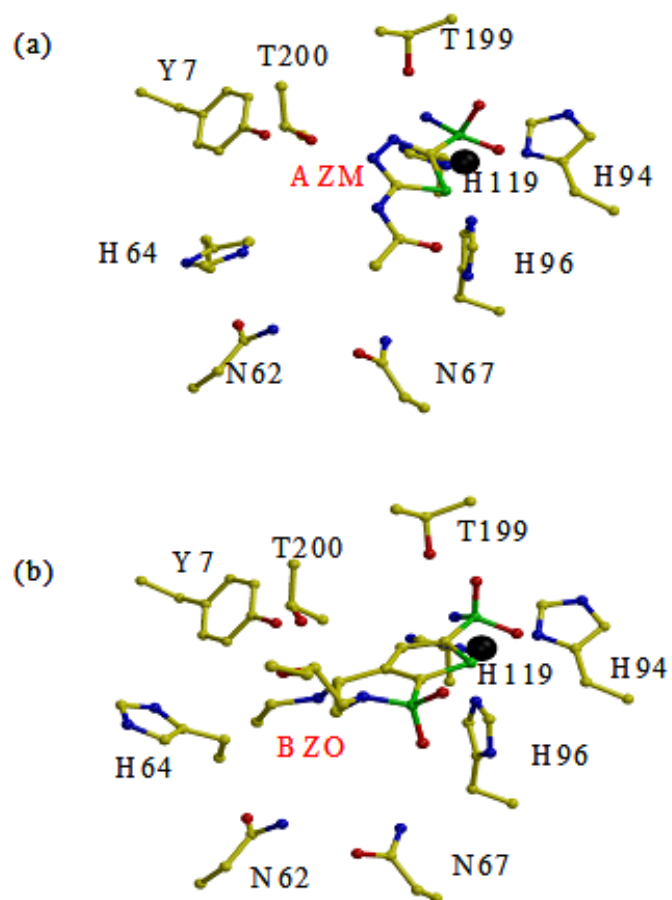


Figure 5-1. Classical carbonic anhydrase inhibitors bound to HCA II. (a) Acetazolamide (AZM), (b) Brinzolamide (BZO). Active site residues are as labeled and the zinc is shown as a black sphere. PDB accession codes for (a) 1AZM (Chakravarty and Kannan, 1994); (b) 1A42 (Stams *et al.*, 1998). Figure was generated and rendered with BobScript and Raster3D (Esnouf, 1997; Merritt and Bacon, 1997).

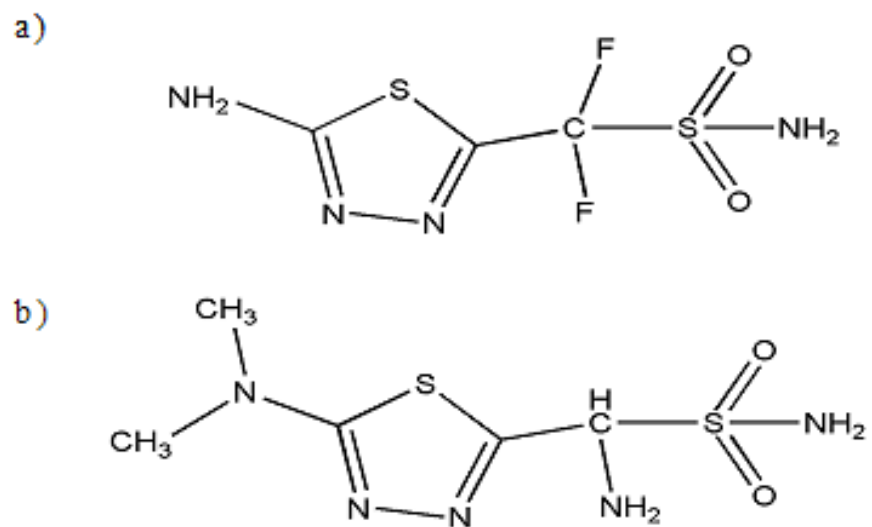


Figure 5-2. Chemical structure of novel inhibitors. (a) BB3, and (b) TDM. Figure was generated with ChemDraw.

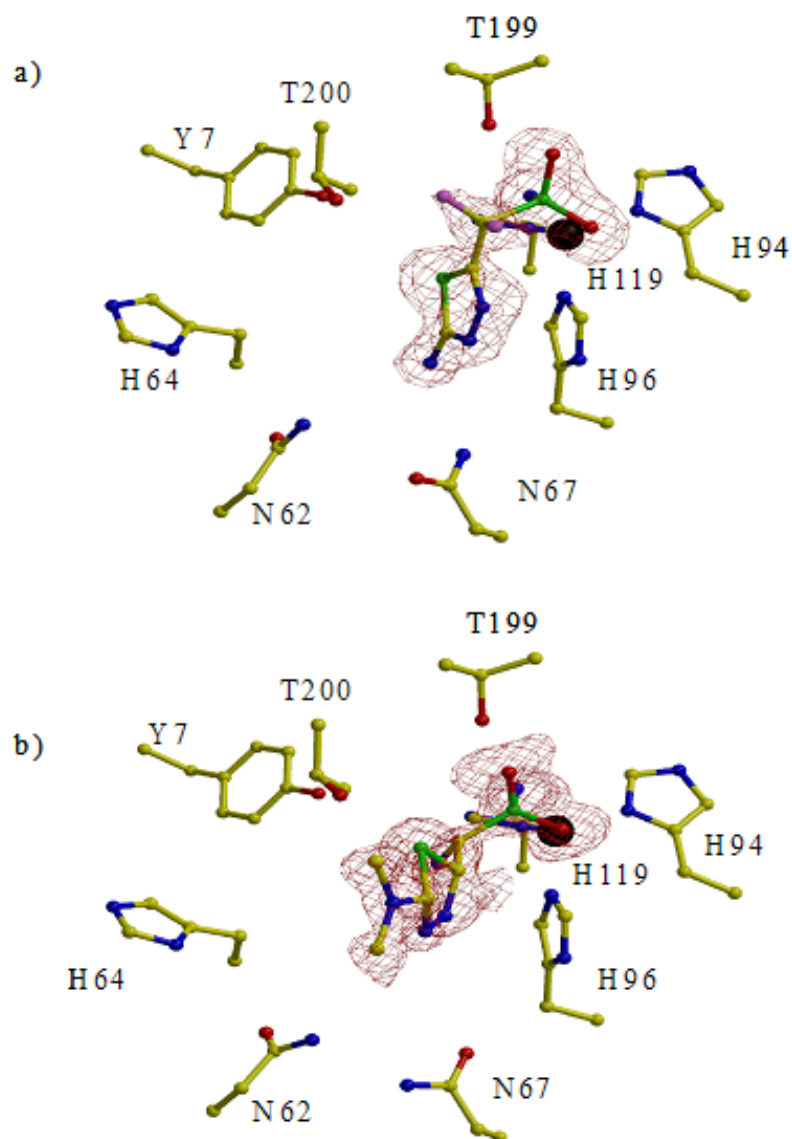


Figure 5-3. Active site structures of HCA II in complex with two novel inhibitors. (a) BB3, and (b) TDM. Active site residues are shown in yellow ball-and-stick and are as labeled. The zinc atom is shown as a black sphere. The red mesh electron densities are F_o-F_c maps contoured at 2σ and was calculated without the inhibitor present. Figure was generated and rendered with BobScript and Raster3D, respectively (Esnouf, 1997; Merritt and Bacon, 1997).

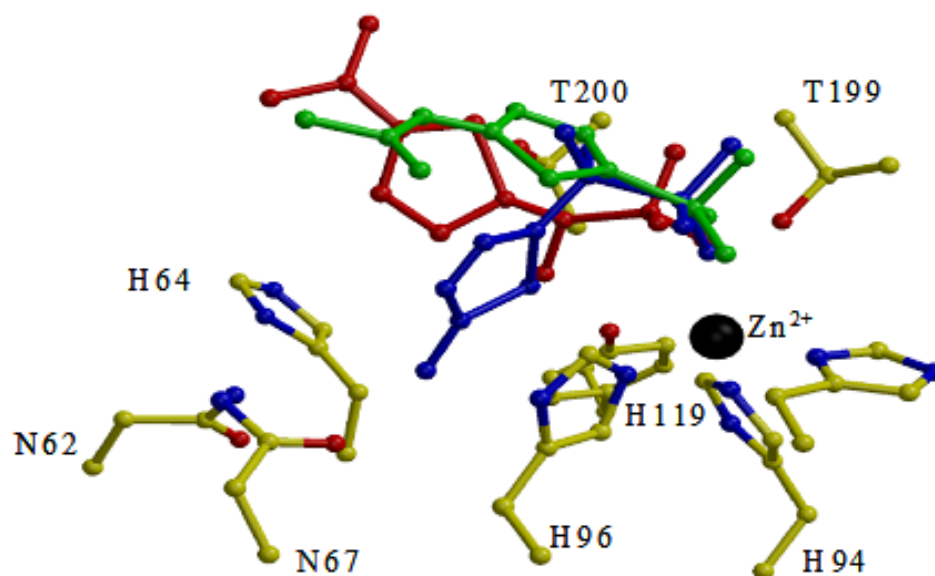


Figure 5-4. HCA II active site with inhibitors superimposed. Active site residues are shown in yellow ball-and-stick and the zinc atom is a black sphere. BB3 is shown in blue, TDM in red, and acetazolamide is shown in green. PDB accession code for acetazolamide coordinates: 1AZM (Chakravarty and Kannan, 1994). Figure was generated and rendered with BobScript and Raster3D, respectively (Esnouf, 1997; Merritt and Bacon, 1997).

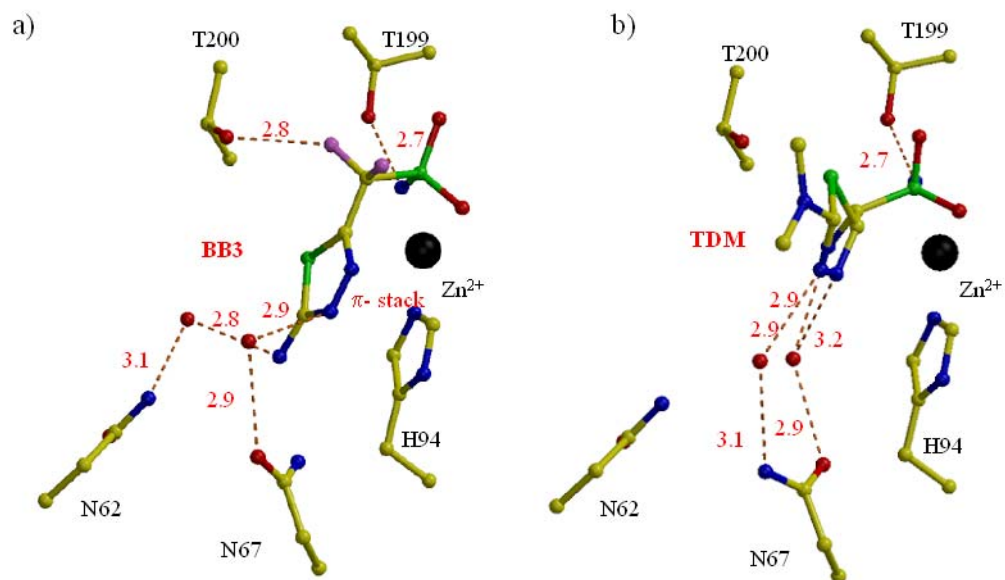


Figure 5-5. Interactions of BB3 and TDM with HCA II. (a) BB3, and (b) TDM. Active site residues are shown in yellow ball-and-stick, as labeled, with the zinc atom as a black sphere. Hydrogen bond distances are as indicated. Figure was generated and rendered with BobScript and Raster3D, respectively (Esnouf, 1997; Merritt and Bacon, 1997).

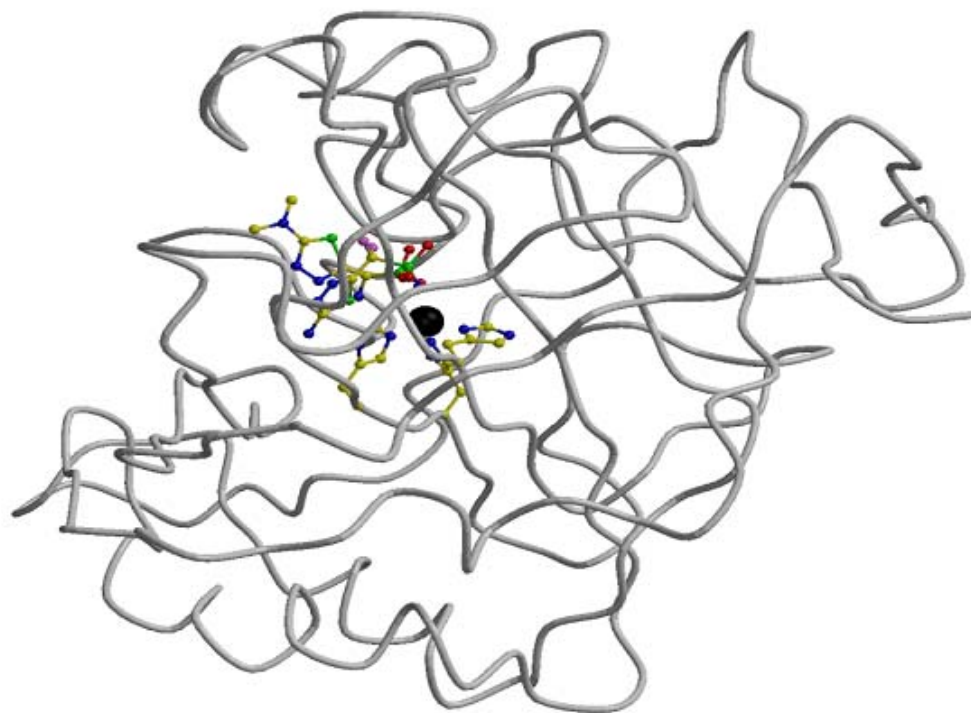


Figure 5-6. HCA II with BB3 and TDM superimposed. Zinc and zinc ligands are shown as a black sphere and yellow ball-and-stick, respectively. The two inhibitors are shown in yellow ball-and-stick also. Figure was generated with BobScript and Raster3D, respectively (Esnouf, 1997; Merritt and Bacon, 1997).

CHAPTER 6
EXPRESSION, PURIFICATION, KINETIC, AND STRUCTURAL
CHARACTERIZATION OF AN ALPHA-CLASS CA FROM AEADES AEGYPTI
(AACAI)

Introduction

Overall, the α -class of CAs are present in vertebrates, but are also found in invertebrates such as fruit flies and mosquitoes (Del Pilar Corena *et al.*, 2002). Recently, another α -CA was identified from the midgut of *Aedes aegypti* larvae. Subsequent sequence comparisons showed it to be homologous to human isoforms I and II with 39% and 32% sequence identity, respectively (HCA I and HCA II; Figure 6-1). Biochemical analysis also showed the protein to be a glycosyl-phosphatidylinositol-linked membrane associated CA, similar to HCA IV with 27% sequence identity (Del Pilar Corena *et al.*, 2002; Seron *et al.*, 2004). Due to the high similarity to HCA I, this protein was named AaCA1 (Genbank accession number AF395662). It has been suggested this CA produces bicarbonate ions that are needed in the midgut to help buffer the extreme alkaline environment (\sim pH 11) found there. This high pH is required for the digestion of plant materials that larvae ingest during this development stage (Martin *et al.*, 1980). Recent experimental evidence that supports the essential role of CA in these organisms showed that treatment with CA inhibitors (CAIs) blocks midgut alkalization and cause death of the mosquito larvae (Del Pilar Corena *et al.*, 2004).

All CAs use the same zinc-hydroxide mechanism of catalysis for the reversible hydration/dehydration of CO₂ through a nucleophilic attack by the zinc-bound hydroxide. The product, bicarbonate, is easily replaced by a water molecule and freely diffuses out

of the active site (Lindskog, 1997; Christianson and Fierke, 1996). The hydroxide at the zinc is then regenerated through a series of proton transfer events that are thought to occur via a well-ordered and conserved water network that connects the zinc-bound solvent and proton shuttle His64 (HCA II numbering) (Tu *et al.*, 1989; Fisher *et al.*, 2005). A detailed discussion of the catalytic mechanism can be found in Chapter 2.

In catalytically active CAs the zinc ion is tetrahedrally coordinated by three His residues (His94, 96, and 199) and a solvent ligand. Thr199 assists by making a hydrogen bond with the zinc-bound solvent to optimally orient it for nucleophilic attack of the incoming substrate (Merz, 1990). Based on mutagenesis, kinetic, and structural studies of amino acids that line the active site cavity, a detailed picture has evolved as to the relevance of these residues. In HCA II the side chains of residues Tyr7, Asn62, Asn67, and Thr200 are all believed to be involved in stabilizing several active site waters that constitute the solvation structure that could promote efficient proton transfer from the zinc-bound solvent to His64. Mutagenesis on any of these residues have been shown to have considerable effects on proton transfer (Fisher *et al.*, 2005; Krebs *et al.*, 1991; Bhatt *et al.*, 2005).

Mosquitoes act as vectors for many important human pathogens that cause diseases such as dengue fever, malaria, and yellow fever. According to the American Mosquito Control Association, there are more than 2500 different species of mosquitoes worldwide and 150 of these occur in the U.S.A. (Darsie and Ward, 2000; Spielman *et al.*, 2001). Recent reports indicate that between fifty million and one hundred million cases of dengue fever appear annually. There are also an additional several hundred thousand occurring cases of the lethal dengue hemorrhagic fever (Halstead, 1997). Alarming, the

incidence of mosquito-borne diseases has been increasing dramatically in recent years, most likely due to the spread of certain disease-carrying species such as *Aedes aegypti* and *Anopheles gambiae* (Gubler, 1997). The discovery of an α -class CA in mosquitoes presents an interesting new drug target for the potential regulation of mosquito populations. This chapter describes the bacterial expression, purification, kinetic characterization, and structural modeling of the soluble CA domain of AaCA1 from *Aedes aegypti*. This work has important applications for the development of drugs specific for mosquito CAs and lays the initial foundation for future crystallographic structure determinations of such CAs.

Materials and Methods

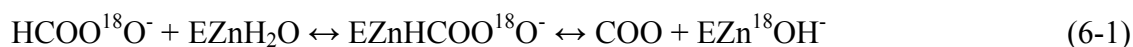
Expression and Purification

A pET100/D-TOPO (Invitrogen Corporation) plasmid containing the truncated gene for AaCA1 (residues 17-275, indicated by the black arrows in Fig. 1) was generated as previously described (Seron *et al.*, 2004). The coding region was removed by digestion of plasmid DNA with restriction enzymes, NcoI and BamHI (New England Biolabs). The linearized insert was then gel-purified and ligated into a modified pET vector, pET81-flp, which was constructed by Tanhauser *et al.* as described elsewhere (Tanhauser *et al.*, 1992). Correct insertion and orientation of the gene was verified by sequencing the resulting plasmid. Expression of the truncated, soluble region of AaCA1 was performed in *E. coli* BL21(DE3) pLysS cells that were grown to an optical density of ~ 0.30 as measured at a wavelength of 600 nm. Protein expression was then induced by the addition of 1 mM IPTG and 1 mM ZnSO₄ was also added for uptake in the expressed protein. At 4 hours post-induction, cells were harvested by centrifugation and the cell pellets frozen at -20 °C overnight. Cell pellets were lysed by freeze/thawing and

solubilized in 0.2 M sodium sulfate, 50 mM Tris-Cl (pH 9.0). The soluble cell fraction was obtained by centrifuging the lysates at 100,000 x g for 1 hour at 4 °C. AaCA1 was further purified from the supernatant by affinity chromatography using p-amino-methyl-benzenesulfonamide (pAMBS; a specific binder to the active site of α -CAs) coupled to agarose beads as described elsewhere (Khalifah *et al.*, 1977). Purity of the protein was verified by electrophoresis on a 12% polyacrylamide gel stained with Coomassie (Figure 6-2). Prior to further analysis, the protein was buffer-exchanged into 50 mM Tris-Cl (pH 7.8) using Amicon Ultra centrifugation devices.

Activity Analysis by ^{18}O Exchange

This method is based on the measurement using membrane-inlet mass spectrometry of the exchange of ^{18}O between CO_2 and water at chemical equilibrium (eqs 6-1 and 6-2) (Silverman, 1982).



An Extrel EXM-200 mass spectrometer with a membrane inlet probe was used to measure the isotopic content of CO_2 . Solutions contained a total concentration of all species of CO_2 of 25 mM, and the ionic strength was maintained by the addition of 0.2 M sodium sulfate. Analysis of ^{18}O -exchange data are described in detail elsewhere (Silverman, 1982; An *et al.*, 2002). This approach yields $k_{\text{cat}}/K_{\text{M}}$ as can be obtained by steady state methods. The pH dependence of $k_{\text{cat}}/K_{\text{M}}$ depends on the ionization state of the zinc-bound water, as shown in eq 6-3.

$$k_{\text{cat}}/K_{\text{M}} = (k_{\text{cat}}/K_{\text{M}})_{\text{max}}(1 + [\text{H}^+]/(K_{\text{a}})_{\text{ZnH}_2\text{O}})^{-1} \quad (6-3)$$

A second rate determined by the ^{18}O exchange method is $R_{\text{H}_2\text{O}}$, the rate of release from the enzyme of water-bearing substrate oxygen (eq 6-2). The pH dependence of $R_{\text{H}_2\text{O}}/[\text{E}]$ is often bell-shaped, consistent with the transfer of a proton from a single predominant donor to the zinc-bound hydroxide. In these cases, the pH profile is adequately fit by eq 6-4 in which k_{B} is a pH-independent rate constant for proton transfer, and $(K_{\text{a}})_{\text{donor}}$ and $(K_{\text{a}})_{\text{ZnH}_2\text{O}}$ are the noninteracting ionization constants of the proton donor BH^+ of eq 6-2 and the zinc-bound water.

$$k_{\text{B}}^{\text{obs}} = k_{\text{B}} / \{ [1 + (K_{\text{a}})_{\text{donor}} / [\text{H}^+]] [1 + [\text{H}^+] / (K_{\text{a}})_{\text{ZnH}_2\text{O}}] \} \quad (6-4)$$

All pH data were obtained at 25 °C in the absence of buffer using a total concentration of all species of CO_2 of 25 mM, with the ionic strength maintained at 0.2 M by addition of sodium sulfate.

Determination of Inhibition Constants

Inhibition constants for tight-binding sulfonamides were determined by titration of the ^{18}O -exchange activity with methazolamide or ethoxzolamide (Maren and Conroy, 1993; Maren and Sanyal, 1983). Data were analyzed by the method of Henderson and fitting the data with Enzfitter (Biosoft) (Segal, 1975).

Model Building

A molecular model of AaCA1 was built using the Swiss-Model facility with HCA I as a template (PDB accession code: 1AZM) (Chakravarty and Kannan, 1994). Swiss-Model is an automated protein structure homology modeling server available at <http://www.expasy.org> (Peitsch, 1996; Guex *et al.*, 1999; Schwede *et al.*, 2003). Model analysis, visualization, and manipulation were performed using the programs Coot and GRASP (Emsley and Cowtan, 2004; Nicholls *et al.*, 1991).

Results and Discussion

Expression and purification of AaCA1 from the *E. coli* BL21(DE3) pLysS expression system typically gave yields of ~ 40 mg purified protein from 1 L of cells (Figure 6-2). Gel lane 2 shows the cell lysate at the time of induction, and lane 3 was taken at 3 hours post-induction. There is a distinct band at ~ 30 kDa in lane 3 that corresponds to overexpressed AaCA1.

Lane 4 is the soluble fraction of the cell lysate that was loaded onto the affinity resin and AaCA1 was found exclusively here. Lane 5 represents the unbound material that did not bind to the affinity resin, and a comparison of lanes 4 and 5 shows that all of the AaCA1 bound to the affinity resin. Lanes 6-8 are different fractions of the protein that were collected at elution of the affinity resin.

After buffer exchange and concentration of the enzyme, denaturing polyacrylamide gels were silver-stained, and the protein was estimated to be more than 95% pure. The protein had limited solubility at concentrations over 1 mg/ml, but was stable at 1 mg/ml in 50 mM Tris-Cl, pH 7.8 at 4 °C.

Kinetic analysis reveals that AaCA1 is a highly efficient CA isoform with k_{cat}/K_M for hydration of carbon dioxide at $67 \pm 3 \mu\text{M}^{-1}\text{s}^{-1}$ and a kinetic pK_a of 6.7 ± 0.1 (Figure 6-3a). The magnitude of this rate constant is more similar to HCA I than HCA II (Table 6-1). This was to be expected as AaCA1 has an overall higher sequence homology to HCA I than that of HCA II (39% and 32% sequence identity, respectively, Figure 6-1). In terms of k_B the rate constant for proton transfer, however, AaCA1 displayed a rate constant more typical of HCA II with maximal activity near pH 6.5 (Table 6-1; Figure 6-3b).

Determination of inhibition constants (K_i) with sulfonamide drugs methazolamide and ethoxzolamide reveal that these inhibitors bind tightly to AaCA1, with K_i s of $2.7 \pm$

0.3 and 1.9 ± 0.3 nM, respectively, as determined from the ^{18}O -exchange method. These results are very similar to those previously obtained for HCA I and HCA II; for each of these enzymes the inhibition constants were 10 nM for methazolamide and 2 nM for ethoxzolamide, determined by a buffer-titration method (Sanyal *et al.*, 1982).

The sequence alignment of AaCA1 with HCA I and II shows the high level of conservation between these CAs (Figure 6-1). This high sequence preservation led to the construction of a reliable three-dimensional molecular model of AaCA1 (Figure 6-4). Superposition of the AaCA1 model onto the crystal structures of HCA I and HCA II gave root mean square deviations for C_{α} s of 0.8 and 1.2 Å, respectively (Fisher *et al.*, 2005; Chakravarty and Kannan, 1994).

As the sequence alignment suggested, the general fold and active site architecture is conserved to that of HCA I and II. An interesting structural feature of AaCA1 is that there are two additional cysteine residues (Cys40 and Cys217; highlighted yellow, Figure 6-1) that are not present in the sequences of HCA I or II, and the model predicts that these residues are close enough to form a disulfide bond (Figure 6-4b). Interestingly, HCA XII and murine CA XIV also have cysteine residues at equivalent position compared to AaCA1, and their crystal structures have shown that they do form an intermolecular disulfide bond (Whittington *et al.*, 2001; Whittington *et al.*, 2004).

The AaCA1 molecular model shows three histidine residues (His111, 113, and 130) that are equivalent to His94, 96, and 119, which are the protein ligands to the zinc in HCA I and II (Figure 6-5). Also, residues threonine 213 and 214, and histidine 83 of AaCA1 correspond to Thr199, Thr200, and the proton shuttling His64 of HCA II, respectively, whereas HCA I has a histidine at position 200. There are, however, key

active site differences between AaCA1 and HCA I (other than the Thr200 position, HCA II numbering) and HCA II. AaCA1 has a threonine at position 81 and a glutamine at position 86, whereas HCA II has asparagines at both positions (HCA II numbering 62 and 67, respectively) while HCA I has a valine at 62 and a histidine at 67. Hence, AaCA1 and HCA II have different polar amino acids at these positions, whereas HCA I has a hydrophobic valine in the active site.

In the AaCA1 model, residues Thr81 and Gln86 point towards the active site, and could therefore be reasonably expected to hydrogen-bond and contribute to a solvent molecule architecture in the active site that resembles that of HCA II. In contrast to HCA II and AaCA1, HCA I has a histidine at position 200 (HCA II numbering) instead of a threonine, and a hydrophobic valine in the active site (Figure 6-5). The observation that AaCA1 would have a solvated active site, more like HCA II than I, supports the measurements of the efficient proton transfer rate constant, k_B , for AaCA1, which is comparable to HCA II (Table 6-1) (Khalifah, 1971).

Inspection of the AaCA1 model gives no clear explanation of why the k_{cat}/K_M for hydration of CO_2 for AaCA1 is more similar to HCA I than HCA II, as the residues that line the proposed substrate hydrophobic pocket (Val121, Val143, Leu198, Val207, and Trp209, HCA II numbering) are conserved in all three CAs (highlighted green, Figure 6-1). Hence this variation might be influenced by the numerous secondary shell interactions forming this pocket, and as AaCA1 overall sequence similar is more like HCA I than II this might account for the observed differences.

The N-terminus of AaCA1 could not be modeled with certainty because of a six amino acid insertions compared to HCA I and II (Figure 6-1). In the sequence alignment,

tyrosine 7 in HCA II appears conserved among AaCA1, HCA I, and HCA II. However, closer inspection of the AaCA1 model shows Asn27 (highlighted in red, Figure 6-1) at the same structural position (Figure 6-5a, c, and e) as Tyr7 in HCA I and II.

There could be structural conservation of a tyrosine at that position of AaCA1, and the insertion loop could be displaced. Alternately, Asn27 could potentially be in the position where the model indicates, and this would have implications for active site architecture and catalysis by AaCA1.

Despite the high sequence identity among AaCA1, HCA I, and HCA II, there are morphological differences between them that are reflected in their overall surface topology and charge distribution (Figure 6-5b, d, and f). HCA I and HCA II seem more compact and globular compared to AaCA1 and appear to have a more even charge distribution.

AaCA1 has a much higher overall calculated negative charge (-7.0) when compared to HCA I (-1.0) and HCA II (-2.0) at physiological pH (Figure 6-5b, d, and f). This surface feature might be related to the cellular location of this isoform at the cell membrane as a glycosyl-phosphatidylinositol-linked protein, while HCA I and HCA II are soluble cytosolic proteins.

Conclusion

A previously cloned α -CA from the mosquito *Aedes aegypti*, AaCA1, has been successfully expressed and purified to near homogeneity from a bacterial system (Figure 6-2) and subsequently kinetically characterized (Figure 6-3). The kinetic data presented here reveal that AaCA1 is a highly active isoform that has catalytic features resembling both HCA II and HCA I (Table 6-1), despite higher sequence identity with the latter

(Figure 6-1). Specifically, proton transfer capacity appears similar to HCA II and the rate constant for conversion of CO₂ to bicarbonate k_{cat}/K_m appears similar to HCA I.

A homology model of AaCA1 has provided information on the overall fold, active site, and surface charge distribution, compared to HCA I and II (Figure 6-4 and 6-5). Based on the sequence alignment and model, it has been shown that critical catalytic residues found in HCA II are conserved in AaCA1. A structural rationale of why AaCA1's proton transfer properties are more like HCA II than HCA I, is the conservation of residues threonine 214 (Thr200 in HCA II) that is a histidine in HCA I, and the conservation of polar amino acids in the active site, whereas HCA I has a valine (Figure 6-5).

Also of interest are the amino acid differences in the active site of AaCA1 at positions Thr81 and Gln86, compared to the structurally equivalent amino acids for HCA I (Val62 and His67) and HCA II (Asn62 and 67) as these amino acid side chains could be useful to design selective CAIs as potential drug target against mosquitoes and not humans.

Table 6-1. Maximal values of k_{cat}/K_m for the hydration of CO_2 and k_B for the proton transfer dependent release of H_2^{18}O from isoforms of carbonic anhydrase.

Isoform	k_{cat}/K_m ($\mu\text{M}^{-1}\text{s}^{-1}$)	k_B (μs^{-1})
Human CA I	50 ^a	0.1 ^a
Human CA II	150 ^a	0.8 ^b
AaCA1	67 +/- 3	1.1 +/- 0.2

^a From Khalifah, 1971.

^b From Duda *et al.*, 2001.

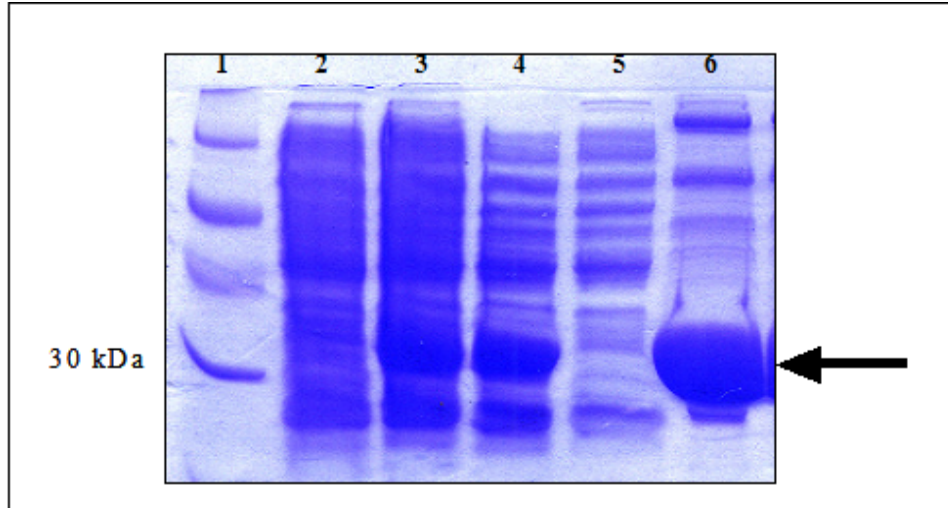


Figure 6-2. The 12% Coomassie stained polyacrylamide gel of AaCA1 expression and purification. Lane 1 – low molecular weight marker; lane 2 - lysate at induction; lane 3 – lysate at 3 hours post-induction; lane 4 – soluble lysate loaded onto affinity resin; lane 5 – unbound/flow through material from affinity purification; lanes 6 - fraction collected from elution of affinity purification. Arrow indicates AaCA1.

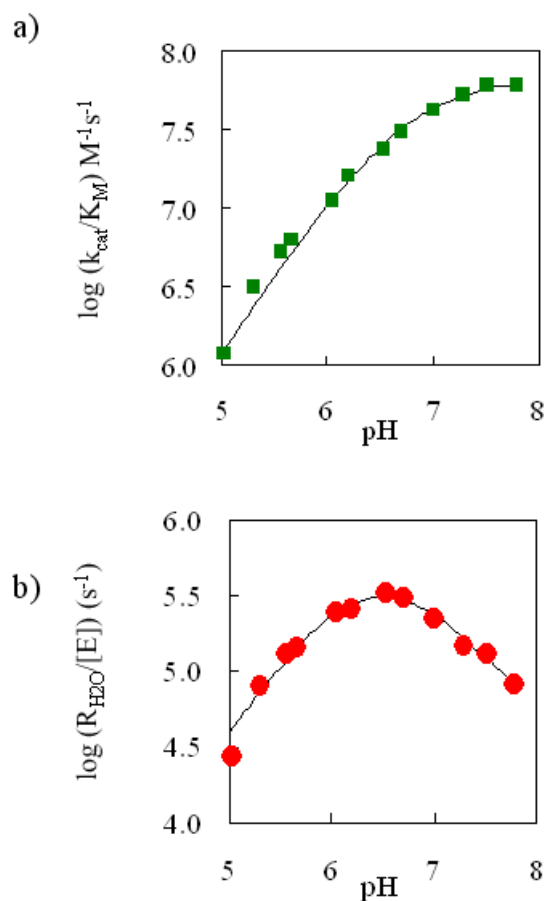


Figure 6-3. The pH profile of rate constants for catalysis by AaCA1. (a) pH profile for k_{cat}/K_m ($\text{M}^{-1}\text{s}^{-1}$) for hydration of CO_2 catalyzed by AaCA1 determined by ^{18}O exchange. The solid line is a fit to eq 5 with $(k_{\text{cat}}/K_m)_{\text{max}} = (6.7 \pm 0.3) \times 10^7 \text{ M}^{-1}\text{s}^{-1}$ and $(\text{pK}_a)_{\text{ZnH}_2\text{O}} = 6.7 \pm 0.1$ (see also Table 1). (b) pH profile for the proton transfer dependent rate constant $R_{\text{H}_2\text{O}}/[E]$ (s^{-1}) in catalysis by AaCA1 as determined by ^{18}O -exchange methods. The solid line is a fit to eq 6-6 with $k_B = (1.1 \pm 0.2) \times 10^6 \text{ s}^{-1}$ and $(\text{pK}_a)_{\text{donor}} = 6.5 \pm 0.2$ and $(\text{pK}_a)_{\text{ZnH}_2\text{O}} = 6.5 \pm 0.2$ (see also Table 1).

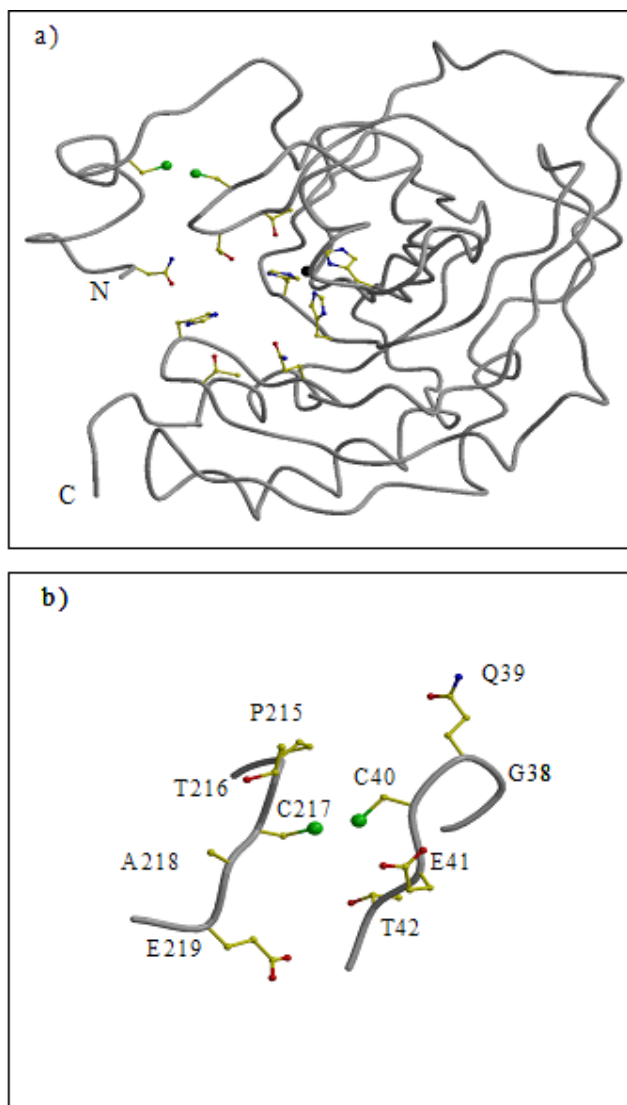


Figure 6-4. Molecular model of AaCA1. (a) Grey coil of overall structure of AaCA1, with active site residues in yellow ball-and-stick, and catalytic zinc atom depicted as a black sphere. N and C termini are as marked; (b) The putative disulfide bond of AaCA1 between residues Cys 40 and 217. Figure was generated and rendered with BobScript and Raster3D (Esnouf, 1997; Merritt and Bacon, 1997).

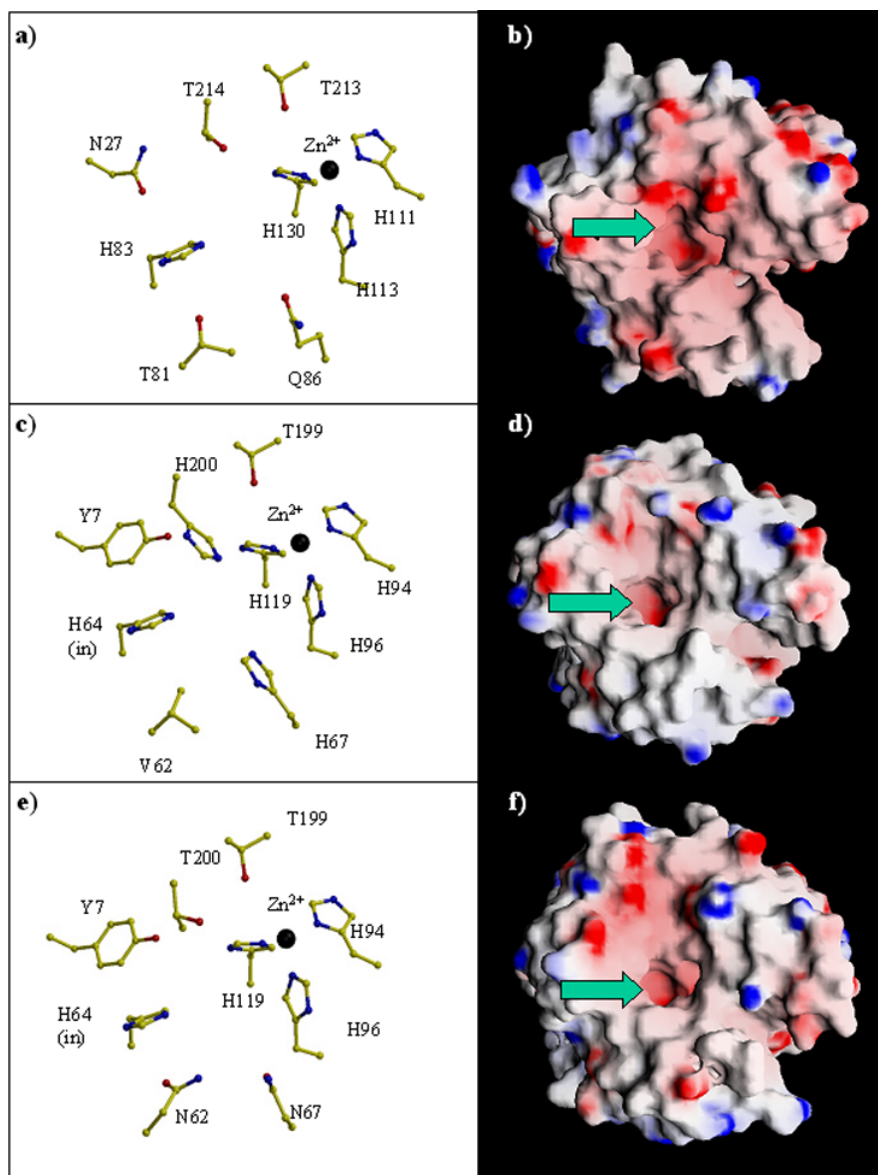


Figure 6-5. Active sites and surface charge distribution of AaCA1, HCA I, and HCA II. (a), (c), and (e) Active sites of AaCA1, HCA I, and HCA II, respectively. (b), (d), and (f) Molecular surface with charge distribution, where blue represents positive and red the negative charge of AaCA1, HCA I, and HCA II, respectively. The green arrows point to the active site of each isoform. Figures (a), (c), and (e) were generated and rendered with BobScript and Raster3D, respectively (Esnouf, 1997; Merritt and Bacon, 1997). Figures (b), (d), and (f) were made using GRASP (Nicholls *et al.*, 1991).

CHAPTER 7 CONCLUSIONS AND FUTURE DIRECTIONS

Summary and Conclusions

The main focus of this dissertation, as discussed in Chapters 2 to 6, has been to gain insights into active site structure of various CAs and relate this knowledge to proton transfer as catalyzed by CA. Different approaches towards these ends were taken to assist in the investigation of structural features as they affect enzyme function.

In Chapter 2, the proton shuttling histidine residues were inserted at different positions in the active site of HCA II. The effect on solvent structure and proton transfer kinetics was then determined over a broad pH range for wild type and mutant HCA II (pH 5.1 to 10.0). A striking feature of HCA II is that it shows remarkable structural and kinetic stability over a wide range of pH (5.1 to 10.0). The main structural difference is the orientation of His64 in wild type HCA II. The side chain displays two conformations and these two states appear to be equally occupied at physiological pH. In H64A/N62H and H64A/N67H HCA II the introduced His does not show any mobility and there is no completed hydrogen-bonded water chain between proton donor and acceptor. A His inserted at position 67 shows appreciable proton shuttling activity (25% of wild type), compared to a His at position 62 (4% of wild type). In these examples, the distance between the proton shuttling His and the zinc-bound solvent and the number of waters that spans this distance, might be more important for efficient proton shuttling than observing a complete hydrogen-bonded chain of waters to the His residue. The results suggest that the optimal distance for the His to the zinc is between 6.6 and 7.5 Å and that

the number of intervening water molecules should not exceed two for the support of efficient and fast proton transfer.

In Chapter 3 three key active site residues in HCA II (Tyr7, Asn62, and Asn67) were replaced by hydrophobic Phe and Leu residues. The rationale was to remove any polar groups while at the same time avoiding steric problems and then measuring the effect on active site solvation and catalysis by HCA II. Instead of directly altering the proton shuttle His64, the goal was to specifically affect the hydrogen-bonded water structure. The structural and kinetic data for N62L and N67L mutants show that the water networks were easily disrupted, especially at low pH, and both displayed considerable lower proton transfer rates compared to wild type and Y7F HCA II. The most surprising result was the enhanced proton transfer rate (up to 7-fold higher) over that of wild type observed for Y7F HCA II. This mutant also displayed a similar water network as wild type HCA II, except for the loss of one active site water. A surprising observation was that Y7F had a sulfate bound at pH 8.2 as this is very unexpected and usually only occurs at low pH (Fisher *et al.*, 2005). Due to the presence of sulfate in the crystal structure and the uncertainty of the effect this has on the orientation of His64 and water structure, the protein was crystallized in the absence of any ammonium sulfate. Comparing the structures of all three mutants, determined at various pH and in the presence or absence of sulfate, strongly suggests that sulfate does not affect the conformation of His64 or the water structure. Correlations between the structural and kinetic data suggest that a single, linear array of water bridging His64 and the zinc-bound solvent might be more efficient at proton transfer than a branched structure. Also, these mutations caused changes in the

pK_a of the proton donor and acceptor and the difference in the pK_a could also have an effect on proton transfer efficiency.

Chapter 4 describes some initial work done towards obtaining a neutron structure of HCA II. X-ray crystallography is severely limited in its ability to reveal the locations of hydrogen or deuterium (H/D) atoms. This is because the extent of diffraction by X-rays depends on the number of electrons and H/D atoms diffract poorly compared to more electron-rich atoms such as carbon C and nitrogen N. Neutrons interact with nuclei of atoms and the diffraction of these atoms, including H/D, does not depend on the number of electrons at all (Habash *et al.*, 2000; Langan *et al.*, 2004). Neutron crystallography can provide information about ionization of catalytic residues, water molecules, and the positions of H/D atoms. The benefits and information obtainable by using neutrons versus X-rays can really assist in the detailed analysis of the CA active site. To this end, fully deuterated enzyme was produced, crystallized, and the structure determined to 1.50 Å (Budayova-Spano *et al.*, 2006). To show proof-of-principle that the deuterated enzyme is homologous to its hydrogenated counterpart, the X-ray structure and catalytic rate of perdeuterated HCA II was determined. The structure and kinetic measurements revealed that perdeuterated HCA II was, within error, identical to hydrogenated HCA II. The only difference was an expected isotope effect in the proton transfer component of catalysis.

Chapter 5 describes a more applied approach compared to the fundamental questions being asked in the preceding chapters. Here X-ray crystallography was used to investigate the binding modes of novel, spacer-containing inhibitors to HCA II, BB3 and TDM. CA inhibitors (CAIs) are commonly prescribed for the treatment of glaucoma,

altitude sickness, and epilepsy (Maren, 1987). The classical, clinically available CAIs have very poor solubility and subsequent bioavailability. Novel compounds with better solubility and different chemical properties could have new applications. Specifically, there is significant interest in using CAIs against certain tumor types as the overexpression of HCA IX is strongly associated with some solid tumors (Wykoff *et al.*, 2000; Giatromanolaki *et al.*, 2001). The work described in this chapter involves two new water-soluble compounds that employ the classical sulfonamide group but have an additional spacer group between the sulfonamide and aromatic ring groups. Structure determination of these compounds bound to HCA II reveal that the spacer group confers interesting and novel binding modes to HCA II (Fisher *et al.*, 2006). These alternated binding modes and locations in the active site could be useful for the future development of human isoform specific drugs.

The recent discovery and cloning of an α -class CA from the mosquito larvae of *Aedes aegypti* (AaCA1) presents an interesting and new target for the possible control of mosquito populations (Del Pilar Corena *et al.*, 2002). Chapter 6 illustrates the expression, purification, and subsequent kinetic and structural characterization of AaCA1. The homology model indicates that this protein is an α -CA and inhibition of the enzyme with clinically used sulfonamides, methazolamide and acetazolamide, supports this conclusion. Catalytic rate measurements also revealed that AaCA1 is a high activity isoform that displays similar proton transfer kinetics to HCA II. However, the rate constant for CO₂/bicarbonate interconversion is more closely resembles that of HCA I. This is interesting as AaCA1 shows higher sequence identity with HCA I compare to HCA II (39% and 32%). The homology model of AaCA1 provides some rationale for the

observed differences in the enzyme activity. Critical active site residues found in HCA II are conserved in AaCA1, specifically Thr214 and other polar amino acids that line the active site cavity. In contrast, HCA I has a His at position 214 and other hydrophobic residues in the active site. Other residues of interest are Thr81 and Gln86 in AaCA1 (Val62 and His67 in HCA I, and Asn62 and Asn67 in HCA II) that could be exploited for the design of selective CAIs to AaCA1.

Future Directions

Despite the abundance of information available about CA activity and active site structure, there are still many unanswered questions. It is unclear which active site residues directly participate in hydrogen bond interactions with water molecules and which are hydrogen bond donors and acceptors involved in proton transfer. These questions would best be answered by a combination of ultra-high resolution X-ray and medium resolution neutron crystallography studies. There are several high resolution crystal structures on hand but these have been determined in complex with either inhibitors or activators (Duda *et al.*, 2003; Jude *et al.*, 2006). Recently, X-ray diffraction data to 1.05 Å of wild type HCA II, without any inhibitors or activators present, was obtained and the structure determination and analysis is currently underway. These data should give valuable information on the protonation status of the proton shuttle His64 as well the possible identity of the zinc-bound solvent. Beam time on the ILL (Grenoble, France) neutron source has also been secured and it is anticipated that the large, perdeuterated crystals of HCA II will at least diffract. Results from the complementary neutron and X-ray techniques could provide high resolution and specific active site information. Not only with these studies contribute an enormous amount of information to our current understanding of the CA active site and catalysis, the information can also

be used to understand differences between human isoforms. Also, details of the protonation state of the HCA II active site will be useful for applications such as rational drug design.

LIST OF REFERENCES

- Alber B.E., Ferry J.G. (1996), Characterization of heterologously produced carbonic anhydrase from *Methanosarcina thermophila*, *J. Bacteriol.* **178**, 3270-3274.
- An H., Tu C.K., Duda D.M., Montanez-Clemente I., Math K., Laipis P.J., McKenna R., Silverman D.N. (2002), Chemical rescue in catalysis by human carbonic anhydrases II and III, *Biochem.* **41**, 3235-3242.
- Aronsson G., Mårtensson L.G., Carlsson U., Jonsson B.H. (1995), Folding and stability of the N-terminus of human carbonic anhydrase II, *Biochem.* **34**, 2153-2162.
- Bergenheim N.C.H., Hallberg M., Wisen S. (1998), Molecular characterization of the human carbonic-anhydrase-related protein (HCA-RP VIII), *Biochimica et Biophys. Acta* **1384**, 294-298.
- Bertini I., Canti G., Luchinat C., Borghi E. (1983), Investigation of the system copper(II) carbonic anhydrase and $\text{HCO}_3^-/\text{CO}_2$, *J. Inorgan. Biochem.* **18**, 221-229.
- Bhatt D., Tu C.K., Fisher S.Z., Hernandez-Prada J.A., McKenna R., Silverman, D.N. (2005), Proton transfer from His200 in human carbonic anhydrase II, *Proteins: Structure, Function, and Bioinformatics* **61**, 239-245.
- Boyle N.A., Chegwiddden W.R., Blackburn G.M. (2005), A new synthesis of difluoromethanesulfonamides: A novel pharmacophore for carbonic anhydrase inhibition, *Org. Biomol. Chem.* **3**, 222-224.
- Breton S. (2001), The cellular physiology of carbonic anhydrases, *J. Pancreas* **2**, 159-164.
- Brockwell D., Yu L., Cooper S., McClelland S., Cooper A., Attwood D., Gaskell S.J., Barber J. (2001), Physicochemical consequences of the perdeuteration of glutathione S-transferase from *S. japonicum*, *Protein Sci.* **10**, 572-580.
- Brünger A.T., Adams P.D., Clore G.M., DeLano W.L., Gros P., Grosse-Kuntze R.W., Jiang J.S., Kuszewski J., Nilges M., Pannu N.S., Read R.J., Rice L.M., Simonson T., Warren G.L. (1998), Crystallography & NMR system: A new software suite for macromolecular structure determination, *Acta Crystallogr.* **D54**, 905-921.

- Budayova-Spano M., Fisher S.Z., Dauvergne M.T., Agbandje-McKenna M., Silverman D.N., Myles D.A.A., McKenna R. (2006), Production and X-ray crystallographic analysis of fully deuterated human carbonic anhydrase II, *Acta Crystallogr.* **F62**, 6-9.
- Burnell J.N. (2000), Carbonic anhydrases in higher plants in: Chegwiddden WR, Carter ND, Edwards YH (Eds), *The Carbonic Anhydrases*, New Horizons; Birkhauser Verlag, Basel, Switzerland, 501-518.
- Chakravarty S., Kannan K.K. (1994), Drug-protein interactions: Refined structures of three sulfonamide drug complexes of human carbonic anhydrase I enzyme, *J. Mol. Biol.* **243**, 298-309.
- Chegwiddden W.R. and Carter N.D. (2000), Introduction to the carbonic anhydrases in: Chegwiddden WR, Carter ND, Edwards YH (Eds), *The Carbonic Anhydrases*, New Horizons; Birkhauser Verlag, Basel, Switzerland, 13-28.
- Christianson D.W., Fierke C.A. (1996), Carbonic Anhydrase: Evolution of the zinc binding site by nature and design, *Acc. Chem. Res.* **29**, 331-339.
- Coates L., Erskine P.T., Wood S.P., Myles D.A.A., Cooper J.B. (2001), A neutron Laue diffraction study of endothiapepsin: Implications for the aspartic protease mechanism, *Biochem.* **40**, 13149-13157.
- Coleman J.E. (1967), Mechanism of action of carbonic anhydrase. Substrate, sulfonamide, and anion binding, *J. Biol. Chem.* **242**, 5212-5219.
- Cui Q., Karplus M. (2003), Is a "proton wire" concerted or stepwise? A model study of proton transfer in carbonic anhydrase, *J. Phys Chem. B* **107**, 1071-1078.
- Darsie R.F., Ward R.A. (2000), Summary of new distribution records for mosquito species in the United States and Canada for the period 1982-99, *J. Am. Mosq. Control Assoc.* **16**, 1-4.
- Del Pilar Corena M., Seron T.J., Lehman H.K., Ochrietor J.D., Kohn A., Tu C.K., Linser P.J. (2002), Carbonic anhydrase in the midgut of larval *Aedes aegypti*: Cloning, localization, and inhibition, *J. Exp. Biol.* **205**, 591-602.
- Del Pilar Corena M., Fiedler M.M., Van Ekeris L., Linser P.J. (2004), A comparative study of carbonic anhydrase in the midgut of mosquito larvae, *Comp. Biochem. Physiol.* **137**, 207-225.
- Dodgson S.J. (1991), The carbonic anhydrases: Cellular physiology and molecular genetics: Dodgson S.J., Tashian R.E., Gros G., Carter N.D. (Eds), Plenum, New York, 267-305.

- Duda D., McKenna R. (2004), Carbonic anhydrase (α -class) in: Messerschmidt A., Bode W., Cygler M. (Eds.) Handbook of Metalloproteins, John Wiley & Sons, New York, 249-263.
- Duda D.M., Tu C.K., Qian M., Laipis P.J., Agbandje-McKenna M., Silverman D.N., McKenna R. (2001), Structural and kinetic analysis of the chemical rescue of the proton transfer function of carbonic anhydrase II, *Biochemistry* **40**, 1741-1748.
- Duda D.M., Govindasamy L., Agbandje-McKenna M., Tu C.K., Silverman D.N., McKenna R. (2003), The refined atomic structure of carbonic anhydrase II at 1.05Å resolution: Implications of chemical rescue of proton transfer, *Acta Crystallogr.* **D59**, 93-104.
- Earnhardt J.N., Silverman D.N. (1998), Carbonic anhydrase in: Sinnott M.(Ed.) Comprehensive biological catalysis Volume 1, Academic Press, London, 483–495.
- Eigen M. (1964), Proton transfer, acid-base catalysis, and enzymatic hydrolysis, *Angewandte Chemie* **3**, 1-19.
- Emsley P., Cowtan K. (2004), Coot: Model-building tools for molecular graphics, *Acta Crystallogr.* **D60**, 2126-2132.
- Engh R.A., Huber R. (1991), Accurate bond and angle parameters for X-ray protein structure refinement, *Acta Cryst.* **A47**, 392-400.
- Eriksson A.E., Jones T.A., Liljas A. (1988), Refined structure of human carbonic anhydrase II at 2.0 Å resolution, *Proteins* **4**, 274-282.
- Esnouf R.M. (1997), An extensively modified version of MolScript that includes greatly enhanced coloring capabilities, *J Mol Graph Model.* **15**, 132-134 and 112-113.
- Fisher Z., Hernandez Prada J.A., Tu C.K., Duda D., Yoshioka C., An H., Govindasamy L., Silverman D.N., McKenna R. (2005) Structural and kinetic characterization of active site histidine as a proton shuttle in catalysis by human carbonic anhydrase II, *Biochem.* **44**, 1097-1105.
- Fisher S.Z., Govindasamy L., Boyle N., Agbanje-McKenna M., Silverman D.N., Blackburn G.M., McKenna R. (2006), X-ray crystallographic studies reveal that the incorporation of spacer groups in carbonic anhydrase inhibitors cause alternate binding modes, *Acta Crystallogr.* **F62**, 618-622.
- Forster R.E. (2000), Remarks on the discovery of carbonic anhydrase in: Chegwidde WR, Carter ND, Edwards YH (Eds.), The Carbonic Anhydrases, New Horizons; Birkhauser Verlag Basel, Switzerland, 1-11.
- Fraser C.M., Gocayne J.D., White O., Adams M.D., Clayton R.A., Fleischmann R.D., Bult C.J., Kerlavage A.R., Sutton G.G., Kelley J.M. *et al.* (1995), The minimal gene complement of *Mycoplasma genitalium*, *Science* **270**, 397-403.

- Fujikawa-Adachi K., Nishimori I., Taguchi T., Onishi S. (1999), Human carbonic anhydrase XIV (CA14): cDNA cloning, mRNA expression, and mapping to chromosome 1, *Genomics* **61**, 74-81.
- Giatromanolaki A., Koukourakis M.I., Sivridis E., Pastorek J., Wykoff C.C., Gatter K.C., Harris A.L. (2001), Expression of hypoxia-inducible carbonic anhydrase-9 relates to angiogenic pathways and independently to poor outcome in non-small cell lung cancer, *Cancer Res.* **61**, 7992-7998.
- Gubler D.J. (1997), Dengue and dengue hemorrhagic fever. Its history and resurgence as a global health problem, in Gubler D.J. and Kuno G. (Eds.) *Dengue and Dengue Hemorrhagic Fever*. CAB International, Wallingford, United Kingdom, 1-22.
- Guex N., Diemand A., Peitsch M.C. (1999), Protein modeling for all, *TIBS* **24**, 364-367.
- Guillot M.B., Korte J.J., Lamblin A.F., Fuchs J.A., Anderson P.M. (1992), Carbonic anhydrase in *Eschericia coli*: A product of the *cyn* operon, *J. Biol. Chem.* **267**, 3731-3734.
- Habash J., Raftery J., Weisgerber S., Cassetta A., Lehmann M.S., Høghøj P., Wilkinson C., Campbell J.W., Helliwell J.R. (1997), Neutron Laue diffraction study of concanavalin A: The proton of Asp28, *J. Chem. Soc Faraday Trans.* **93**, 4313-4317.
- Habash J., Raftery J., Nuttall R., Price H.J., Wilkinson C., Kalb A.J., Helliwell J.R. (2000), Direct determination of the position of the deuterium atoms of the bound water in concanavalin A by neutron Laue crystallography, *Acta Cryst.* **D65**, 541-550.
- Håkansson K., Carlsson M., Svensson L.A., Liljas A. (1992), Structure of native and apo carbonic anhydrase II and structure of some of its anion-ligand complexes, *J. Mol. Biol.* **227**, 1192-1204.
- Halstead S.B. (1997), Epidemiology of dengue and dengue hemorrhagic fever, in Gubler D.J. and Kuno G. (Eds.) *Dengue and Dengue Hemorrhagic Fever*. CAB International, Wallingford, United Kingdom, 23-44.
- Henriques O.M. (1928), Die bindungsweise des kohlendioxids im blute, *Biochem. Ztschrift* **200**, 1-24.
- Henry R.P. (1996), Multiple roles of carbonic anhydrase in cellular transport and metabolism, *Annu. Rev. Physiol.* **58**, 523-538.
- Hewett-Emmett D., Tashian R.E. (1996), Functional diversity, conservation, and convergence in the evolution of the alpha-, beta-, and gamma-carbonic anhydrase gene families, *Mol. Phylogen. Evo.* **5**, 50-77.

- Iverson T.M., Alber B.E., Kisker C., Ferry J.G., Rees D.C. (2000), A closer look at the active site of gamma-class carbonic high-resolution crystallographic studies of the carbonic anhydrase from *Methanosarcina thermophila*, *Biochem.* **39**, 9222-9231.
- Jewell D.A., Tu C.K., Paranawithana S.R., Tanhauser S.M., LoGrasso P.V., Laipis P.J., Silverman D.N. (1991), Enhancement of the catalytic properties of human carbonic anhydrase III by site-directed mutagenesis, *Biochem.* **30**, 1484-1490.
- Jones T.A., Zou J.Y., Cowan S.W., Kjeldgaard M. (1991), Improved methods for building protein models in electron density maps and the location of errors in these models, *Acta Crystallogr.* **A47**, 110-119.
- Jonsson B.M., Hakansson K., Liljas A. (1993), The structure of human carbonic anhydrase II in complex with bromide and azide. *FEBS Lett.* **322**, 186-190.
- Jude K.M., Wright S.K., Tu C.K., Silverman D.N., Viola R.E., Christianson D.W. (2002), Crystal structure of F65A/Y131C-methylimidazole carbonic anhydrase V reveals architectural features of an engineered proton shuttle, *Biochem.* **41**, 2485-2491.
- Jude K.M., Banerjee A.L., Haldar M.K., Manokaran S., Roy B., Mallik S., Srivastava D.K., Christianson D.W. (2006), Ultrahigh resolution crystal structures of human carbonic anhydrase I and II complexed with "two-prong" reveal the molecular basis of high affinity, *J. Am. Chem. Soc.* **128**, 3011-3018.
- Kato K. (1990), Sequence of a novel carbonic anhydrase-related polypeptide and its exclusive presence in the Purkinje cells, *FEBS Letters* **271**, 137-140.
- Kannan K.K., Notstrand B., Fridborg K., Lövgren S., Ohlsson A., Petef M. (1975), Crystal structure of human erythrocyte carbonic anhydrase B. Three-dimensional structure at a nominal 2.2-Å resolution, *PNAS* **72**, 51-55.
- Kannan K.K., Petef M., Fridborg K., Cid-Dresdner H., Lovgren S. (1977), Structure and function of carbonic anhydrases. Imidazole binding to human carbonic anhydrase B and the mechanism of action of carbonic anhydrases, *FEBS Let.* **73**, 115-119.
- Khalifah R.G. (1971), The carbon dioxide hydration activity of carbonic anhydrase. I. Stop-flow kinetic studies on the native human isoenzymes B and C, *J. Biol. Chem.* **246**, 2561-2573.
- Khalifah R.G., Strader D.J., Bryant S.H., Gibson S.M. (1977), Carbon-13 nuclear magnetic resonance probe of active-site ionizations in human carbonic anhydrase B, *Biochemistry* **16**, 2241-2247.
- Kim G., Lee T.H., Wetzel P., Geers C., Robinson M.A., Myers T.G., Owens J.W., Wehr N.B., Eckhaus M.W., Gros G., Wynshaw-Boris A., Levine R.L. (2004), Carbonic anhydrase III is not required in the mouse for normal growth, development, and life span, *Mol Cell Biol.* **24**, 9942-9947.

- Kim S., Rabbani Z., Dewhirst M., Vujaskovic Z., Vollmer R., Schreiber E., Oosterwijk E., Kelley M. (2005), Expression of HIF-1 α , CA IX, VEGF, and MMP-9 in surgically resected non-small cell lung cancer, *Lung Cancer* **49**, 325-335.
- Kisker C., Schindelin H., Alber B.E., Ferry J.G., Rees D.C. (1996), A left-hand beta-helix revealed by the crystal structure of a carbonic anhydrase from the archaeon *Methanosarcina thermophila*, *EMBO J.* **15**, 2323-2330.
- Krebs J.F., Fierke C.A. (1991), Conformational mobility of His64 in the Thr200 \rightarrow Ser mutant of human carbonic anhydrase II, *Biochem.* **30**, 9153-9160.
- Krebs J.F., Rana F., Dluhy R.A., Fierke C.A. (1993), Kinetic and spectroscopic studies of hydrophilic amino acid substitutions in the hydrophobic pocket of human carbonic anhydrase II, *Biochem.* **32**, 4496-4505.
- Kresge J.A., Silverman D.N. (1999), Application of Marcus rate theory to proton transfer in enzyme-catalyzed reactions, *Methods Enzym.* **308**, 276-297.
- Langan P., Greene G., Schoenborn B.P. (2004), Protein crystallography with spallation neutrons: the user facility at Los Alamos Neutron Science Center, *J. Appl. Cryst.* **37**, 24-31.
- Laskowski R.A., MacArthur M.W., Moss D.S., Thornton J.M. (1993), PROCHECK: A program to check the stereochemical quality of protein structures, *J. Appl. Cryst.* **26**, 283-291.
- Lehtonen J., Shen B., Vihinen M., Casini A., Scozzafava A., Supuran C.T., Parkkila A.K., Saarnio J., Kivela A.J., Waheed A., Sly W.S., Parkkila S.J. (2004), Characterization of CA XIII, a novel member of the carbonic anhydrase isozyme family, *J. Biol Chem.* **279**, 2719-2727.
- Liang Z., Xue Y., Behravan G., Jonsson B.H., Lindskog S. (1993), Importance of the conserved active-site residues Tyr7, Glu106 and Thr199 for the catalytic function of human carbonic anhydrase II, *Eur J Biochem.* **211**, 821-827.
- Liang J.Y., Lipscomb W.N. (1990), Binding of substrate CO₂ to the active site of human carbonic anhydrase II: A molecular dynamics study, *PNAS* **87**, 3675-3679.
- Liang Z., Jonsson B.H., Lindskog S. (1993), Proton transfer in the catalytic mechanism of carbonic anhydrase. Effects of placing histidine residues at various positions in the active site of human isozyme II, *Biochim. Biophys. Acta* **1203**, 142-146.
- Liljas A., Kannan K.K., Bergstén P.C., Waara I., Fridborg K., Strandberg B., Carlbom U., Järup L., Lövgren S., Petef M. (1972), Crystal structure of human carbonic anhydrase C, *Nature New Biol.* **235**, 131-137.
- Liljas A., Håkansson K., Jonsson B.H., Lindskog S. (1994), Inhibition and catalysis of carbonic anhydrase. Recent crystallographic analyses, *Eur. J. Biochem.* **219**, 1-10.

- Lindskog S. (1997), Structure and mechanism of carbonic anhydrase, *Pharmacol. Ther.* **74**, 1-20.
- Lindskog S., Silverman D.N. (2000), The catalytic mechanism of mammalian carbonic anhydrases in: Chegwiddden W.R., Carter N.D., Edwards Y.H. (Eds.), *The Carbonic Anhydrases*, New Horizons; Birkhauser Verlag Basel, Switzerland, 175-195.
- LoGrasso P.V., Tu C.K., Jewell D.A., Wynns G.C., Laipis P.J., Silverman D.N. (1991), Catalytic enhancement of human carbonic anhydrase III by replacement of phenylalanine-198 with leucine, *Biochem.* **30**, 8463-8470.
- Mann T., Keilin D. (1940), Sulfanilamide as a specific inhibitor of carbonic anhydrase, *Nature* **146**, 164-165.
- Mansoor U.F., Zhang X.R., Blackburn G.M. (2000), The design of new carbonic anhydrase inhibitors in: Chegwiddden W.R., Carter N.D., Edwards Y.H. (Eds.), *The Carbonic Anhydrases*, New Horizons; Birkhauser Verlag Basel, Switzerland, 437-459.
- Maren T.H. (1967), Carbonic anhydrase: Chemistry, physiology, and inhibition, *Physiol. Rev.* **47**, 595-781.
- Maren T.H. (1974), HCO₃⁻ formation in aqueous humour. Mechanism and relation to the treatment of glaucoma, *Invest. Ophthalmol.* **13**, 479-484.
- Maren T.H. (1987), Carbonic anhydrase: general perspectives and advances in glaucoma research. *Drug Dev. Res.* **10**, 255-276.
- Maren T.H., Conroy C.W. (1993), A new class of carbonic anhydrase inhibitor, *J. Biol. Chem.* **268**, 26233-26239.
- Maren T.H., Sanyal G. (1983), The activity of sulfonamides and anions against the carbonic anhydrases of animals, plants, and bacteria, *Ann. Rev. Pharmacol. Toxicol.* **23**, 439-459.
- Martin M.M., Martin J.S., Kukor J.J., Merrit R.W. (1980), The digestion of protein and carbohydrate by the stream detritivore, *Tipula abdominalis* (Diptera, Tipulidae), *Oecologia* **46**, 360-364.
- Marx D., Tuckerman M.E., Hutter J., Parrinello M. (1999), The nature of the hydrated excess proton in water, *Nature* **397**, 601-604.
- McPherson A. (1982), *Preparation and Analysis of Protein Crystals*, Wiley, New York.
- Meilleur F., Contzen J., Myles D.A.A., Jung C. (2004), Structural stability and dynamics of hydrogenated and perdeuterated cytochrome P450cam (CYP101), *Biochem.* **43**, 8744-8753.

- Meldrum N.U., Roughton F.J.W. (1932), Some properties of carbonic anhydrase, the CO₂-enzyme present in blood, *J. Physiol. (London)* **75**, 15-16.
- Meldrum N.U., Roughton F.J.W. (1933), Carbonic anhydrase: Its preparation and properties, *J. Physiol. (London)* **80**, 113-142.
- Merritt E.A., Bacon D.J. (1997), Raster3D Version 2: Photorealistic molecular graphics, *Methods of Enzymology* **277**, 505-524.
- Merz K.M. (1990), Insights into the function of the zinc hydroxide-Thr199-Glu106 hydrogen bonding network in carbonic anhydrases, *J Mol Biol.* **214**, 799-802.
- Merz K.M. (1991), Carbon dioxide binding to human carbonic anhydrase II, *J. Am. Chem. Soc.* **113**, 406-411.
- Mitsuhashi S., Mizushima T., Yamashita E., Yamamoto M., Kumasaka T., Moriyama H., Ueki T., Miyachi S., Tsukihara T. (2000), X-ray structure of beta-carbonic anhydrase from the red alga, *Porphyridium purpureum*, reveals a novel catalytic site for CO(2) hydration, *J. Biol. Chem.* **275**, 5521-5526.
- Mohammed O.F., Pines D., Dreyer J., Pines E., Nibbering E.T.J (2005), Sequential proton transfer through water bridge in acid-base reactions, *Science* **310**, 83-86.
- Murakami H., Sly W.S. (1987), Purification and characterization of human salivary carbonic anhydrase, *J. Biol. Chem.* **262**, 1382-1388.
- Murakami Y., Kanada K., Tsuji M., Kanayama H., Kagawa S. (1999), MN/CA9 gene expression as a potential biomarker in renal cell carcinoma, *BJU Int.* **83**, 743-747.
- Myles D.A.A., Bon C., Langan P., Cipriani F., Castagna J.C., Lehmann M.S., Wilkinson C. (1998), Neutron Laue diffraction in macromolecular crystallography, *Physica B* **241-243**, 1122-1130.
- Nagle J.F., Morowitz H.J. (1978), Molecular mechanisms of proton transport in membranes, *PNAS* **75**, 298-302.
- Nair S.K., Christianson D.W. (1991), Unexpected pH-dependent conformation of His-64, the proton shuttle of carbonic anhydrase II, *J. Am. Chem. Soc.* **113**, 9455-9458.
- Nair S.K., Ludwig P.A., Christianson D.W. (1994), Two-Site Binding of phenol in the active site of human carbonic anhydrase II: Structural implications for substrate association, *J. Am. Chem. Soc.* **116**, 3659-3660.
- Nair S.K., Krebs J.F., Christianson D.W., Fierke C.A. (1995), Structural basis of inhibitor affinity to variants of human carbonic anhydrase II, *Biochem.* **34**, 3981-3989.

- Nicholls A., Sharp K., Honig B. (1991), Protein folding and association: Insights from the interfacial and thermodynamic properties of hydrocarbons, *Proteins* **11**, 281-296.
- Niimura N. (1999), Neutrons expand the field of structural biology, *Curr. Opin. Struct. Biol.* **9**, 602-608.
- Niimura N., Arai S., Kurihara K., Chatake T., Tanaka I., Bau R. (2006), Recent results on hydrogen and hydration in biology studies by neutron macromolecular crystallography, *Cell. Mol. Life Sci.* **63**, 285-300.
- Norvell J.C., Nunes A.C., Schoenborn B.P. (1975), Neutron diffraction analysis of myoglobin: Structure of the carbon monoxide derivative, *Science* **190**, 568-569.
- Ortova Gut M., Parkkila S., Vernerová Z.K., Rohde E., Závada J., Hocker M., Pastorek J., Karttunen T., Gibadulinová A., Zavadová Z., Knobeloch K.P., Wiedenmann B., Svoboda J., Horak I., Pastorekova S. (2002), Gastric hyperplasia in mice with targeted disruption of the carbonic anhydrase gene *Car9*, *Gastroenterol.* **123**, 1889-1903.
- Osborne W.R.A., Tashian R.E. (1974), Thermal inactivation studies of normal and variant human erythrocyte carbonic anhydrases by using a sulphonamide-binding assay, *Biochem. J.* **141**, 219-225
- Otwinowski Z., Minor W. (1997), Processing of X-ray diffraction data collected in oscillation mode, *Methods Enzymol.* **276**, 307-326.
- Pastoreková S., Zavadová Z., Košťál M., Babušíková O., Závada J. (1992), A novel quasi-viral agent, Ma-Tu, is a two-component system, *Virology* **187**, 620-626.
- Peitsch M.C. (1996), Promod and Swiss-Model: Internet-based tools for automated comparative protein modeling, *Biochem. Soc. Trans.* **24**, 372-279.
- Pines E., Magnes E.Z., Lang M.J., Fleming G.R. (1997), Direct measurement of intrinsic proton transfer rates in diffusion-controlled reactions, *Chem. Phys. Letters* **281**, 413-420.
- Pomès R., Roux B. (1996), Theoretical study of H⁺ translocation along a model proton wire, *J. Phys. Chem.* **100**, 2519-2527.
- Rossmann M.G. (1990), The molecular replacement method, *Acta Cryst.* **A46**, 73-82.
- Rowlett R.S., Silverman D.N. (1982), Kinetics of the protonation of buffer and hydration of CO₂ catalyzed by human carbonic anhydrase II, *J. Am. Chem. Soc.* **104**, 6737-6741.
- Sanyal G., Swenson E.R., Pessah N.I., Maren T.H. (1982), The carbon dioxide hydration activity of skeletal muscle carbonic anhydrase, *Mol. Pharmacol.* **22**, 211-220.

- Scheiner S., Yi M. (1996), Proton transfer properties of imidazole, *J. Phys. Chem.* **100**, 9235-9241.
- Schultz A.J., Thiyagarajan P., Hodges J.P., Rehm C., Myles D.A.A., Langan P., Mesecar A. (2005), Conceptual design of a macromolecular neutron diffractometer (MaNDi) for the SNS, *J. Appl. Cryst.* **38**, 964-974.
- Schwede T., Kopp J., Guex N., Peitsch M.C. (2003), Swiss-Model: An automated protein homology-modeling server, *Nucleic Acids Research* **31**, 3381-3385.
- Segal I.H. (1975), *Enzyme kinetics*, Wiley-Interscience, New York, 150-159.
- Seron T.J., Hill J., Linser P.J. (2004), A GPI-linked carbonic anhydrase expressed in the larval mosquito midgut, *J. Exp. Biol.* **207**, 4559-4572.
- Shah G.U., Ulmasov B., Waheed A., Becker T., Makani S., Svichar N., Chesler M., Sly W.S. (2005), Carbonic anhydrase IV and XIV knock-out mice: Roles of the respective carbonic anhydrases in buffering the extracellular space in brain, *PNAS* **102**, 16771-16776.
- Sheldrick G.M., Schneider T.R. (1997), *Macromolecular Crystallography, Part B*, Sweet R.M. and Carter C.W. Jr. (Eds.), *Methods Enzymol.* **277**, 319-343.
- Shu F., Ramakrishnan V., Schoenborn B.P. (2000), Enhanced visibility of hydrogen atoms by neutron crystallography of fully deuterated myoglobin, *Proc. Natl. Acad. Sci. USA* **97**, 3872-3877.
- Schüttelkopf A.W., van Aalten D.M.F. (2004), PRODRG: A tool for high-throughput crystallography of protein-ligand complexes, *Acta Cryst.* **D60**, 1355-1363.
- Silverman D.N. (1982), Carbonic anhydrase: Oxygen-18 exchange catalyzed by an enzyme with rate-contributing steps, *Methods Enzymol.* **87**, 732-752
- Silverman D.N. (2000), Marcus rate theory applied to enzymatic proton transfer, *Biochimica Biophys. Acta* **1458**, 88-103.
- Silverman D.N., Tu C.K., Lindskog S., Wynns G.C. (1979), Rate of exchange of water from the active site of human carbonic anhydrase C, *J. Am. Chem. Soc.* **101**, 6734 – 6740.
- Silverman D.N., Tu C.K., Chen X., Tanhauser S.M., Kresge A.J., Laipis P.J. (1993), Rate-equilibria relationships in intramolecular proton transfer in human carbonic anhydrase III, *Biochemistry* **32**, 10757-10762.
- Silverman D.N., Lindskog S. (1988), The catalytic mechanism of carbonic anhydrase: Implications of a rate-limiting protolysis of water, *Acc. Chem. Res.* **21**, 30-36.

- Simonsson .I., Lindskog S. (1982), The interaction of sulfate with carbonic anhydrase, *Eur. J. Biochem.* **123**, 29-36.
- Skaggs L.H., Bergenhem N.C.H., Venta P.J., Tashian R.E. (1993) The deduced amino acid sequence of human carbonic anhydrase-related protein (CARP) is 98% identical to the mouse homologue, *Gene* **126**, 291-292.
- Sly W.S., Hu P.Y. (1995), Human carbonic anhydrases and carbonic anhydrase deficiencies, *Annu. Rev. Biochem.* **64**, 375-401.
- So A.K.C., Espie G.S., Williams E.B., Shively J.M., Heinhorst S., Cannon G.C. (2004), A novel evolutionary lineage of carbonic anhydrase (class) is a component of the carboxysome shell, *J. of Bacteriol.* **186**, 623-630.
- Spielman A., D'Antonio M. (2001), Mosquito: The Story of Man's Deadliest Foe, Hyperion Books, New York.
- Stams T., Chen Y., Boriack-Sjodin P.A., Hurt J.D., Liao J., May J.A., Dean T., Laipis P., Silverman D.N., Christianson D.W. (1998), Structures of murine carbonic anhydrase IV and human carbonic anhydrase II complexed with brinzolamide: molecular basis of isozyme-drug discrimination, *Protein Sci.* **7**, 556-563.
- Stams T., Nair S.K., Okuyama T., Waheed A., Sly W.S., Christianson D.W. (1996), Crystal structure of the secretory form of membrane-associated human carbonic anhydrase IV at 2.8-Å resolution, *PNAS* **93**, 13589-13594.
- Steiner H., Jonsson B.H., Lindskog S. (1975), The catalytic mechanism of carbonic anhydrase. Hydrogen-isotope effects on the kinetic parameters of the human C isoenzyme, *Eur. J. Biochem.* **59**, 253-259.
- Strop P., Smith K.S., Iverson T.M., Ferry J.G., Rees D.C. (2001), Crystal structure of the "cab"-type beta class carbonic anhydrase from the archaeon *Methanobacterium thermoautotrophicum*, *J Biol Chem.* **276**, 10299-10305.
- Supuran C.T., Scozzafava A., Conway J. (2004), Carbonic Anhydrase: Its Inhibitors and Activators, CRC Press, Boca Raton.
- Tanhauser S.M., Jewell D.A., Tu C.K., Silverman D.N., Laipis P.J. (1992), A T7 expression vector optimized for site-directed mutagenesis using oligodeoxyribonucleotide cassettes, *Gene* **117**, 113-117.
- Taniuchi K., Nishimori I., Takeuchi T., Fujikawa-Adachi K., Ohtsuki Y., Onishi S. (2002), Developmental expression of carbonic anhydrase-related proteins VIII, X, and XI in the human brain, *Neuroscience* **112**, 93-99.
- Tashian R.E. (1992), Genetics of mammalian carbonic anhydrases, *Adv. Genet.* **30**, 321-356.

- Thiel A. (1913), Über die langsame neutralisation des kohlenensäure, *Berichte Deutsche Chem Gesellschaft* **46**, 241-244.
- Thompson J.D., Higgins D.G., Gibson T.J. (1994), Using Clustal for multiple sequence alignments, *Nucleic Acids Research* **22**, 4623-4680.
- Tibell L., Forsman C., Simonsson I., Lindskog S. (1985), The inhibition of human carbonic anhydrase II by some organic compounds, *Biochim Biophys Acta.* **829**, 202-208.
- Tripp B.C., Ferry J.G. (2000), A structure-function study of a proton transport pathway in the gamma-class carbonic anhydrase from *Methanosarcina thermophila*, *Biochem.* **39**, 9232-9240.
- Tripp B.C., Smith K., Ferry J.G. (2001), Carbonic anhydrase: New insights for an ancient enzyme *J. Biol. Chem.* **276**, 48615-48618.
- Tu C.K., Couton J.M., Van Heeke G., Richards N.G.J., Silverman D.N. (1993), Kinetic analysis of a mutant (His107-Tyr) responsible for human carbonic anhydrase II deficiency syndrome, *J. Biol. Chem.* **268**, 4775-4779.
- Tu C.K., Silverman D.N., Forsman C., Jonsson B.H., Lindskog S. (1989), Role of histidine 64 in the catalytic mechanism of human carbonic anhydrase II studied with a site-specific mutant, *Biochem.* **28**, 7913-7918.
- Tufts B.L., Esbaugh A., Lund S.G. (2003), Comparative physiology and molecular evolution of carbonic anhydrase in the erythrocytes of early vertebrates, *Comp. Biochem. Physiol. Part A* **136**, 259-269.
- Türeci O., Sahin U., Vollmar E., Siemer S., Gottert E., Seitz G., Parkkila A.K., Shah G.N., Brubb J.H., Pfreundschuh M., Sly W.S. (1998), Human carbonic anhydrase XII: cDNA cloning, expression, and chromosomal localization of a carbonic anhydrase gene that is overexpressed in some renal cell cancers, *PNAS* **95**, 7608-7613.
- Ulmasov B., Waheed A., Shah G.N., Grubb J.H., Sly W.S., Tu C.K., Silverman D.N. (2000), Purification and kinetic analysis of recombinant CA XII, a membrane carbonic anhydrase overexpressed in certain cancers, *PNAS* **97**, 14212-14217.
- Venkatasubban K.S., Silverman D.N. (1980), Carbon dioxide hydration activity of carbonic anhydrase in mixtures of water and deuterium oxide, *Biochem.* **19**, 4984-4989.
- Venta P.J. (2000), Inherited deficiencies and activity variants of the mammalian carbonic anhydrase in: Chegwidden WR, Carter ND, Edwards YH (Eds.), *The Carbonic Anhydrases*, New Horizons; Birkhauser Verlag Basel, Switzerland, 403-412.

- Venta P.J., Welty R.J., Johnson T.M., Sly W.S., Tashian R.E. (1991) Carbonic anhydrase deficiency syndrome in a Belgian family is caused by a point mutation at an invariant histidine residue (107 His – Tyr): Complete structure of the normal human CA II gene, *Am. J. Hum. Genet.* **49**, 1082-1090.
- Vidgren J., Liljas A., Walker N.P. (1990), Refined structure of the acetazolamide complex of human carbonic anhydrase II at 1.9 Å, *Int. J. Biol. Macromol.* **12**, 342-344.
- Lu D. Voth G.A. (1998), Molecular dynamics simulations of human carbonic anhydrase II: Insight into experimental results and the role of solvation, *Proteins* **33**, 119-134.
- Wallace A.C., Laskowski R.A., Thornton J.M. (1995), LIGPLOT: A program to generate schematic diagrams of protein-ligand interactions, *Protein Eng.* **8**, 127-134.
- Whittington D.A., Waheed A., Ulmasov B., Shah G.N., Grubb J.H., Sly W.S., Christianson D.W. (2001), Crystal structure of the dimeric extracellular domain of human carbonic anhydrase XII, a bitopic membrane protein overexpressed in certain cancer tumor cells, *PNAS* **98**, 9545-9550.
- Whittington D.A., Grubb J.H., Waheed A., Shah G.N., Sly W.S., Christianson D.W. (2004), Expression, assay, and structure of the extracellular domain of murine carbonic anhydrase XIV: Implications for selective inhibition of membrane-associated isozymes, *J. Biol. Chem.* **279**, 7223-7228.
- Wykoff C.C., Beasley N.J., Watson P.H., Turner K.J., Pastorek J., Sibtain A., Wilson G.D., Turley H., Talks K.L., Maxwell P.H., Pugh C.W., Ratcliffe P.J., Harris A.L. (2000), Hypoxia-inducible expression of tumor-associated carbonic anhydrases, *Cancer Res.* **60**, 7075-7083.
- Xue Y., Liljas A., Jonsson B.H., Lindskog S. (1993), Structural analysis of the zinc hydroxide-Thr199-Glu106 hydrogen bond network in human carbonic anhydrase II, *Proteins* **17**, 93-106.(a)
- Xue Y., Vidgren J., Svensson S., Liljas A., Jonsson B.H., Lindskog S. (1993), Crystallographic analysis of Thr-200-->His human carbonic anhydrase II and its complex with the substrate, HCO_3^- , *Proteins Struct. Funct. Genet.* **15**, 80-87.(b)

BIOGRAPHICAL SKETCH

Suzanne Zoë Fisher was born in Cape Town, South Africa, in 1976. She graduated from the high school Jan van Riebeeck in 1994 and spent a year after that working and traveling around Europe. In 1996 she entered the University of Stellenbosch and completed her undergraduate B.Sc. in 1999, majoring in biochemistry and animal physiology. In 2000 Zoë then went on to obtain her B.Sc.(Hons.) in the Biochemistry Department under the direction of Prof. Janet Hapgood. At the end of that year, she moved to the United States to work as a lab technician for Dr. Christopher West, Professor of Anatomy and Cell Biology at the University of Florida. In the Fall of 2002, she started in the Interdisciplinary Program and subsequently joined the lab of Dr. Robert McKenna. She worked on the elucidation of the proton transfer mechanism in carbonic anhydrase using a structural biology approach.